UNIVERSITY of CALIFORNIA
Santa Barbara

Heusler materials for thermoelectric applications: phase separation, atomic site disorder, and interstitials

A Dissertation submitted in partial satisfaction of the

requirements for the degree

Doctor of Philosophy

in

Materials

by

Malinda Leigh Caudle Buffon

Committee in charge:

Professor Ram Seshadri, Chair
Professor Tresa Pollock
Professor Stephen Wilson
Professor Steve Buratto

June 2017

The dissertation of Malinda Leigh Caudle Buffon is approved.

Professor Tresa Pollock

Professor Stephen Wilson

Professor Steve Buratto

Professor Ram Seshadri, Committee Chair

April 2017

Heusler materials for thermoelectric applications:

phase separation, atomic site disorder, and interstitials

by

Malinda Leigh Caudle Buffon

there once was a man from Waukee

who saw her for all she could be

his vision is not met

but there was no regret

for it was about the journey, you see

dedicated to my daddy

Acknowledgements

This work would not be possible without the academic support I have been provided. First and foremost, thanks to Professor Ram Seshadri for the deep care he holds for all students. The role he takes upon himself to support students and their scientific development makes him a pillar to this department. Thanks to Professor Tresa Pollock for her impressive ability to ask just the right questions to guide this work. Thanks to: Professor Steven Wilson for his guidance and astute observations, to Professor Jim Allen for his conversations and to Professor Steve Buratto, not only for his willingness to jump on this committee in the last month, but for always remaining an encouraging presence during my time at UCSB. I would like to thank the professors of IRG-3 for bringing their perspectives, questions, and guidance to the projects included here. Thanks to my undergraduate research adviser, Professor Paul Canfield, who first inspired me to pursue an advanced degree.

Without the aid of an excellent staff, completing this project would have been infinitely more difficult. Thank you to all the MRL staff for supporting the varied tasks with which I needed assistance. Thank you, Amanda Strom, for being a source of advice and patient guidance. Thanks to Mark Cornish for his aid in the microscopy lab and his excellent stories. To Deryck Stave for running

the MPL. Thanks to Chris Torbet for running machinery critical to this project and for his cool disposition when equipment misbehaves.

I am thankful for the interns who have, from a logistical perspective, helped me complete much of the sample preparation for the studies in this document. More than just making samples, thank you for forgiving me for my mistakes, telling me when I do things right, and allowing me to invest in your education. To Demetrius, thank you for your honesty, your drive for self improvement emboldens me. To Natalie, you are persistent and strong. To Shahryar, thank you for sharing your passion, it inspires this weary graduate student.

I am thankful to have landed at such a university as UCSB. The supportive infrastructure reflects how the leaders of this university care for their students. I am thankful for family student housing, a place that became more than a place to live by encouraging a community of friends. Thanks to UCSB CAPS for providing access to counseling that helped during times of need.

I am thankful for the support of teammates, ranging from high school swimming and Iowa State to UCSB triathlon and SBSC masters. Thank you for cheering for me, training with me, racing against me, and sharing a sport that has helped to develop much of who I am. Thank you to all the coaches who have encouraged and pushed me.

Thank you to the my fellow UCSB students for being more than colleagues, but friends. Thanks to the MRL community for providing a welcoming workspace. Thank you to the Buratto group. To Cynthia, who has a beautiful soul and is nice enough to share. Thank you to the Seshadri group for incredible feedback, companionship, and good laughs. To Molleigh for the real conversations that we share. To Geneva for her relentless support, both personally and academically. And to Megan, who has shared this journey with me and, by countering my stubbornness with her own, helped us develop a friendship centering on vulnerability.

Thanks for Vera for choosing to share this long distance friendship with me, we never chat enough but when we do it's always right. Cyndi, who stepped into a place of seemingly endless grace when my family needed it most. Chelsea, who first shared *Sleeping at Last* before it healed us.

Thanks to the my pet ratties: Arya, Sansa, Dani, and Kat for being my furbabies, putting up with many snuggles, and always being as excited to see me as I was to see them.

I am blessed to be part of a family that surrounds me with love and believes in me more than I believe in myself. Thanks to Grandma Helen, Grandpa Bob, and Aunt Suzanne. To my in-laws, for accepting me, exactly as I am, into their

family. To Dana: you are the best sissy I never knew to ask for, thank you for your listening ear and supportive advice. Thanks to my parents, for being my first fans, teaching me the value of critical thinking, and encouraging me to keep persisting.

Thank you Josh – for everything and beyond. I am thankful to the stars that we found each other. May we wander this life together.

Curriculum Vitæ

Malinda Leigh Caudle Buffon

Education

2012–2017 Ph.D. in Materials

University of California, Santa Barbara, CA, USA.

2008–2012 B.S. in Materials Science and Engineering

Iowa State University, Ames, IA, USA.

Publications

8. **M. L. C. Buffon**, G. Laurita, J. Graser, S. Mooraj, T. Sparks, T. Pollock, and R. Seshadri, Investigation of thermoelectric performance in pseudo–binary half-Heusler alloy between TiNiSn and NbCoSn, *In progress.*

7. **M. L. C. Buffon**, G. Laurita, L. Lamontagne, E. Levin S. Mooraj, D. Lloyd, N. White, T. Pollock, and R. Seshadri, Thermoelectric performance and the role of anti-site disorder in Heusler $TiFe_2Sn$, *In progress*.

6. **M. L. C. Buffon**, G. Laurita, N. Verma, L. Lamontagne, L. Ghadbeigi, D. Lloyd, T. Sparks, T. Pollock, and R. Seshadri, Enhancement of thermoelec-

tric properties in the Nb–Co–Sn half-Heusler/Heusler system through spontaneous inclusion of a coherent second phase, *J. Appl. Phys.* **120** (2016) p. 075104. [**doi**]

5. M. Boucherit, O. Shoron, C. A. Jackson, T. A. Cain, **M. L. C. Buffon**, C. Polchinski, S. Stemmer, and S. Rajan, Modulation of over 10^{14} cm^{-2} electrons in $SrTiO_3/GdTiO_3$ heterostructures, *Appl. Phys. Lett.* **104** (2014) 182904. [**doi**]

4. T. Kong, C. Cunningham, V. Taufour, S.L. Budko, **M. L. C. Buffon**, X. Lin, H. Emmons, P.C. Canfield, Thermodynamic and transport properties of single crystalline RCo_2Ge_2 (R=Y, La-Nd, Sm-Tm), *J. Magn. Mater.* **358** (2014) 212. [**doi**]

3. C. Liu, Y. Lee, T. Kondo, E.D. Mun, **M. L. Caudle**, B.N. Harmon, S.L. Budko, P.C. Canfield and A. Kaminsk, Metallic surface electronic state in half-Heusler compounds RPtBi (R=Lu, Dy, Gd), *Phys. Rev. B: Condens. Matter* **83** (2011) 205133. [**doi**]

2. A. I. Goldman, A. Kreyssig, S. Nandi, M.G. Kim, **M. L. Caudle** and P.C. Canfield, High-energy X-ray diffraction studies of *i*-$Sc_{12}Zn_{88}$, *Philos. Mag.* **91** (2010) 2427-2433. [**doi**]

1. P.C. Canfield, **M. L. Caudle**, C.-S. Ho, A Kressig, S. Nandi, M. G. Kim, X. Lin, A. Kracher, K. W. Dennis, R. W. McCallum, and A. I. Goldman, Solution growth of a binary icosahedral quasicrystal of $Sc_{12}Zn_{88}$, *Phys. Rev. B: Condens. Matter* **81** (2010) 020201. [**doi**]

Abstract

Heusler materials for thermoelectric applications:

phase separation, atomic site disorder, and interstitials

by

Malinda Leigh Caudle Buffon

By converting heat into electricity and *vice versa*, thermoelectric devices have a range of applications, including solid state refrigeration, powering space probes, and converting waste heat into energy. The performance of thermoelectric materials is characterized by the thermoelectric figure of merit (zT) which requires a large-magnitude Seebeck coefficient (S), reduced electrical resistivity (ρ), and reduced thermal conductivity (κ). Heusler (XY_2Z) and half-Heusler (XYZ) materials with 18 and 24 valence electron counts are of particular interest for waste-heat thermoelectric applications due to their derivation from affordable elements, mechanical reliability, and thermal stability at operating conditions. In this work, we discuss four unique studies in which we engineer, characterize, and explore three different Heusler variants: NbCoSn, $TiFe_2Sn$, and TiNiSn. Through these vignettes, we find a connection between atomic

structural disorder and thermoelectric performance.

We begin by exploring the effect of phase separation in the NbCoSn–$NbCo_2Sn$ system in the form of $NbCo_{1+x}Sn$. The introduction of Heusler particulates to a half-Heusler matrix is an established technique for zT enhancement by reducing thermal conductivity without impacting electrical performance. In addition to the successful application of this technique to NbCoSn, we find that an annealing treatment regulates antisite disorder in this system. This plays a critical role in improving thermoelectric performance.

We explored variations of Heusler compound $TiFe_2Sn$, revealing the role of antisite disorder. First, we considered variations on the Ti–Fe ratio as $Ti_{1+x}Fe_{2-x}Sn$, concluding that all compounds contain Ti–Fe antisite disorder and this disorder can be reduced by preparing a Ti–rich variation of this compound. Next, we attempted to modify the charge carrier concentration as $TiFe_2Sn_{1-y}Sb_y$. This technique modifies the Seebeck coefficient, but does not enhance the Seebeck coefficient as expected by electrical band structure calculations. This discrepancy arises from calculations completed for a perfect crystal that do not include the observed antisite defects.

Next, we examined a novel 18 valence electron solid solution formed between half-Heusler compounds TiNiSn and NbCoSn: $(TiNiSn)_{1-x}(NbCoSn)_x$.

We first confirm the successful preparation of the solid solution and then examined the thermoelectric properties. Characterization of thermoelectric performance shows that the introduction of substitutional atoms degrades electrical performance while improving thermal conductivity. Intermediate compound $(TiNiSn)_{0.5}(NbCoSn)_{0.5}$ has the most promising thermoelectric performance of the alloys, owing to a high-temperature Seebeck coefficient that is larger than that of any other composition.

Finally, we consider a heat treatment study that evaluates the presence of Ni-interstitials in Ni-rich TiNiSn in relation to their impact on thermoelectric performance. Heat treatments are designed so that samples are thermodynamically encouraged to either phase separate into TiNiSn and $TiNi_2Sn$ or to accommodate excess Ni as Ni-interstitials. This work shows that the presence of Ni-interstitials enhances the thermoelectric performance of TiNiSn by simultaneously increasing the Seebeck coefficient and reducing thermal conductivity.

Contents

Contents xv

List of Figures xvii

List of Tables xix

1 Introduction 1

1.1 Thermoelectric materials for power generation 1

1.2 Heusler and half-Heusler materials 10

1.3 Overview 18

2 Enhancement of thermoelectric properties in the Nb–Co–Sn half-Heusler/Heusler system through spontaneous inclusion of a coherent second phase 20

2.1 Introduction 22

2.2 Experimental details 23

2.3 Results and discussion 27

2.4 Conclusion 47

3 Thermoelectric performance and the role of anti-site disorder in Heusler $TiFe_2Sn$ 48

3.1 Introduction 49

3.2 Methods . . . 51
3.3 Results and discussion . . . 54
3.4 Conclusions . . . 69

4 Investigation of thermoelectric performance in pseudo–binary half-Heusler alloy between TiNiSn and NbCoSn 70

4.1 Introduction . . . 71
4.2 Experimental details . . . 72
4.3 Structural characterization . . . 75
4.4 Physical properties . . . 81
4.5 Conclusions . . . 86

5 Phase separation and thermoelectric properties with heat treatment in half-Heusler TiNiSn 87

5.1 Introduction . . . 87
5.2 Experimental details . . . 89
5.3 Results and discussion . . . 92
5.4 Conclusions . . . 100

6 Summary and future directions 102

6.1 Summary . . . 102
6.2 Future directions . . . 104
6.3 Conclusions . . . 107

A Comparing sample preparations of NbCoSn 108

B Price curves 113

Bibliography 113

List of Figures

1.1 Depiction of the Seebeck effect and a thermoelectric device . . . 3
1.2 Overview of thermoelectric materials classes . . . 9
1.3 Depiction of half-Heusler and Heusler crystal structure . . . 11
1.4 Data mining results of 18 VEC half-Heusler compounds for thermoelectric performance . . . 14
1.5 Depiction of disorder in Heusler variant materials . . . 16

2.1 Electronic band structure and density of state calculations for NbCoSn . . . 28
2.2 Powder synchrotron X-ray diffraction results of $NbCo_{1+x}Sn$ . . . 31
2.3 Neutron diffraction results for $NbCo_{1+x}Sn$ . . . 32
2.4 Lattice constant and phase fractions for $NbCo_{1+x}Sn$ . . . 35
2.5 Scanning electron microscopy of $NbCo_{1+x}Sn$ . . . 37
2.6 Transmission electron microscopy of $NbCo_2Sn$ precipitates in NbCoSn matrix . . . 39
2.7 Electronic transport properties for $NbCo_{1+x}Sn$ . . . 41
2.8 Thermoelectric power factor for $NbCo_{1+x}Sn$ . . . 43
2.9 Thermal conductivity for $NbCo_{1+x}Sn$ . . . 44
2.10 zT for $NbCo_{1+x}Sn$ . . . 46

3.1 Electrical band structure calculations for $TiFe_2Sn$ . . . 55

3.2 Synchrotron X-ray and neutron diffraction study for $TiFe_2Sn$ . . . 57
3.3 Structural parameter results for $Ti_{1+x}Fe_{2-x}Sn$ 58
3.4 Refinements and resulting lattice constants for $TiFe_2Sn_{1-y}Sb_y$ . . 60
3.5 Electron microscopy for $TiFe_2Sn$ 62
3.6 Electrical transport properties of $Ti_{1+x}Fe_{2-x}Sn$ 65
3.7 Electrical transport properties of $TiFe_2Sn_{1-y}Sb_y$ 67

4.1 Synchrotron X-ray diffraction study for TiNiSn–NbCoSn solid solution 77
4.2 Neutron diffraction study for TiNiSn–NbCoSn solid solution . . . 79
4.3 Structural parameter results for TiNiSn–NbCoSn solid solution . . 80
4.4 Electronic property results for TiNiSn–NbCoSn solid solution . . . 82
4.5 Thermal conductivity and zT for TiNiSn–NbCoSn solid solution . 85

5.1 Depiction of heat treatments for $TiNi_{1.1}Sn$ samples 90
5.2 Comparison of percent $TiNi_2Sn$ with sample preparation 93
5.3 The main (220) peak of TiNiSn samples 95
5.4 SEM of $TiNi_{1.1}Sn$ heat treatment study 96
5.5 Thermoelectric properties of heat-treated $TiNi_{1.1}Sn$ 98

A.1 Comparing electrical resistivity of NbCoSn samples 109
A.2 Comparing Seebeck coefficient of NbCoSn samples 110
A.3 Comparing thermal conductivity of NbCoSn samples 111
A.4 Comparing zT of NbCoSn samples 112

B.1 Price curve for Chapter 2, NbCoSn 114
B.2 Price curve for Chapter 4, TiNiSn–NbCoSn solid solution 115

List of Tables

2.1 Structural parameters of the NbCoSn phase as obtained from Rietveld refinement of the neutron diffraction data 33

6.1 Summary of impact of defects on thermoelectric properties 105

Preface

The working title of this thesis was *Adventures in Imperfections*, a title that, while unsuited to a scientific communication, expresses its theme. In contrast to my juvenile understanding of crystal structures, (regular and perfect) I found Heusler-based materials to be the home for defects that were not only interesting, but added to the quality of these compounds. Explorations of these imperfections are catalogued by this document, making it a literal collection of *Adventures in Imperfections*, a title that also comments on a lesson I relearn again and again: life is extraordinary when we release expectations and face the complex reality in which we live.

Chapter 1

Introduction

1.1 Thermoelectric materials for power generation

As nearly half of the energy produced in the United States is lost as waste heat,[1] recapturing this heat and converting it into energy would reshape the energy landscape. Thermoelectric devices provide a pathway towards sustainability by transforming a temperature gradient into a voltage differential.[2–4] This enables energy harvesting of waste heat that is available in the form of body heat,[5] automotives,[6, 7] and energy production.[8]

The Seebeck effect was originally discovered in 1821 by Thomas Seebeck who, upon forming a circuit between two dissimilar materials and holding

their junctions at different temperatures, observed the deflection of a compass needle.[9] Over the next 130 years, various efforts were made to exploit thermoelectric materials as generators, but success was limited by low efficiency. During the 1950s to 1970s, the rise of space-related applications drove the development of thermoelectric generators through the refinement of tellurium based thermoelectrics that were utilized in applications such as the Apollo missions and Voyager I and II space probes. Materials processing plays a critical role in recent thermoelectric improvements and has enabled improvements that continues through the current day.[10, 11] Thermoelectric devices have many modern applications including spacecraft, such as the Curiosity rover and New Horizons probe, vibration free refrigerators, portable coolers, and even camp stoves that charge electronic devices.

As depicted by Figure 1.1 (a), when a material is held under a temperature difference (ΔT) electronic charge carriers on the heated side have a larger velocity than the carriers on the cold side. This results in a relatively increased charge carrier density on the cold side of the material. The resulting voltage difference is described as a function of both the Seebeck coefficient and the temperature gradient:

$$\Delta V = -S\Delta T \tag{1.1}$$

The direction of current is determined by the type of charge carrier. Charge

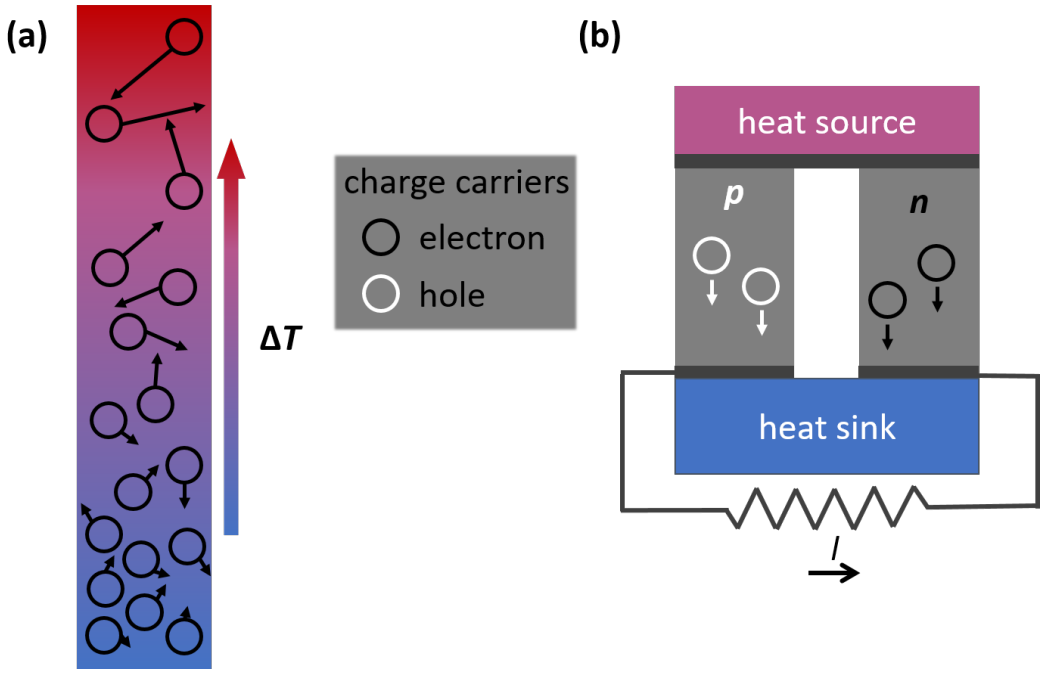

Figure 1.1: (a) Illustration of the Seebeck effect, showing that electronic charge carriers move towards the cold side of a material in a temperature gradient. (b) Single-module depiction of a thermoelectric generator. Upon placing $n-$ and $p-$type materials electrically in series and thermally in parallel, this circuit will carry a load.

carriers include electrons ($n-$type) and holes ($p-$type). The type of carrier is noted by the sign of the Seebeck coefficient, which is negative when electrons are the primary carriers and positive when holes are the primary charge carriers. A power generating thermoelectric device is engineered by placing $n-$ and $p-$type semiconductors electrically in series, but thermally in parallel, as shown in Figure 1.1 (b).[2] Upon placing this device in a thermal gradient, all carrier types diffuse towards the cold sink enabling a current that powers a load. This device can be readily scaled through the addition of more thermoelectric couples, enabling solid state energy production.

1.1.1 Evaluation of thermoelectric performance

The efficiency of a thermoelectric device is proportional to the Carnot efficiency (η_C):

$$\eta_C = \frac{T_H - T_C}{T_H} \tag{1.2}$$

where T_H and T_C are the hot and cold-side temperatures. To evaluate the efficiency of a thermoelectric device (η_{TE}), a figure of merit ($Z\bar{T}$) is introduced to describe the thermoelectric performance of the device:

$$\eta_{TE} = \eta_C \frac{\sqrt{1+Z\bar{T}} - 1}{\sqrt{1+Z\bar{T}} + \frac{T_C}{T_H}} \tag{1.3}$$

$Z\bar{T}$ depends on the Seebeck coefficient (S), electrical resistivity (ρ), thermal conductivity (κ) of the $n-$ and $p-$ type materials, and the average temperature between the hot and cold-side surfaces ($\bar{T}$):

$$Z\bar{T} = \frac{(S_p - S_n)^2}{[(\rho_n \kappa_n)^{\frac{1}{2}} + (\rho_p \kappa_p)^{\frac{1}{2}}]^2} \bar{T} \tag{1.4}$$

Evaluation of a single material for thermoelectric performance is completed by determining its individual thermoelectric figure of merit (zT) at any given temperature (T): [3]

$$zT = \frac{S^2}{\rho\kappa} T \tag{1.5}$$

zT is the thermoelectric figure of merit that will be referenced to when evaluating the materials in this document.

Evaluation of equation 1.5 presents the desirable physical properties of a thermoelectric material. First, a large Seebeck coefficient ensures that, upon being in a temperature gradient, the material produces a large voltage differential. Next, a low electrical resistivity enables a current to readily pass through the device. Finally, a low thermal conductivity limits heat transfer between the hot and cold sides of the device. Thus, a promising thermoelectric material will conduct electrons like a crystal while conducting heat like a glass. As will be discussed, these terms are interdependent such that development of an *electronic crystal phonon glass* requires advanced materials design.

The Seebeck coefficient and the electrical resistivity are described together as the powerfactor (PF, $S\rho^{-1}$) and both depend on charge carrier concentration (n). A simplified model for Seebeck coefficient, assuming a degenerate semiconductor with a single parabolic band, is:

$$S = \frac{8\pi^2 k_B^2}{3qh^2} m^* T \Big(\frac{\pi}{3n}\Big)^{3/2} \tag{1.6}$$

where q is the electronic charge constant, h is Planck's constant, k_b is the Boltzmann constant, and m^* is the effective mass. In addition to this dependence on carrier concentration, the Seebeck coefficient is dependent on effective mass, which is inversely proportional to the band curvature of the electronic band structure at the Fermi energy. Effective mass is larger for a flat band. Electrical resistivity is described as:

$$\frac{1}{\rho} = nq\mu \tag{1.7}$$

where μ is the carrier mobility. Mobility is also dependent on effective mass, where a smaller effective mass allows carriers to move easily through a material. The Seebeck coefficient and electrical resistivity of a material are dependant on carrier concentration and effective mass such that they are contraindicated. As one property is improved, the other is deteriorated. For this reason, while zT can be optimized at a given carrier concentration, it is challenging to truly enhance zT by modifying carrier concentration.

Thermal conductivity (κ) results from the additive contributions of many smaller effects.[12] For this analysis we will consider a model consisting of two components: one pertaining to the electrical contribution to thermal conductivity (κ_e) and the other arising from lattice contribution to thermal conductivity (κ_l) such that:

$$\kappa = \kappa_l + \kappa_e \tag{1.8}$$

The electronic contribution to thermal conductivity depends on electrical resistivity through the Wiedemann-Franz law as:

$$\kappa_e = nqLT\mu \tag{1.9}$$

where L is the Lorenz factor and is generally treated as a constant determined from a free-electron model.[2] Equation 1.9 indicates that this component of thermal conductivity, similar to the Seebeck coefficient and electrical resistivity, is dependent on both the carrier concentration and carrier mobility. In contrast, the lattice contribution to thermal conductivity is dependent on heat capacity, phonon group velocity, and the mean free path lengths of phonons. The lattice contribution to thermal conductivity is generally determined experimentally by subtracting the calculated electronic contribution from the total thermal conductivity. Lattice thermal conductivity can be reduced through the introduction of phonon scattering centers. Thus, as the lattice contribution to thermal conductivity is the only component of zT that does not depend on carrier concen-

tration or carrier mobility, phonon scattering centers become a pivotal tool in zT improvement. The objective in thermoelectric materials design is to introduce phonon scattering centers at a range of length scales without negatively impacting the electronic performance of the same material.

1.1.2 Materials classes for thermoelectric applications

A vast number of material classes, such as Bi_2Te_3,[14] clathrates,[15] and skutterudites[16] have been explored as thermoelectric materials. Work by Gaultois *et al.* collected key results from these different materials classes, developing a database of thermoelectric performance.[13] Upon sorting these results by materials class, as shown in Figure 1.2, the potential of half-Heusler materials becomes evident through their relatively large power factors, resulting from Seebeck coefficients that can reach in excess of $|200|\,\mu VK^{-1}$.[17] Half-Heusler materials were first considered for thermoelectric applications by Hohl *et al.* in 1999[18] and have since been prepared with zT values larger than 1.[19] Furthermore, half-Heusler compounds are prepared from relatively abundant elements, are thermally robust, and are mechanically reliable. Large thermal conductivity is the primary challenge for half-Heusler thermoelectric materials and is typically $>$ $5\,Wm^{-1}K^{-1}$, as compared to $1\,Wm^{-1}K^{-1}$ in Bi_2Te_3 derived

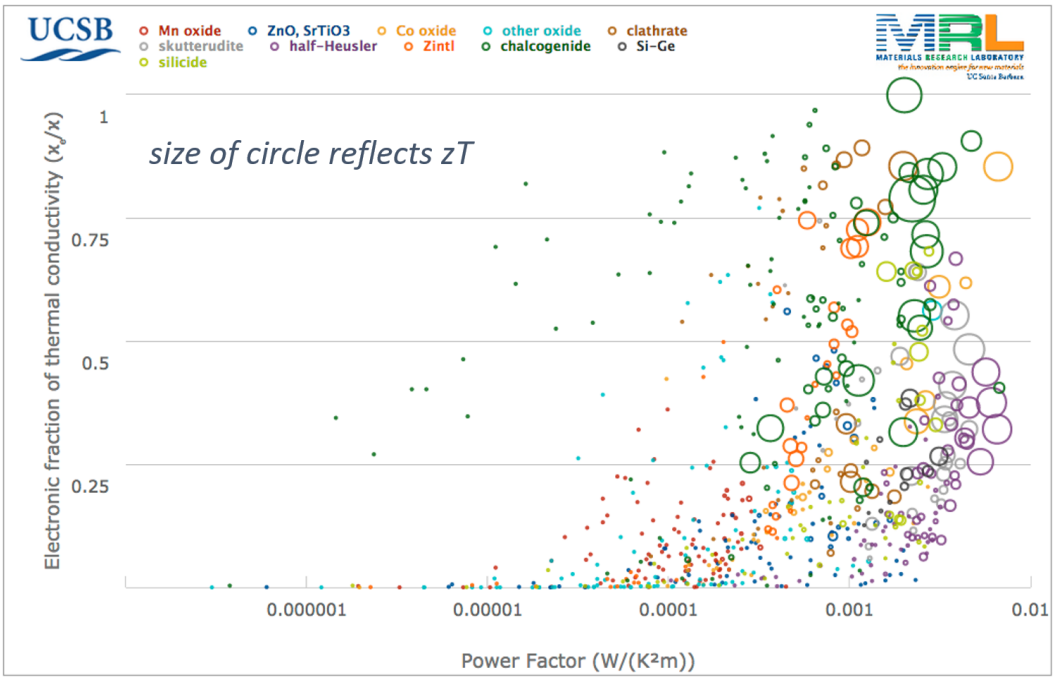

Figure 1.2: Data mining overview of various materials for thermoelectric performance at their peak zT. Material class is identified by color. Power factor follows the x-axis, $\frac{\kappa_{electronic}}{\kappa_{total}}$ is the y-axis, and size of circle indicates relative zT. Half-Heusler materials are shown in purple, displaying large power factors with thermal conductivities that result largely from the lattice component, indicating half-Heusler materials will benefit from phonon-scattering techniques to decrease κ and increase zT. Database from Ref. [13].

compounds.[14] However, as also indicated in Figure 1.2, a majority of this thermal conductivity arises from the lattice contribution term. As the lattice contribution to thermal conductivity can be reduced by introducing phonon scattering centers with limited impact to electrical terms, the thermoelectric performance of half-Heusler materials has a vast potential for improvement.

1.2 Heusler and half-Heusler materials

Heusler compounds were first synthesized in 1903 by Friedrich Heusler who discovered Cu_2MnAl was ferromagnetic despite containing no magnetic elements.[20] This led to the discovery of multiple large structural classes of materials, including half-Heusler (*hH*) and Heusler (*H*) compounds. Compounds with these structures exhibit properties with a broad range of applications including magnetic tunnel junctions,[21] topological insulators,[22] superconductivity,[23] magnetocalorics,[24] and thermoelectrics.[25]

1.2.1 Half-Heusler and Heusler crystal structure

The half-Heusler (*hH*, XYZ) and Heusler (*H*, XY_2Z) crystal structures are shown in Figure 1.3. The half-Heusler structure consists of three interpenetrat-

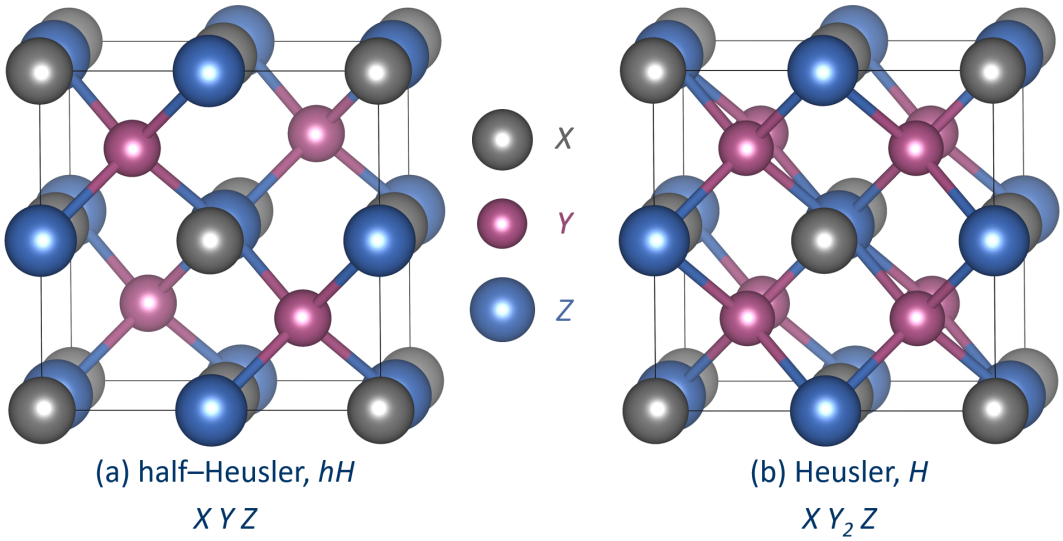

Figure 1.3: Depiction of the crystal structures of (a) cubic half-Heusler (*hH*), *XYZ* and (b) cubic Heusler (*H*), XY_2Z compounds described in the face-centered cubic space groups $F\bar{4}3m$ and $Fm\bar{3}m$, respectively. In both structures *X* are in the 4a Wyckoff site $(0,0,0)$, while *Z* are in $4b$ $(\frac{1}{2},\frac{1}{2},\frac{1}{2})$. In the *hH* structure, *Y* atoms are in $4c$ $(\frac{1}{4},\frac{1}{4},\frac{1}{4})$. In the *H* structure *Y* are in 8c $(\frac{1}{4},\frac{1}{4},\frac{1}{4})$ in $Fm\bar{3}m$. The diamondoid tetrahedral network formed by the *Y*–*Z* atoms of *hH* is indicated with bonds. X and Y atoms are typically transition metals and Z is a main group element.

ing face-centered cubic lattices that are offset by $(\frac{1}{4}, \frac{1}{4}, \frac{1}{4})$. As X and Z usually have the largest electronegativity difference, these form a XZ rock-salt lattice in which half of the Z coordinated tetrahedral sites are stuffed by Y atoms. The Heusler structure is similar, except that all tetrahedral sites are now occupied by additional Y atoms.[26]

An alternative perspective of the half-Heusler structure is useful for evaluating electronic behavior. Here, the structure is described as a zinc-blende sublattice, formed by *Y* and *Z* atoms, that is stuffed by *X* atoms. This consideration highlights the covalency of the YZ zinc-blende sublattice and the ionic contributions of X atoms. This has been emphasized in Figure 1.3 by bonds between the *Y*–*Z* atoms,

1.2.2 Heusler variant thermoelectric materials

Heusler and half-Heusler materials follow Slater-Pauling behavior, which provides a method to estimate the magnetic moment of 3d elements and their alloys from the valence electron count (VEC) of the compound. At a particular VEC that varies with material system, the compound is non-magnetic and semiconducting.[27] For the case of the half-Heusler, consider the zinc-blende sublattice discussed in the previous section. From this perspective, the valence

electrons from the electropositive X^{n+} are transferred to the more electronegative $(YZ)^{n-}$. When the total VEC is eighteen, the compound has a full shell and is expected to be semiconducting.[28] A similar argument can be made for Heusler compounds for a VEC of 24.[29] These semiconducting Heusler variant compounds are valuable for thermoelectric applications, displaying the desirable combination of high Seebeck coefficient, coupled with relatively low electrical resistivities. For this reason, when determining the material systems for the upcoming studies, only 18 VEC half-Heusler and 24 VEC Heusler compounds were considered.

The studies presented in this document were designed to examine the potential of promising, but under explored, Heusler variant compounds. Due to the large spectrum of Heusler variant materials to select from, a set of criteria was established. An ideal system should be a closed shell semiconductor (i.e. VEC of 18 for half-Heusler and 24 for Heusler), have a large power factor (indicating a large Seebeck coefficient), and be largely unexplored in the literature. A data mining and visualization approach was utilized in selection and results of the half-Heusler search are shown in Figure 1.4. This figure was developed from a list of all 18 VEC half–Heusler compounds, eliminating compounds that were derived from elements that were relatively expensive or air sensitive. Literature of remaining compounds was reviewed by cross referencing SciFinder, Google

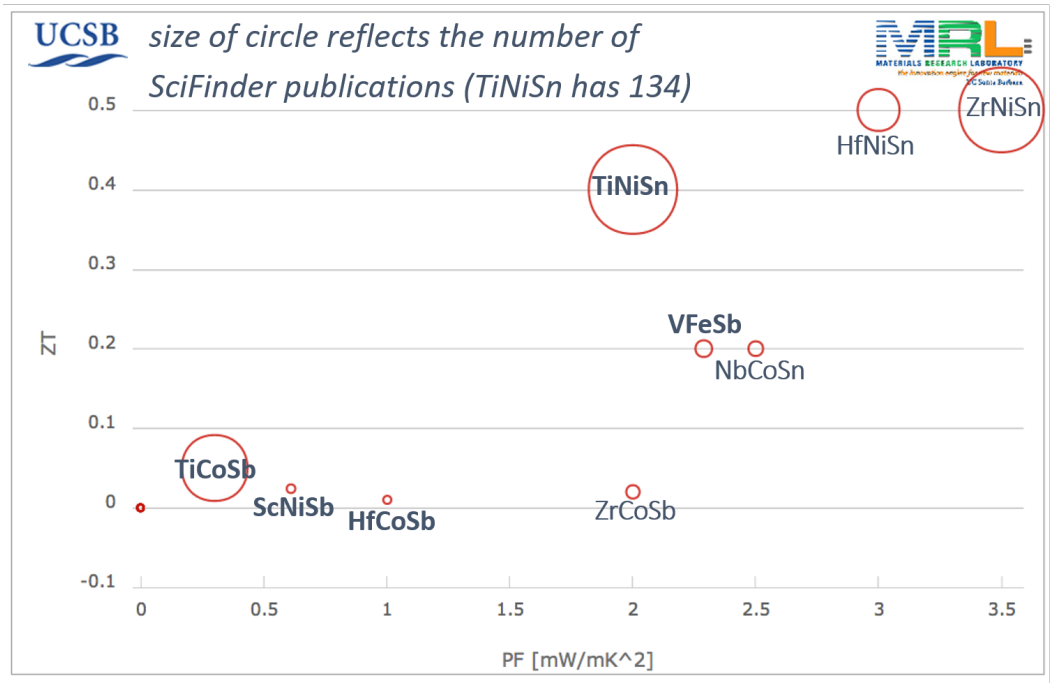

Figure 1.4: Summary of data mining results comparing thermoelectric performance of 18 VEC half-Heusler compounds as found from the literature plotted with power factor on the x-axis, zT on the y-axis, and size of circle is dependent on the volume literature on the compound. The MNiSn ($M =$ Ti, Hf, Zr) compounds have the most promising properties and are well examined by the literature. This plot illustrates the intrigue of under explored, but promising, compounds like VFeSb and NbCoSn.

Scholar, and the ICSD database. The resulting papers were scanned and key conclusions were entered into a spreadsheet, yielding the results in Figure 1.4. NbCoSn was selected from these results and will be discussed in Chapters 2 and 4. A similar search was conducted on 24 VEC Heusler compounds, leading to interest in $TiFe_2Sn$, the subject of chapter 3.

1.2.3 Structural disorder in Heusler variant materials

By containing chemically similar elements, Heusler variant materials exhibit various forms of crystallographic disorder.[27, 30, 31] The types of structural disorder discussed in this document are summarized in Figure 1.5. Understanding disorder is critical to describing observed physical properties of samples with varied stoichiometry and processing techniques and to evaluate differences between calculated properties and experimental results. Disorder plays a critical role in determining the physical properties of Heusler variant materials: sometimes benefiting thermoelectric performance and sometimes inhibiting it.

Substitutional defects, illustrated in frame (a) of Figure 1.5, introduce an impurity element to replace the expected element at a given atomic site. These substitutions are isovalent when the impurity atom has the same oxidation state as the original atom and are aliovalent when the oxidation states differ. These

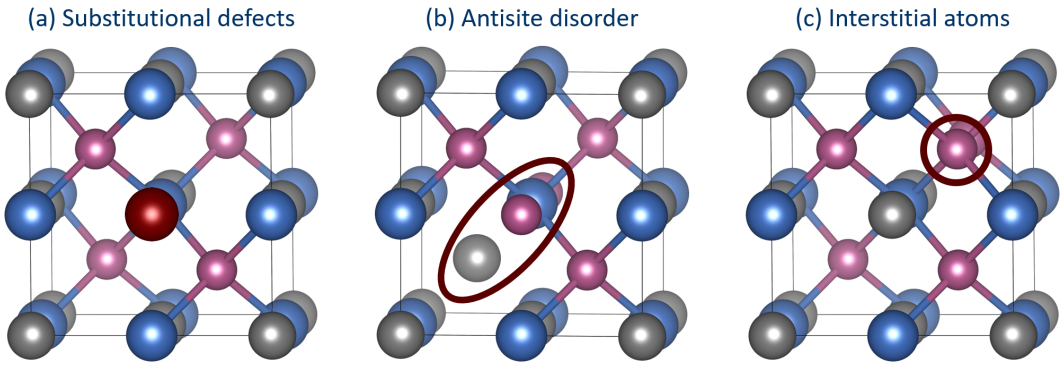

Figure 1.5: Depiction of three common defects, as shown on the half-Heusler crystal structure. Defects are highlighted in red. (a) Substitutional defects replace an existing atom with an impurity atom. This can be occur on any site, such as element A onto an X site (A_X) (b) Antisite disorder occurs when two elements switch the site that they reside on. While antisite defects occur in multiple combinations, for the studies presented here, X atoms reside on Y sites (X_Y) and Y atoms reside on X sites (Y_X). (c) Interstitial defects occur when a normally vacant site is filled. In this discussion, we will consider Y atoms residing in the same tetrahedral vacancy that is filled by Y in the Heusler crystal structure.

defects are frequently utilized in Heusler variant thermoelectric materials to both modify carrier concentration for peak electrical properties and to introduce phonon scattering centers that reduce thermal conductivity. Isovalent substitution of the X site, such as a MNiSn alloys, utilizes the same column of the periodic table (M = Ti, Zr, Hf) to introduce thermal conductivity reducing phonon scattering centers without impacting electronic structure.[32] Aliovalent substitution of the Z site, such as Sb for Sn, introduces extra electron charge carriers that can improve thermoelectric performance, such as TiNiSn$_{1-x}$Sb$_x$.[33]. By combining different substitutional defects, a zT greater than 1 has been achieved for compositions such as Hf$_{0.6}$Zr$_{0.4}$NiSn$_{0.98}$Sb$_{0.02}$.[19]

Antisite defects, depicted in Figure 1.5 (b), occur when an element that is already included in the crystal structure occupies an unintended site. For example, if element X occupied Y's atomic site. Antisite defects are common to Heusler compounds due their general covalency that limits the energetic penalty of antisite defects. In MnCo$_2$Sn and MnCo$_2$Si Heusler compounds, the Mn atom can readily occupy Co sites, impacting the magnetic properties of these compounds.[34] Unlike substitutional defects, antisite defects are difficult to intentionally introduce or to even completely remove from some Heusler variant compounds.

Interstitial defects, shown in Figure 1.5 (c), occur when an atom occupies an

otherwise empty space in the crystal structure. Due to the similarity between the half-Heusler and Heusler crystal structures, the vacant tetrahedral sites of the half-Heusler structure can be easily filled by a Y atom in some half-Heusler systems.[35] This occurs in the TiNiSn system and has been well explored.[36] This defect plays a critical role in the thermoelectric performance of TiNiSn by modifying the density of states.[37] The presence of these defects can be modified by considering the role of heat treatments and initial compound stoichiometry.

1.3 Overview

Multiple Heusler variant material systems were investigated for thermoelectric performance. Systems were selected as under studied, but promising, compounds that are 18 VEC half-Heusler or 24 VEC Heusler compounds. In these studies, various forms of structural disorder, some intentional and others not, were observed. The relationships of this disorder to thermoelectric performance is discussed. Specifically, this work addresses the following:

- **$NbCo_{1+x}Sn$:** Heusler $NbCo_2Sn$ precipitates dispersed in a NbCoSn matrix via two preparation techniques that vary by thermal cycle. Annealing impacts site ordering and physical properties.

- **$\mathbf{Ti_{1+x}Fe_{2-x}Sn}$** and **$\mathbf{TiFe_2Sn_{1-y}Sb}y$:** Examines antisite defects of Heusler compound $TiFe_2Sn$. These defects explain discrepancy in the role Sb-doping plays on electronic performance of $TiFe_2Sn$ in prepared compounds as compared to that expected from calculations.

- **$\mathbf{(TiNiSn)_{1-x}(NbCoSn)_x}$:** A novel solid solution between half-Heusler compounds TiNiSn and NbCoSn that maintains 18 VEC across the range is examined. Thermoelectric properties of intermediate compounds are evaluated, revealing the impact of substitutional defects on the Y site.

- **$\mathbf{TiNi_{1.1}Sn}$:** An annealing study of half-Heusler TiNiSn with emphasis on excess Ni that resides in interstitial sites. The impact that interstitial atoms have on thermoelectric performance is examined.

This thesis considers perspectives of Heusler variant materials, connecting structural disorder to thermoelectric performance. From these studies, we learn that while each Heusler variant material has unique defects with their own impact, all systems exhibit disorder. By understanding this disorder, the development of future thermoelectric generators becomes possible.

Chapter 2

Enhancement of thermoelectric properties in the Nb–Co–Sn half-Heusler/Heusler system through spontaneous inclusion of a coherent second phase

Half-Heusler *XYZ* compounds with an 18 valence electron count are promising thermoelectric materials, being thermally and chemically stable, deriving

from relatively earth-abundant components, and possessing appropriate electrical transport properties. The typical drawback with this family of compounds is their high thermal conductivity. A strategy for reducing thermal conductivity taken in this study was to introduce a secondary phase designed to minimize negative impact on other properties. Here, we achieve this through the addition of excess Co to half-Heusler NbCoSn, which introduces precipitates of a semi-coherent $NbCo_2Sn$ Heusler phase. A series of $NbCo_{1+x}Sn$ materials are characterized here using X-ray and neutron diffraction studies and electron microscopy. Electrical and thermal transport measurements and electronic structure calculations are used to understand property evolution. We find that annealing has an important role to play in determining antisite ordering and properties. Antisite disorder in the as-prepared samples improves thermoelectric performance through the reduction of thermal conductivity, but annealing during the measurement returns properties to resemble those of the annealed samples. Similar to the more widely studied $TiNi_{1+x}Sn$ system, Co addition to the NbCoSn phase results in improved thermoelectric performance through a decrease in thermal conductivity which results in a 20% improvement in the thermoelectric figure of merit, zT.

2.1 Introduction

A method of choice for lowering κ in *hH*–derived materials employs the spontaneous phase separation between *hH* and *H* phases to form a biphasic material. In this approach, extra *Y* solute is added to the starting compositions of *XYZ hH*, resulting, after suitable processing in a material of a *hH* matrix with *H* inclusions that act as phonon scattering centers. Douglas *et al.*[38] have employed this approach for the Ti–Ni–Sn system, forming a continuous *hH* TiNiSn matrix with discrete *H* $TiNi_2Sn$ inclusions. Three dimensional microstructural analysis of $TiNi_{1.20}Sn$ suggests the eventual percolation of the *H* phase at large Ni additions, which degrades zT as compared to $TiNi_{1.15}Sn$.[39] Detailed investigation of this two phase system shows that some excess Ni tends to enter the tetrahedral vacancies of the *hH* matrix, permitting this phase to exist at off stoichiometric concentrations. Continued additions of Ni results in the formation of small *H* clusters.[36] Similarly, the addition of Ni in (Zr,Hf)–Ni–Sn systems reveals phase separation to a mixture of *H* and *hH* phases,[40] and that that there is a relationship between structural ordering in (Ti,Zr,Hf)–Ni–Sn *hH* materials and thermoelectric properties[41]. The combined effect of *H* inclusions and tetrahedral interstitials introduces phonon scattering at a range of length scales, leading to further reduction in κ. [42] Here we explore this approach in

an alternate *hH–H* system: Nb–Co–Sn.

NbCoSn (*hH*) and $NbCo_2Sn$ (*H*) compounds are reported to be stable in the Nb–Co–Sn phase space.[43] NbCoSn *hH* was selected due to its 18 valence electron count. NbCoSn has been explored for thermoelectric applications by Ono *et al.*, who investigated the effect of Sb–doping on the thermoelectric properties,[43] while Kimura *et al.* explored biphasic $NbCo_{1+x}Sn$, $x = 0.00$, 0.05, 0.10, prepared by optical float zone, indicating that it is possible to reduce the thermal conductivity of NbCoSn through the addition of Co.[44, 45]

In this work, we will show that the *hH* phase of NbCoSn can be formed without the annealing step required for most *hH* materials, including TiNiSn. The absence of annealing for NbCoSn phase formation allows the study of how preparation and subsequent ordering in *hH* materials impacts observed thermoelectric properties. Here we study the Nb–Co–Sn *hH–H* system and examine the effect of the second-phase inclusions on the properties, as well as the role played by antisite disorder.

2.2 Experimental details

A series of $NbCo_{1+x}Sn$ ($x = 0.00$, 0.05, 0.10, 0.15, 0.20) samples were prepared, as described in more detailed below. Compositions were selected to be in

the biphasic regime between the *hH* and *H* phases to maximize thermoelectric properties as illustrated by previous work on the Ti–Ni–Sn system.[38] Samples were characterized through X-ray and neutron powder diffraction, microscopy, and thermoelectric property measurements. Density functional theory (DFT) calculations were performed to examine the electronic band structure for the possible origins of the high Seebeck coefficient, as well as to approximate the value of the minimum thermal conductivity κ_{min} of NbCoSn.

To determine the effect of annealing on the structural and thermoelectric properties, samples were prepared using two different approaches, indicated as "as-prepared" (*AP*) and "annealed" (*An*). The *AP* samples were first arc-melted in an Ar atmosphere from a stoichiometric ratio of the pure elements: Nb foil (99.8%, Sigma Aldrich), Co powder (99.9%, Sigma Aldrich), and Sn shot (99.8%, Sigma Aldrich). The samples were flipped between each melt, and melted a total of three times to ensure homogeneity. The mass loss during melting was less than 2% for all samples. The *An* samples were then wrapped in Ta foil, placed in an evacuated fused silica ampoule, and submitted to an additional annealing step at 1123 K for 1 week, an annealing temperature and time common in half-Heusler preparation. Both *AP* and *An* samples were subsequently pulverized in a WC ball-mill for 5 min, and powders were then loaded in a 20 mm diameter die for further consolidation by spark plasma sintering (SPS).

Samples were pressed in the SPS for 5 minutes at 50 MPa at 1123 K. The resulting samples were approximately 7 g in mass. Electrical discharge machining was used to section samples to appropriate dimensions for measurements.

Room temperature synchrotron X-ray diffraction (XRD) data were acquired for all samples at the Advanced Photon Source at the 11-BM beamline at Argonne National Laboratory. Samples were placed in Kapton capillaries and a wavelength of 0.4592 Å was selected to avoid resonant Sn absorption. Room temperature neutron diffraction data were acquired on the POWGEN diffractometer at Oak Ridge National Laboratory for $x = 0.00$ *AP* and $x = 0.00$, 0.15 *An* samples. Samples were loaded into 6 mm vanadium cans and data was collected for approximately 2 h per sample. Refinement of all diffraction data was completed using the Rietveld method as implemented in the GSAS-EXPGUI suite of programs.[46, 47] Sn occupancy was held at 1 while allowing the Co and Nb site occupancies to vary. Crystal structures were visualized using VESTA.[48]

The microstructure of each sample was examined by removing a small piece from the bulk sample, mounting it in epoxy, and polishing with SiC and then with diamond suspension, finishing with 0.25 μm diamond suspension. Scanning electron microscopy (SEM) studies were carried out on a FEI XL30 Sirion FEG microscope equipped with a backscattered-electron (BSE) detector. Energy dispersive X-ray (EDX) analysis assisted in phase identification. TEM lamella

were prepared using a focused ion beam (FIB, Helios, FEI). Detailed investigation of microstructure was conducted in Tecnai G2 sphera TEM (FEI) operating at 300 keV.

Electrical transport properties (electrical conductivity and Seebeck coefficient) were measured on 2 mm $\times$ 2 mm $\times$ 8 mm bars on an ULVAC ZEM-3 instrument under 0.1 atm of He from room temperature to 873 K and back to room temperature. Measurements were performed twice to verify results. A Netzsch LFA 457 instrument was employed to measure thermal diffusivity using the laser flash method, between room temperature and 1123 K. Dense pellets were used for the measurements and a graphite spray was applied before measuring to minimize emissivity errors. As the electrical and thermal transport properties were measured at different temperature intervals, zT was calculated by interpolation of the thermal conductivity to the same temperatures as the electrical transport measurement.

The electronic structure of *hH* NbCoSn was calculated using density functional theory (DFT) as implemented in the Vienna *ab initio* Simulation Package (VASP)[49, 50] with projector-augmented wave (PAW) pseudopotentials.[51, 52] For structure optimization and band structure calculations, the Perdew-Burke-Ernzerhof (PBE) exchange-correlation functional within the generalized gradient approximation (GGA-PBE) was employed.[53] The standard primitive

unit cell of the conventional face-centered orthorhombic cell was obtained using AFLOW.[54] A Γ center k-mesh of 8×8×8 was employed. Additional calculations of the density of states (DOS) employed the HSE06 screened hybrid functional.[55] Calculations of κ_{min} were conducted following Clarke using the Young's modulus calculated from VASP using the Voigt-Reuss-Hill approximation. [56]

2.3 Results and discussion

2.3.1 Computational

The results of first-principles DFT calculations of the electronic structure of *hH* NbCoSn are displayed in Figure 2.2, including (a) the band structure, calculated using the PBE functional, and (b) the density of states, calculated using the hybrid HSE06 functional for greater reliability in establishing a band gap. NbCoSn is seen from DFT with GGA approximation to possess an indirect gap close to 1.3 eV. The band structure calculation suggests a band structure with a smaller band gap, closer to 1.0 eV. Given that this compound is n-type (from the Seebeck coefficient, discussed presently), it is relevant to consider the nature of the conduction band, which is largely comprised of Nb d states. The

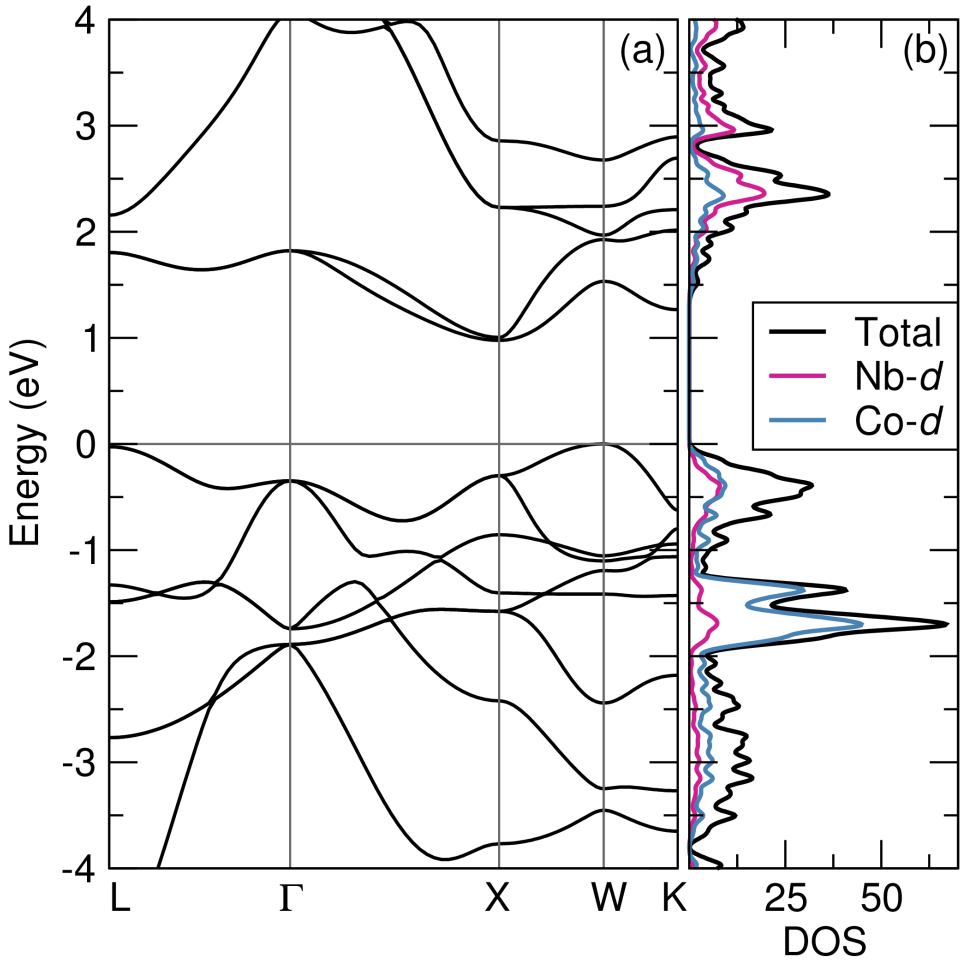

Figure 2.1: (a) PBE electronic band structure displaying an indirect band gap in *hH* NbCoSn. (b) HSEO6 density of states for NbCoSn, showing a gap of almost 1.3 eV.

conduction band minimum at the X point is doubly degenerate and relatively flat. As the Seebeck coefficient is related to the effective mass, this result may explain the relatively high Seebeck coefficient.[2] These results are in contrast with the electronic structure of the more widely studied n-type thermoelectric *hH* TiNiSn, which has a valence band minimum that is singly degenerate at the X point. DFT calculations estimate a minimum lattice thermal conductivity, κ_{min} of 0.86 W m^{-1} K^{-1}. This value is lower than experimental measurements κ approaching 4 W m^{-1} K^{-1} at 1100 K.

2.3.2 Structural characterization

In order to understand the thermoelectric properties of these compounds, it is first essential to evaluate them from a structural perspective. This was accomplished through the analysis of the average structure of the Nb–Co–Sn series through synchrotron X-ray and neutron diffraction studies. Synchrotron X-ray diffraction provides the high Q-space resolution and high signal-to-noise necessary to consider the evolution of the minor *H* phase and determine impurity phases, while neutron diffraction allows for accurate determination of site occupancies and atomic displacement parameters (ADPs, reported as U_{iso}). Together, these techniques can provide a detailed description of the structural phases and

atomic parameters of these *hH–H* materials, in particular the average structural disorder and its role on the observed physical properties.

Synchrotron X-ray diffraction was performed on $x = 0.00$, 0.05, 0.10, 0.15, 0.20 *AP* and $x = 0.00$, 0.15 *An* samples. The results for the *AP* samples are presented in Figure 2.2, and the evolution of the *H* (220) reflection, highlighted in the right panel, corresponds to increases in x-content. Rietveld refinement of the X-ray diffraction data indicated small weight fractions of secondary phases, including Nb_3Sn, elemental Sn, and an unidentified intermetallic phase. Secondary phases (Sn and Nb_3Sn) were less than 2wt%, and were thus not included in the overall fits of the diffraction data. The *An* samples have a smaller percentage of secondary phases, indicating the additional annealing step results in the dissolution of secondary phases remnant from the melting process. In addition to phase purity, there is a slight decrease in the lattice constant with additional annealing as is indicated by a comparison of the *AP* and *An* samples where $x = 0.00$ ($a = 5.9559(1)$ Å for the *AP* material as compared to $a = 5.9510(3)$ Å for the *An*). This lattice contraction suggests the *An* samples have increased ordering, as will be shown by neutron analysis.

Powder neutron diffraction was completed at room temperature for a subset of samples ($x = 0.00$ *AP* and $x = 0.00$, 0.15 *An*). Results for the *An* samples are shown with the Rietveld fits in Figure 2.3. Key crystallographic parameters are

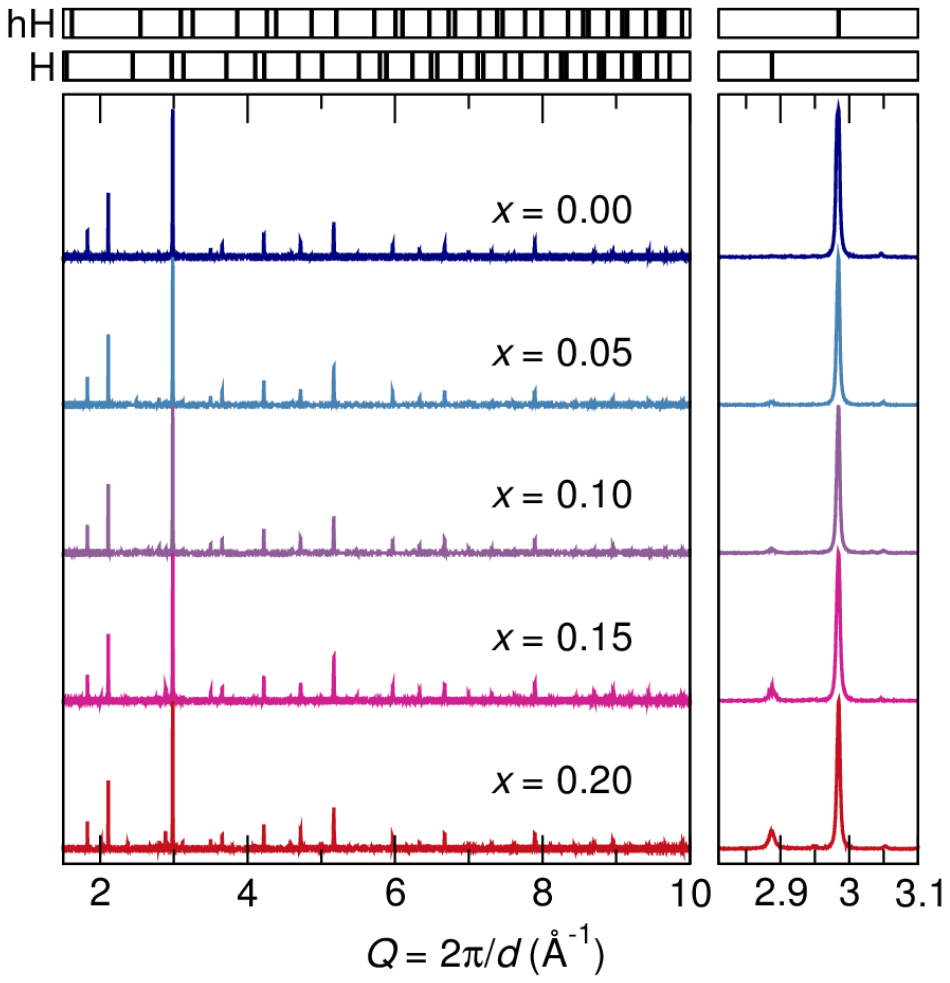

Figure 2.2: Powder synchrotron X-ray diffraction results for the as-prepared (*AP*) $NbCo_{1+x}Sn$, $x = 0.00$ through 0.20 (indicated) samples. Indexed peaks from the refined lattice constants for the *hH* $F\bar{4}3m$ and *H* $Fm\bar{3}m$ phases are shown in the top two panels. (220) peaks are shown in detail on the panel to the right, where the evolution of the *H* phase can be observed with increasing x.

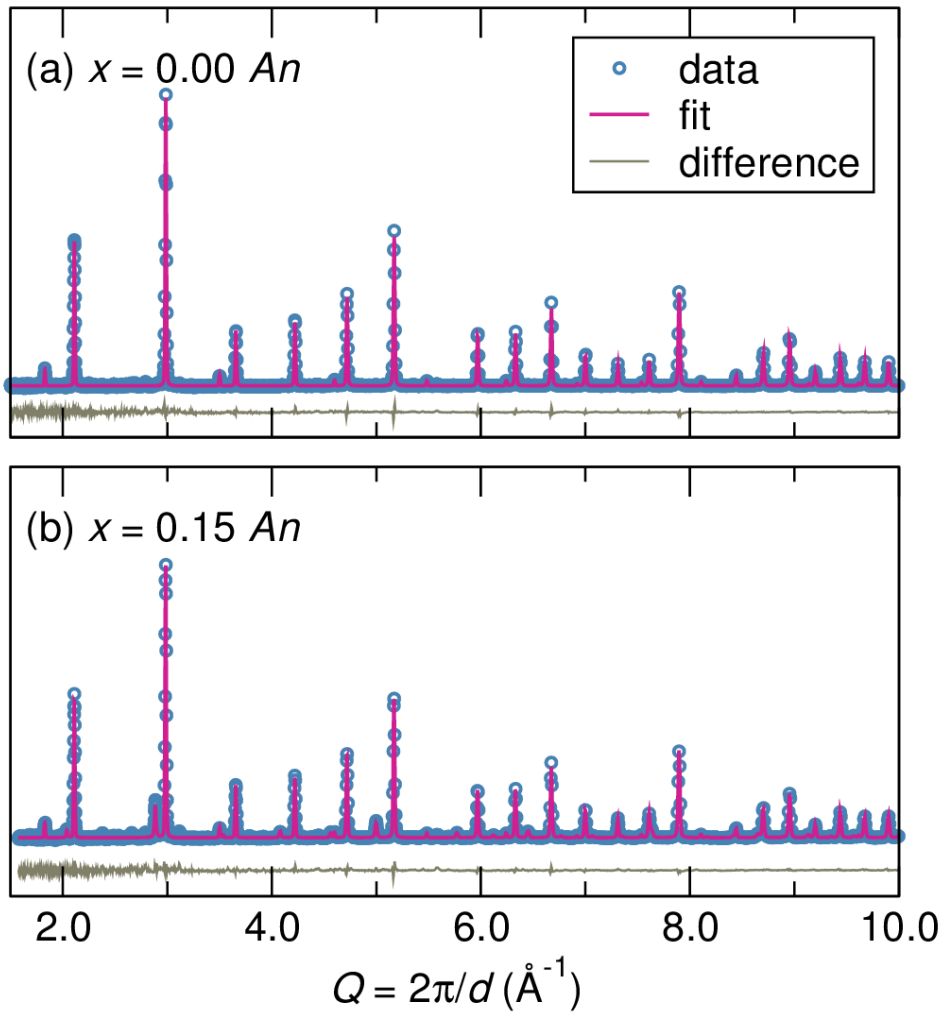

Figure 2.3: Fits obtained from the Rietveld refinement of powder neutron diffraction data for the annealed (*An*) samples of $NbCo_{1+x}Sn$, with (a) $x = 0.00$, using a single *hH* phase, and (b) $x = 0.15$ refined with *hH* and *H* phases.

Table 2.1: Structural parameters of the *hH* phase as obtained from Rietveld refinement of the neutron diffraction data, comparing *AP* and *An* samples. Note the greater degree of site-ordering in the *An* samples.

	$x = 0.00$, *AP*	$x = 0.00$, *An*	$x = 0.15$, *An*
a (Å)	5.95786(2)	5.95240(2)	5.95301(2)
Nb U_{iso}	0.0035(5)	0.00288(3)	0.0038(4)
Co U_{iso}	0.0030(2)	0.0031(2)	0.0025(2)
Sn U_{iso}	0.0029(4)	0.0032(4)	0.0018(3)
Occ. Nb_{Nb}	0.90(2)	0.97(2)	1
Occ. Co_{Co}	1	1	1
Occ. Sn_{Sn}	1	1	1
Occ. Co_{Nb}	0.10(2)	0.03(2)	0
R_{wp}	5.7%	6.2%	6.45%

compared in Table 2.1. The ADPs, presented as U_{iso}, of these compounds are similar at each of these sites, indicating that the individual atomic sites have similar degrees of structural disorder. While completing this analysis, attempts were made to introduce Co interstitials similar to the Ni interstitials found in vacant tetrahedral sites of the TiNiSn system. However, these attempts resulted in the Co interstitial to have unreasonably large U_{iso} values, suggesting it to be an unfit model. While both of the $x = 0$ compounds have excess Co on the Nb $4a$ Wyckoff sites, this substitution is most evident in the *AP* sample as compared to the *An* samples. Additionally, occupancies of the annealed $x = 0.15$ compound indicates that the addition of the secondary *H* phase may encourage site ordering. Thus, the *An* samples have a higher degree of site ordering (*i.e.*, Co and Nb are occupying their predicted sites) in addition to having a higher phase purity.

Figure 2.4 compares the *hH* lattice constant, *H* lattice constant, and *H* mole fraction with respect to x. The synchrotron X-ray data indicates that the lattice constants of both phases are independent of composition in the range studied, indicating that the the addition of extra Co to the hH phase contributes to the formation of the H phase and not to the introduction of Co-interstitials in the hH phase. This result contrasts the lattice constant expansion found in the Ti–Ni–Sn system with the addition of Ni. [38] Furthermore, there is no evidence of peak splitting, as found in TiNiSn, that results from an extra phase with Ni

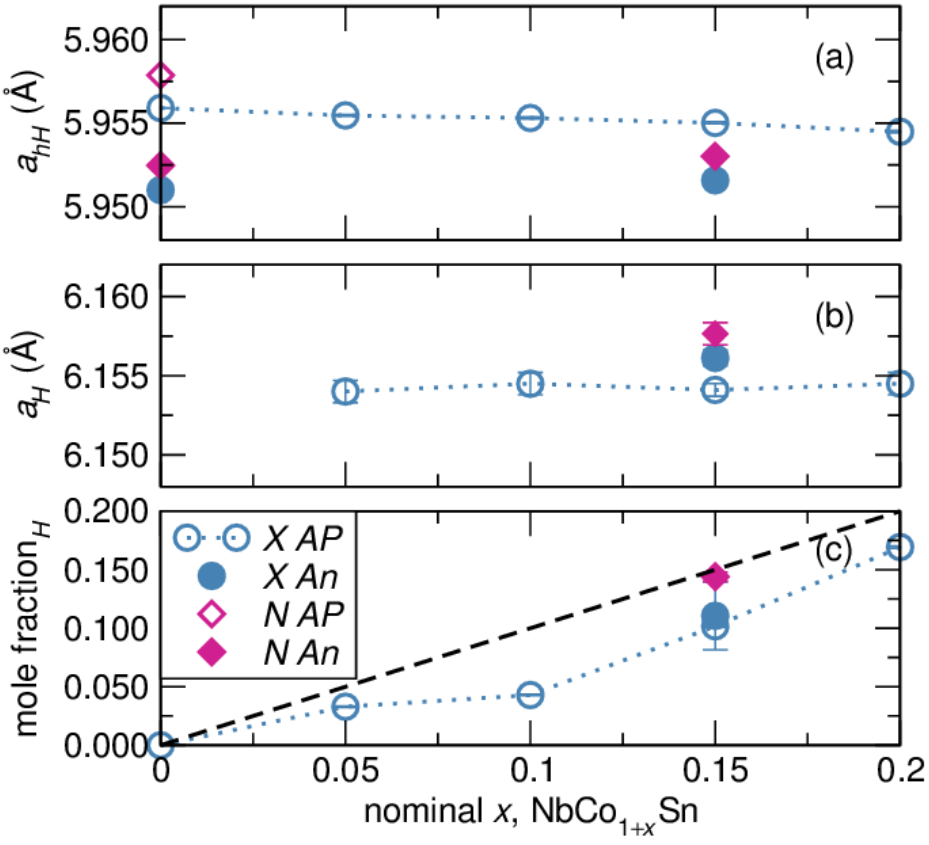

Figure 2.4: Summary of physical property results from refinements (a) The lattice constant of the *hH* shows limited variation with x. Annealing is seen to yield samples with smaller lattice parameters, as a consequence of greater site ordering. (b) The *H* lattice constant is also not dependent upon x, but in contrast to *hH*, increases upon annealing. (c) The mole fraction of the *H* phase is close to the value expected from starting compositions. Results from powder synchrotron X-ray diffraction are denoted by *X*, and from powder neutron diffraction by *N*.

interstitials.[36] Figure 2.4(c) compares how the refined mole fraction of the *H* phase varies with nominal x. These results indicate that the *H* phase emerges near the 1:1 ratio with regards to the nominal compositions.

From these results, it is concluded that, regardless of annealing, as x is increased, the *H* phase will form as a second phase alongside the *hH* phase. Additionally, the extra annealing step in preparation of the *An* samples increases the site ordering of the *hH* phase as shown through a decrease in lattice constant and the degree of substitution of Co on the Nb sites. These results contrast the interstitial defects found in the TiNiSn system, exemplifying the variable forms of structural disorder that may appear within the Heusler family.

2.3.3 Microscopy

In addition to exploring the proportions of the phases and ordering in *hH* and *H* compounds, the microstructure of this biphasic compound has been studied to evaluate the interfaces between the two phases. Representative SEM micrographs are given in Figure 2.5, where it is apparent that the $x = 0.00$ *An* compound is entirely the *hH* phase, as shown in frame (a). Regions of Sn impurities can be identified by their bright appearance. Particles of *H* evolve with Co addition, as shown in frame (b) evaluating the $x = 0.15$ *An* sample. Dark

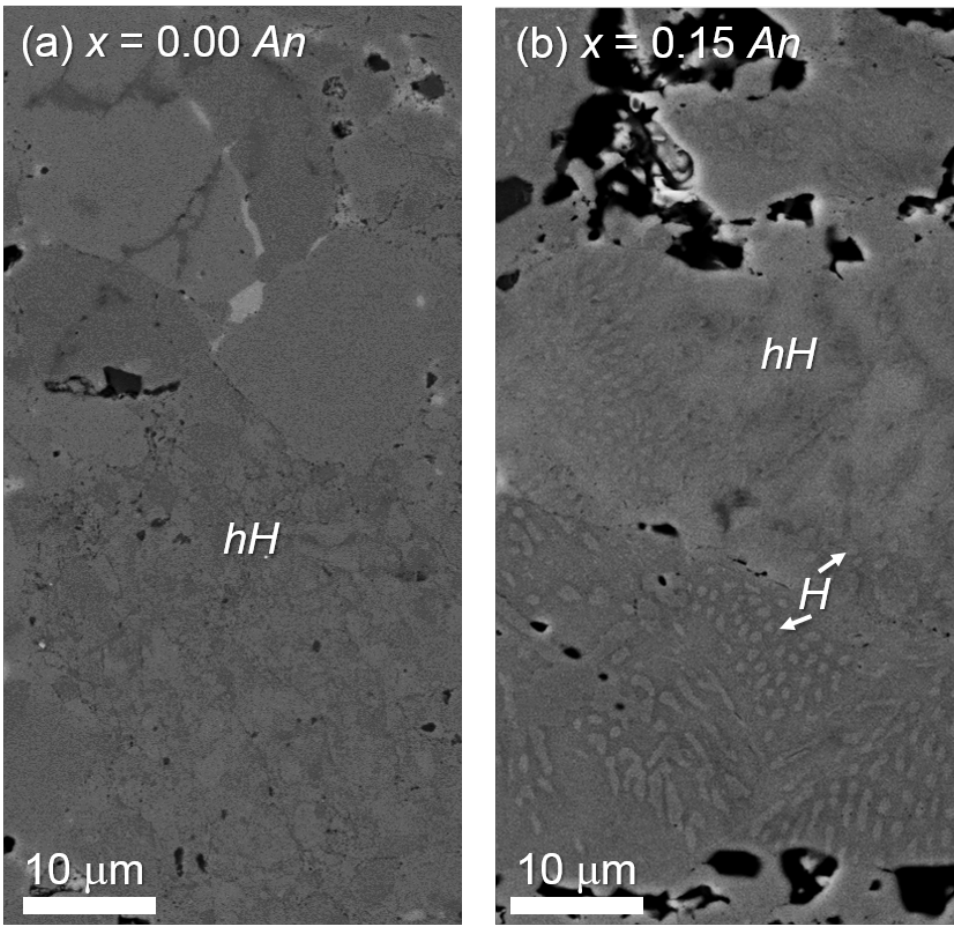

Figure 2.5: SEM BSE results indicate the evolution of the H phase through increasing x, regions of H and hH phases are labeled alongside bright regions of Sn impurities. Micrograph (a) of $x = 0.00$ is almost entirely the *hH* phase. Grains in the lower portion of this figure are NbCoSn, as confirmed by EDX. Micrograph (b) of $x = 0.15$ shows the biphasic nature of the *H* phase through the addition of excess Co. The region shown in (b) was further evaluated by TEM, shown in Figure 2.6. A pore is visible near the top of this image.

regions of micrographs are pores that formed during sample preparation. These *H* inclusions become large in the $x = 0.20$ *AP* sample. Intermediate compositions ($x = 0.05$, 0.10) show similar *H* features as $x = 0.15$, but are less frequent. Comparison of *An* to *AP* samples indicates a reduction in impurity phases, such as Nb_3Sn and Sn upon the introduction of the annealing step.

The TEM image of lamella taken from the two-phase region indicated in Figure 2.5(c) is shown in Figure 2.6 and clearly reveals the presence of precipitates with sizes ranging from the nanometer to micron scale. A range of precipitate size will scatter phonons at a range of wavelengths, maximizing the reduction of κ. [42] The brighter particle is confirmed by EDX to be the *H* phase and the darker matrix as *hH*. The bright field TEM, Figure 2.6, is labeled to indicate the location for diffraction analysis. Selected area electron diffraction pattern (SAED) taken from the *H* phase, the *hH* phase, and the interface between the two indicates the same crystallographic orientation. This suggests a cube-on-cube orientation relationship between the *H* precipitates and the *hH* matrix with semi-coherent interfaces, which is expected due to their similar crystal structure and lattice parameter 3% misfit. Coherent interfaces are shown to significantly reduce the thermal conductivity without affecting the electrical conductivity, which is critical in designing a highly efficient thermoelectric material. [57]

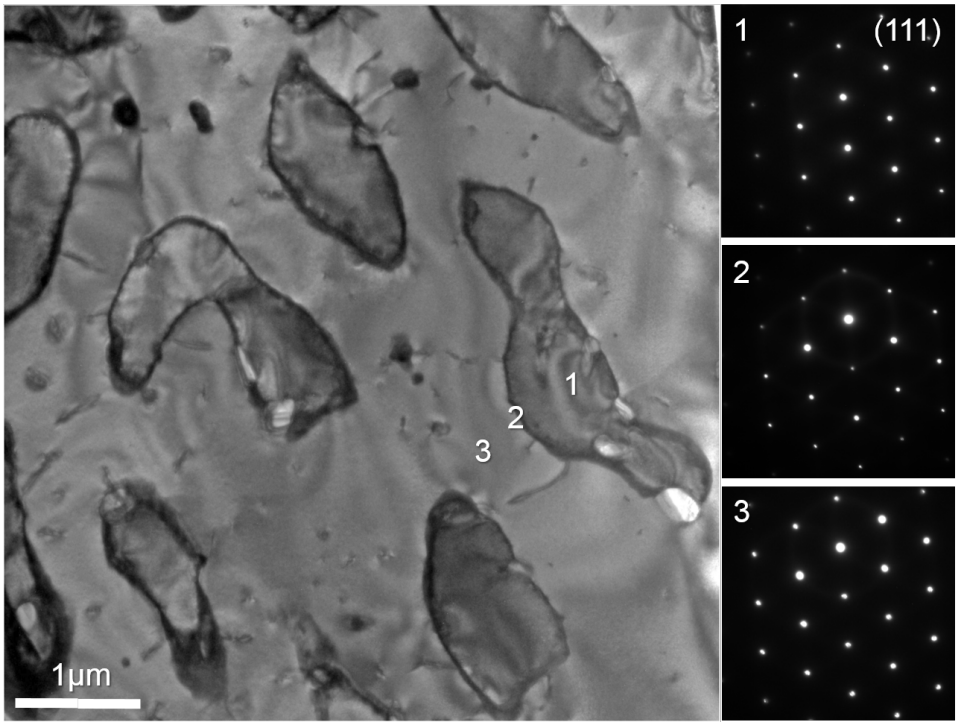

Figure 2.6: TEM micrograph highlighting the interface formed between the *H* and *hH* phases in the annealed $x = 0.15$ sample. The section was taken from the lower right region of Figure 2.5(b). Selected area electron diffraction patterns are displayed at right for regions 1, 2, and 3 as indicated on the micrograph. These suggest the interface between the *hH* and *H* phases is semi-coherent.

2.3.4 Physical properties

To determine the thermoelectric properties of the biphasic materials, a series of high temperature transport measurements were completed. The electrical resistivity (ρ), shown in panel (a) of Figure 2.7, indicates metallic behavior for all samples, as shown by the positive slope in the temperature dependence of the resistivity. This is in contrast to the semiconducting behavior of the *hH* compound as predicted through DFT. Since these calculations were performed on a perfectly ordered system, discrepancies can be attributed to the varying amounts of site ordering evidenced by the analysis of the diffraction data. A similar antisite disorder effect was proposed by Ono *et al.*,[43] who also predicted semiconducting behavior but observed metallic conductivity for samples of $NbCoSn_{1-x}Sb_x$. Additionally, we can observe that resistivity generally decreases with increasing x. In addition to compositional effects, an increase in the temperature dependence of the resistivity was observed for both *An* samples, in particular, the $x = 0.00$ *An* sample has a comparatively high electrical resistivity to the rest of the series. These observations can be attributed to the high degree of ordering present in the *An* sample, allowing it to be closer to its theoretical semiconducting state.

The Seebeck coefficient S is illustrated in panel (b) of Figure 2.7. The mag-

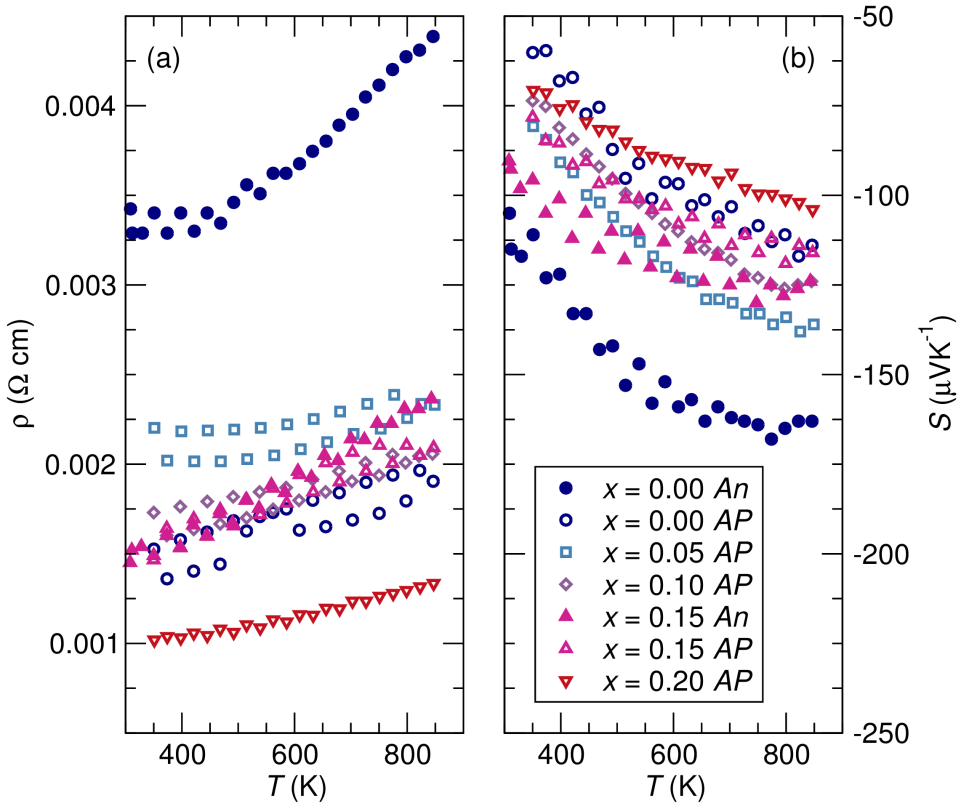

Figure 2.7: (a) Electrical resistivity indicates that the $x = 0$ samples do not display the expected semiconducting behavior. An increase in metallic character is observed with increasing x while the (b) Seebeck coefficient generally decreases in magnitude with x. Annealing increases the resistivity of samples, suggesting the role of higher site ordering.

nitude of the Seebeck coefficient decreases with increasing *H* content. The $x = 0.00$ *An* (no *H* phase) sample shows the largest magnitude in Seebeck coefficient, particularly when compared with the *AP* sample. This can be explained by the higher degree of ordering in the *An* sample as indicated by the structural characterization of these compositions.

The electrical resistivity is proportional to the magnitude of the Seebeck coefficient as both are dependent on carrier concentration. [2] This phenomenon is evident in this material system by observing that the sample with the lowest resistivity ($x = 0.20$ *AP*) is also the one with the lowest magnitude in Seebeck coefficient. Conversely, the sample with the highest resistivity ($x = 0.00$ *An*) has the largest magnitude in Seebeck coefficient. Therefore, as shown in Figure 2.8, varying x results in a limited change in the Power Factor, $S^2\rho^{-1}$.

Trends in the thermal conductivity, κ, as a function of temperature for $x = 0.00$, 0.15 (*An, AP*) are summarized in Figure 2.9. The lattice contribution to thermal conductivity is shown for $x = 0.00$ *An* and $x = 0.15$ *AP*, as determined by subtracting the electronic contribution to thermal conductivity, as calculated by the Widemann-Franz law, from the experimental thermal conductivity.[58] A Lorenz number of $2.44 \times 10^{-8} W\,\Omega\,K^{-2}$ was used. It can be observed that the addition of the *H* phase results in a decrease in κ over all temperature ranges. This is expected as the introduction of a secondary phase will disrupt the coherence

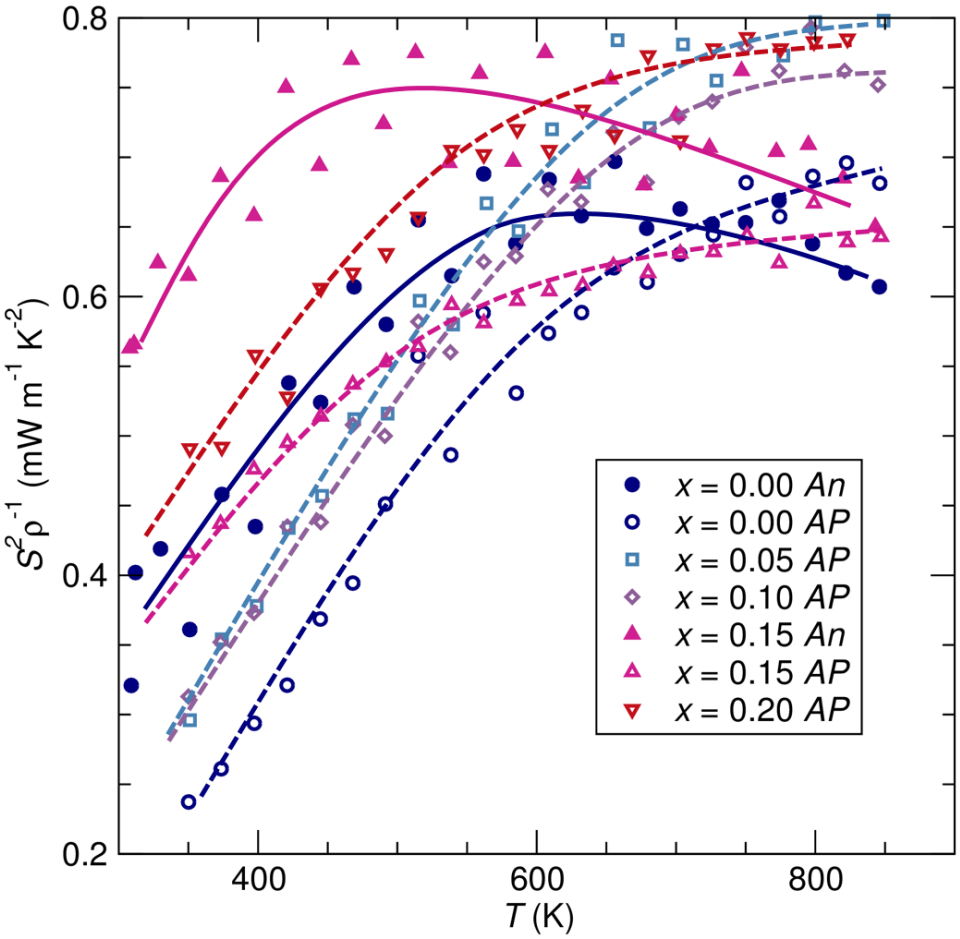

Figure 2.8: The thermoelectric power factor, $S^2\rho^{-1}$ displayed for the different *AP* and *An* samples, as a function of temperature. At the highest temperature measured, there is a general trend towards a high power factor, suggesting that the decreased resistivity with increasing x, both for the *AP* and *An*, plays a greater role than changes in the Seebeck coefficient.

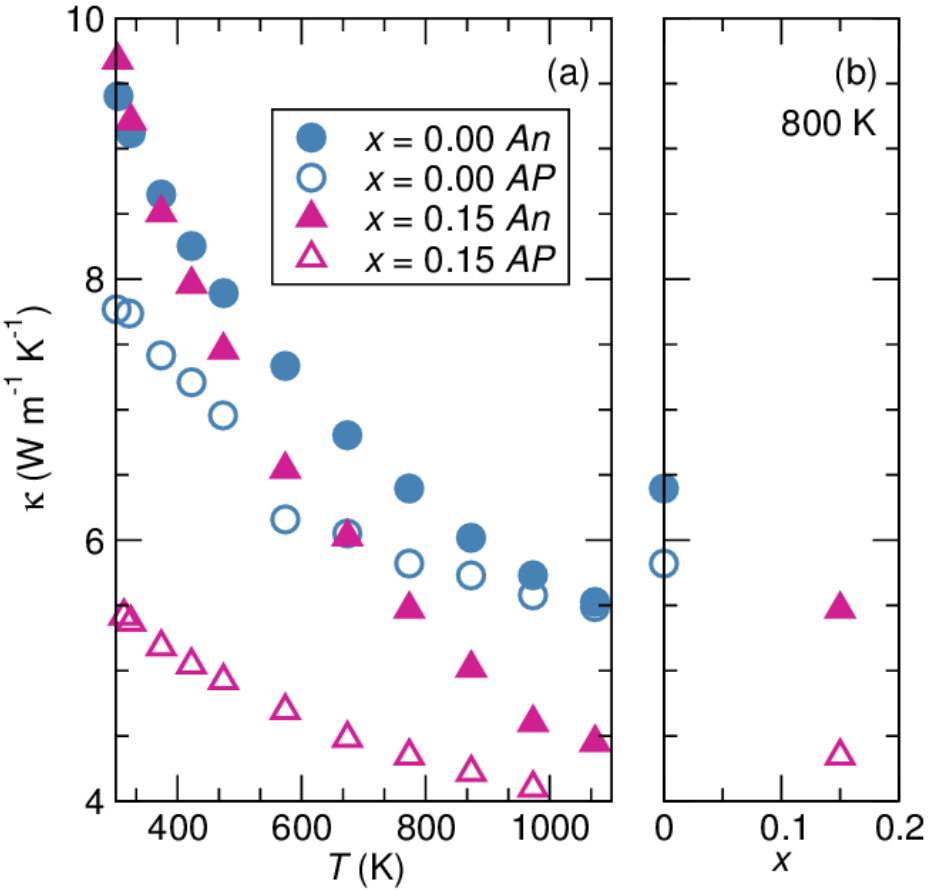

Figure 2.9: Thermal conductivity (κ) for $x = 0.00$, 0.15 samples as (a) a function of temperature and (b) a function of x at 800 K. It is observed that both the absence of the additional annealing step and the inclusion of the secondary *H* phase reduces κ.

of the material, resulting in less efficient phonon transport. Quantitatively, there is a 25% decrease in κ from $x = 0.00$ *AP* to $x = 0.15$ *AP* at 800 K. For both compositions, the *AP* samples have a lower κ than the *An* samples. This is attributed to both an increase in phase purity and site ordering induced by the annealing step, which decreases the amount of phonon scattering centers in the material. With κ reduction from both disorder and the secondary *H* phase, $x = 0.15$ *AP* exhibits the lowest κ. However, the κ of the *AP* samples approaches that of the *An* samples at higher temperatures, suggesting that with thermal cycling, performance of the *AP* will be closer to that of the *An* samples. Therefore, the most effective method for lowering κ is the inclusion of the secondary *H* phase.

The zT metric ($zT = [S^2/(\kappa\rho)]T$) for $x = 0.00$, 0.15 (*An, AP*) is shown in Figure 2.10. It is observed that zT reaches a maximum of 0.122 at 822 K for the $x = 0.15$ *AP* sample. As the power factors for all studied materials are similar at this temperature, the enhanced zT is attributed primarily to the reduction of κ. Comparing the maximum zT of the annealed, thermally stable, samples indicates 20% improvement in the thermoelectric figure of merit upon the introduction of $NbCo_2Sn$ inclusions. This confirms that the addition of a secondary phase is an effective method for optimizing the thermal aspects of the thermoelectric performance of these *hH-H* systems.

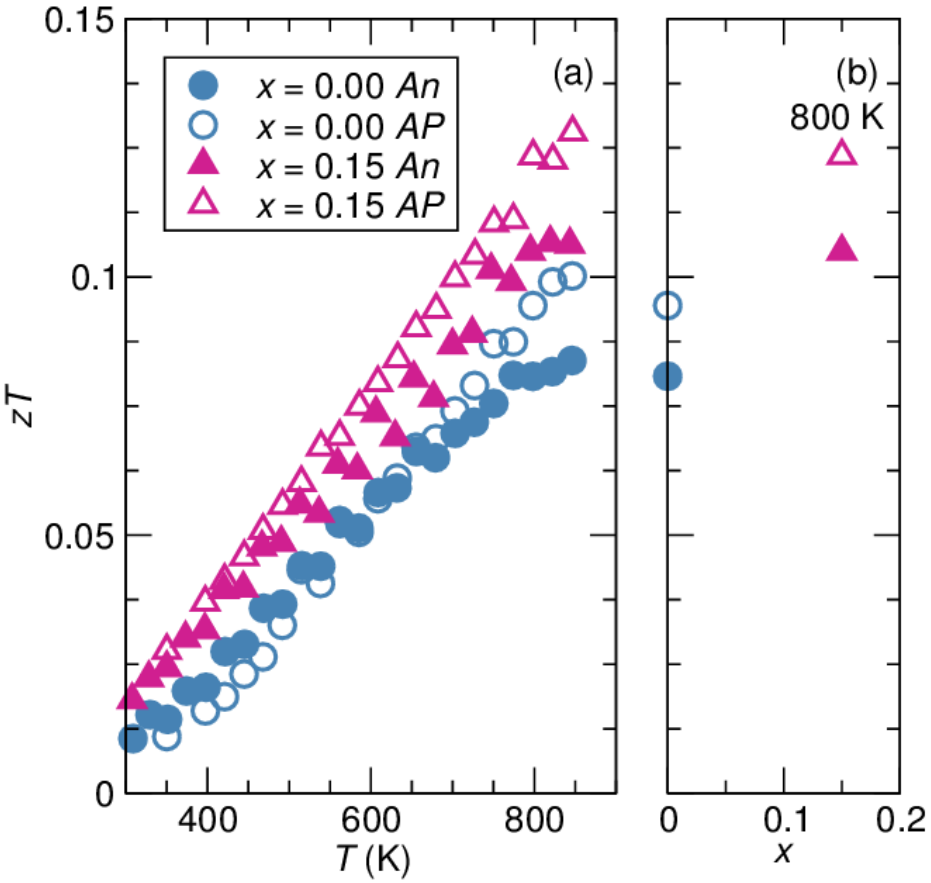

Figure 2.10: Thermoelectric figure of merit, zT, of $x = 0.00$ and 0.15 as a function of (a) temperature and (b) x at 800 K. The largest zT was shown for $x = 0.15$ *AP* at 822 K, which is attributed primarily to the reduction in κ with the addition of a secondary*H* phase.

2.4 Conclusion

In summary, we have shown that *hH* compound NbCoSn will develop a biphasic structure with *H* $NbCo_2Sn$ through the introduction of excess Co. TEM shows the resulting interface is semi-coherent in nature. Two different preparation approaches, one which included a high temperature anneal, permitted the examination of antisite defects and their influence on transport properties relevant to thermoelectric performance. In contrast to TiNiSn, results indicate that additional Co does not sit in the tetrahedral vacancies of the hH lattice, but may occupy Nb sites without a high temperature anneal. The annealed, highly ordered, compounds exhibit electrical resistivity closer to theoretical semiconductor behavior, while the experimentally examined compounds with antisite defects exhibit a reduction in thermal conductivity that, particularly in the biphasic compound, resulted in a thermal conductivity reduction and improvement in thermoelectric figure of merit, zT.

Chapter 3

Thermoelectric performance and the role of anti-site disorder in Heusler $TiFe_2Sn$

Heusler compounds XY_2Z with 24 valence electrons per formula unit are promising thermoelectric materials due to their thermal and chemical stability, preparation from relatively earth-abundant elements, and favorable electrical properties. First principal calculations recently published on $TiFe_2Sn$ have proposed this compound to be of thermoelectric interest due to a flat conduction band that would enable an enhanced Seebeck coefficient with electron dop-

ing. In light of this refueled interest in $TiFe_2Sn$ as a thermoelectric material, we present new experimentation that probes $TiFe_2Sn$, namely high temperature physical property measurements and average structure refinements from synchrotron X-ray and neutron diffraction data. Our findings evaluate deviations from a 1:1 Ti–Fe ratio ($Ti_{1+x}Fe_{2-x}Sn$ where $x = -0.10,\ -0.05,\ 0,\ 0.05,\ 0.10$) concluding that Ti–Fe anti-site defects are present in the stoichiometric compound and that these defects are reduced in the Ti–rich compound. Additionally, we present investigations into the Seebeck coefficient through the introduction of Sb onto the Sn site ($TiFe_2Sn_{1-y}Sb_y$ where $y = 0.01,\ 0.05$). Results do not reveal an enhanced Seebeck coefficient with Sb doping due to the anti-site defects present in this system.

3.1 Introduction

Recent theoretical studies considering the Heusler compound $TiFe_2Sn$ suggests that the Seebeck coefficient of this compound could be enhanced through n-type doping.[59] These predictions are reasonable considering literature on the Heusler compound VFe_2Al, a relatively well explored compound that has been of interest since the discovery of unusual temperature dependence of electrical resistivity[60] that is accredited to a pseudogap at the Fermi level.[61, 62]

VFe_2Al displays a large Seebeck coefficient ($|S| > 150\,\mu$V/K) upon varying the VEC slightly from 24. Techniques for this have included introducing Ge[63] or Si[64] to the Al site, varying the V–Al ratio,[65–67] and varying the Fe–V ratio.[68, 69] Considering that both $TiFe_2Sn$ and VFe_2Al are 24 VEC Heusler compounds, these high Seebeck predictions for $TiFe_2Sn$ are compelling. In contrast to VFe_2Al, $TiFe_2Sn$ is a less explored compound, and existing literature on $TiFe_2Sn$ has not indicated significant improvements in Seebeck coefficient upon varying the Ti–Fe ratio.[70, 71] This discrepancy between calculations and experimental results is likely the result of anti-site defects between the Ti–Fe elements, as has been evaluated by lab X-ray diffraction and Mössbauer, [72–74] that were not included in the high Seebeck coefficient predictions.[59] These anti-site defects are in the form of Ti occupying Fe sites (Ti_{Fe}) and as Fe occupying Ti sites (Fe_{Ti}). However, no high temperature physical property measurements, synchrotron X-ray, or neutron diffraction data have been reported for $TiFe_2Sn$.

To examine these predictions of a high Seebeck coefficient in $TiFe_2Sn$, we present novel data on the high temperature thermoelectric performance of $TiFe_2Sn$, detailed structural refinements from synchrotron X-ray and neutron diffraction, and a study on Sb substitution for Sn. By completing joint Rietveld refinements of synchrotron X-ray and neutron diffraction, the structural studies

presented in this work add significant evidence to the nature of disorder in the $TiFe_2Sn$ system. Our work uses two different approaches to evaluate $TiFe_2Sn$: First, we varied the Ti–Fe ratio as $Ti_{1+x}Fe_{2-x}Sn$ to evaluate the impact this ratio has on structural site ordering. Second, we explored the effect that substituting Sb for Sn, $TiFe_2Sn_{1-y}Sb_y$, has on thermoelectric performance, examining predictions that a high Seebeck in $TiFe_2Sn$ will manifest with n-type doping.[59]

3.2 Methods

Two series of compounds based on $TiFe_2Sn$ were prepared. One set of compounds modified the Ti–Fe ratio in the form $Ti_{1+x}Fe_{2-x}Sn$ ($x = -0.10$, -0.05, 0, 0.05, 0.10) to determine how off-stoichiometry impacts site ordering and thermoelectric properties. A second set of compounds were prepared by doping the Sn site with Sb as $TiFe_2Sn_{1-y}Sb_y$ ($y = 0.01$, 0.05) to experimentally explore calculation-based reports of an enhanced Seebeck coefficient with n-type doping.[59]

All samples were prepared using a three step processing method: arc-melting, annealing, and spark plasma sintering (SPS). Arc-melting was conducted in an inert Ar atmosphere from a stoichiometric ratio of the pure elements: Ti foil (99.7%, Sigma Aldrich), Fe chips (99.98%, Sigma Aldrich), Sn

shot (99.8%, Sigma Aldrich), and Sb shot (99.999%, Alfa Aesar). The resulting button was wrapped in Ta foil, sealed in a silica ampule under a partial pressure of Ar, and annealed for one week at 1123 K from which the button was slow cooled. Following the anneal, the button was ground to a fine powder using a mortar and pestle. This powder was pressed in the SPS for 8 minutes at 61.5 MPa and 1123 K to produce a puck approximately 9.1 mm in diameter. Final samples were roughly 1.5 g in mass. Bars for physical property measurements of approximate dimensions $6 \times 2 \times 3$ mm were sectioned by electrical discharge machining. Remaining sections were selected for electron microscopy measurements.

Band structure calculations of $TiFe_2Sn$ were conducted utilizing density functional theory (DFT) as implemented in the Vienna ab initio Simulation package (VASP),[49, 50] complete with projector-augmented wave (PAW) pseudopotentials.[51, 52] The Perdew-Burke-Ernzerhof (PBE) exchange correlation functional was applied in structure optimization and band structure calculations within the generalized gradient approximation (GGA-PBE).[53] A Γ center k-mesh of $8 \times 8 \times 8$ was applied to these calculations.

Powder samples for $x = -0.10$, -0.05, 0, 0.05, 0.10 and $y = 0.01$, 0.05 were sealed in Kapton capillary tubes and synchrotron XRD data was measured at 295 K for all samples on the 11-BM beamline at the Advanced Photon Source

at Argonne National Lab where a wavelength of 0.4593 Å was used to avoid Sn absorption. Neutron diffraction data for $x = -0.10$, 0, 0.10 and $y = 0.05$ was acquired by the POWGEN diffractometer at the Spallation Neutron Source located at Oak Ridge National Laboratory. Samples were loaded in 6 mm vanadium cans and measurements were conducted at 300 K, lasting approximately 1 hour. Rietveld refinements of diffraction data was conducted using TOPAS.[75] When possible ($x = -0.10$, 0.00, 0.10 and $y = 0.05$) joint X-ray and neutron refinements were completed to maximize available statistics. The $TiFe_2Sn$ crystal structure was visualized using VESTA.[48]

Electron microscopy was completed on pieces removed from the bulk sample. The piece was mounted in epoxy, ground with SiC paper, and then polished with diamond suspensions down to 0.25 μm. Scanning electron microscopy (SEM) was conducted on a FEI XL30 Siron FEG equipped with a backscattered-electron (BSE) detector operating at 15.0 kV. Phase identification was supported by energy dispersive X-ray (EDX) analysis.

High temperature electrical transport properties (Seebeck coefficient, S, and electrical resistivity, ρ) were measured utilizing a ULVAC ZEM-3 instrument. Measurements were conducted under 0.1 atm of He and consisted of heating the sample from 300 to 850 K and cooling to 300 K. Measurements were taken every 50 K and results collected on cooling are presented.

3.3 Results and discussion

Computational

First-principal DFT calculations of the electronic band structure of $TiFe_2Sn$, shown in Figure 3.1, indicate that $TiFe_2Sn$ is a semiconductor with an indirect band gap of 0.1 eV. This electronic band structure reveals a flat conduction band that rises only 0.04 eV between the conduction band minimum at X and nearby Γ. As the Seebeck coefficient is proportional to the effective mass,[2] a large Seebeck coefficient is expected with n-type doping. These calculations are consistent with literature on $TiFe_2Sn$. Yabuuchi *et al.*[59] reports a band gap of 0.07 eV and estimates that a large magnitude Seebeck coefficient ($S < -200\,\mu$V/K) would manifest upon n-type doping, on the order of 10^{21} cm^{-3}. This band structure is consistent with published band structure calculations[76–78] that also evaluate the density of state (DOS), indicating that the conduction band is primarily comprised of Fe states.

Structural characterization

In order to examine the site ordering of $TiFe_2Sn$, we performed detailed X-ray and neutron diffraction studies on deviations from pure $TiFe_2Sn$ stoichiometry.

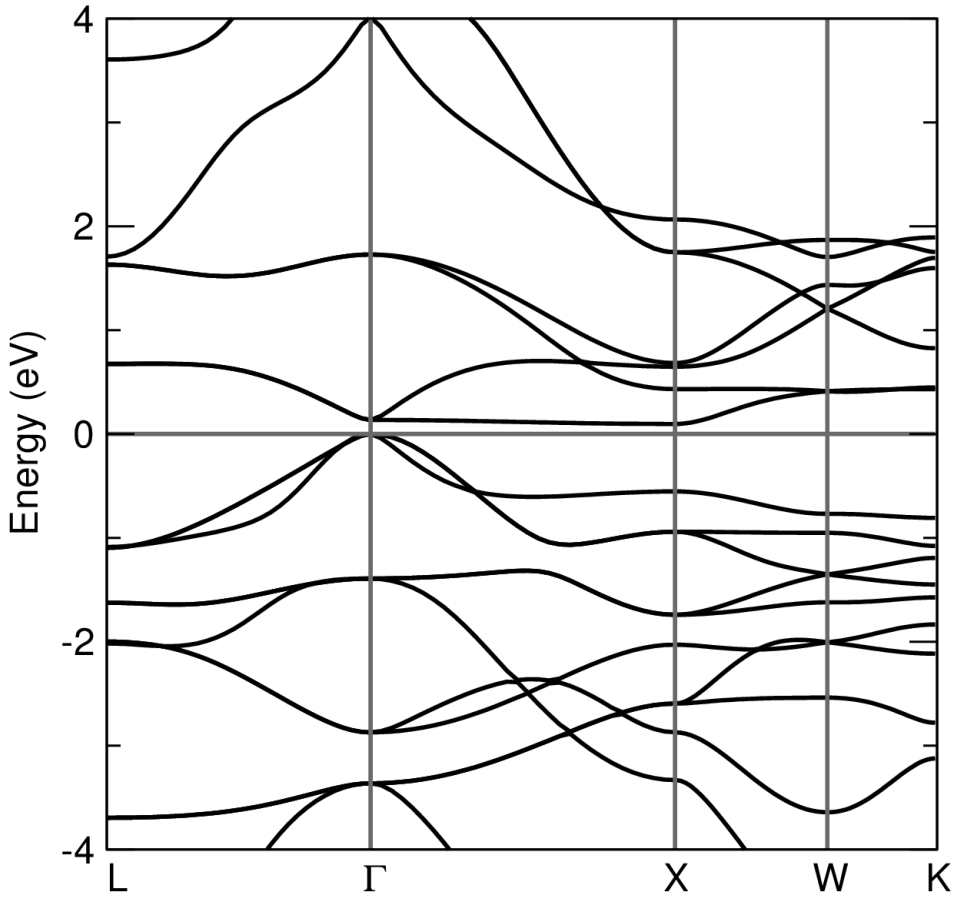

Figure 3.1: PBE electronic band structure of Heusler compound $TiFe_2Sn$. Calculations indicate the indirect band gap between X and Γ is 0.1 eV while the direct gap at Γ is 0.14 eV. The low curvature conduction band between Γ and X implies a large Seebeck coefficient may materialize with n-type doping.

Synchrotron X-ray diffraction, due to its Q-space resolution and high signal to noise ratio, allows the determination of accurate lattice parameters and identification of minor impurity phases. Neutron diffraction enables the determination of accurate site occupancies and atomic displacement parameters (reported as U_{iso}). To our knowledge, this is the first publication featuring a detailed structural analysis of $TiFe_2Sn$.

A representative fit of of neutron and X-ray diffraction patterns for $x = 0$ is shown in Figure 3.2. Rietveld refinements were conducted on X-ray data for $x = -0.05$, 0.05 and both X-ray and neutron diffraction data for $x = -0.10$, 0, 0.10. Quality of fit metric, R_{wp}, was in the range of 7 to 10% for all refinements. Impurity phases were determined by evaluating minor peaks of X-ray data, indicating that the compounds with compositions near $TiFe_2Sn$ ($x = -0.05$, 0, 0.05) did not form impurity phases. The Fe–rich sample ($x = -0.10$) contained 0.3 wt% Sn impurities, while analysis of the Ti–rich sample ($x = 0.10$) shows the formation of 0.4 wt% Sn_5Ti_6. The formation of impurity phases at extreme x values indicates that this study evaluates the full solubility limit of the Ti:Fe ratio. A subtle peak asymmetry is present in X-ray peaks, possibly suggesting a distribution of lattice parameters, as has been suggested elsewhere.[73, 74] However, fitting this asymmetry with an additional $TiFe_2Sn$ phase did not visually improve the fit or R_{wp}.

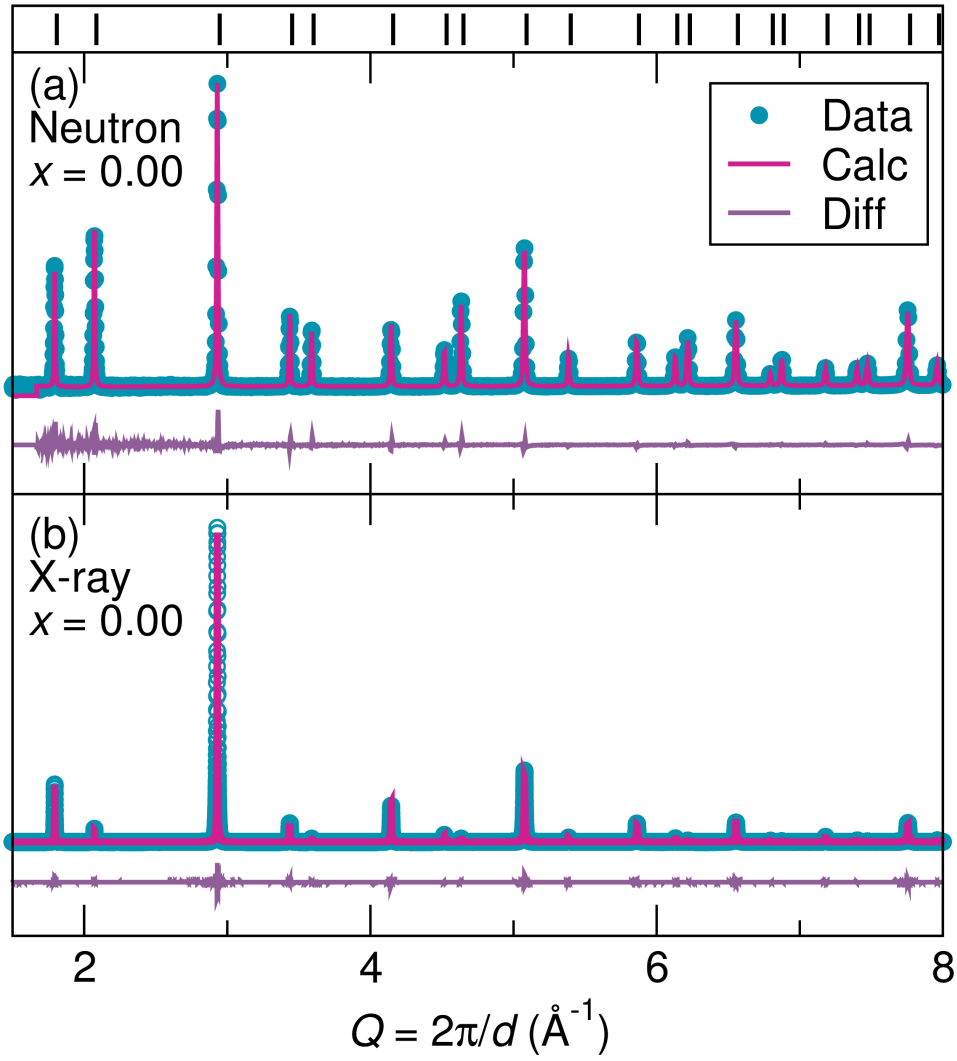

Figure 3.2: Joint fits of (a) neutron and (b) X-ray diffraction data for stoichiometric $TiFe_2Sn$ indicates sample are phase pure. Indexed peaks from the refined phase are shown in the top panel. Difference curves are plotted below each fit.

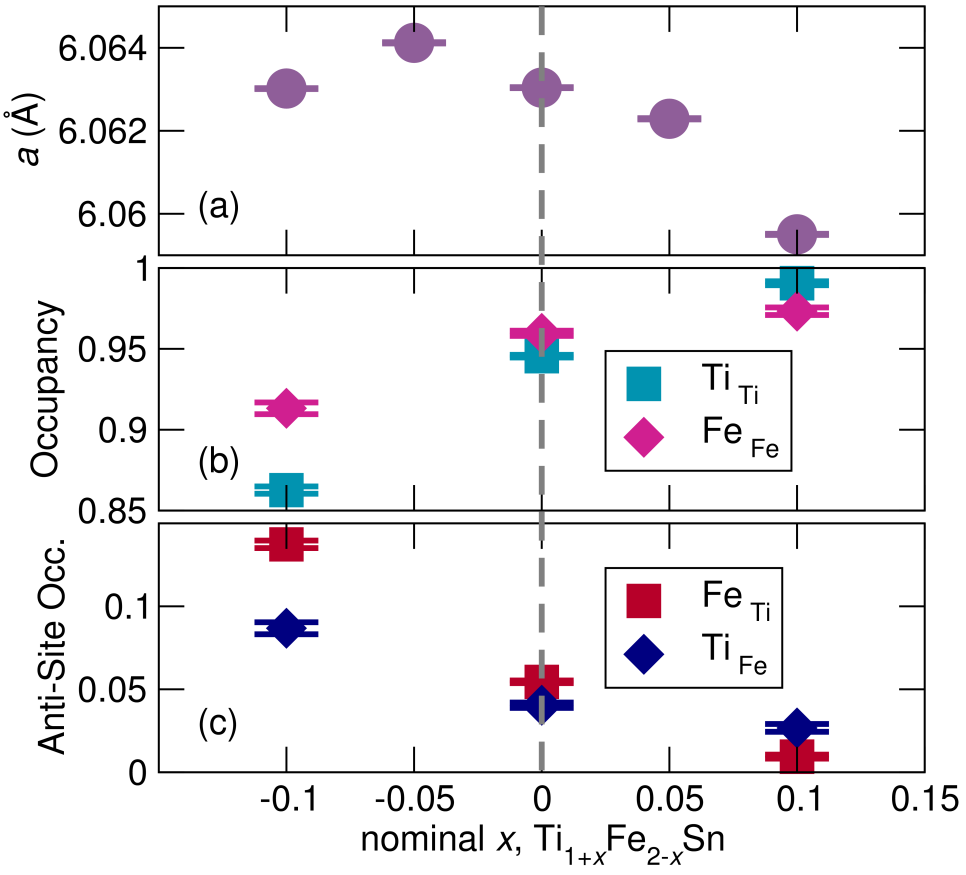

Figure 3.3: Summary of $Ti_{1+x}Fe_{2-x}Sn$ structural parameters: (a) lattice parameter (b) site occupancy (c) anti-site occupancy, illustrating that the $x = 0$ composition has Ti–Fe anti-site defects that can be reduced by using a Ti–rich composition. Data was obtained from Rietveld refinement of diffraction data ($x = -0.05$, 0.05) and joint refinement of X-ray and neutron diffraction data ($x = -0.10$, 0, 0.10).

Structural parameters, as determined by Rietveld refinements are presented in Figure 3.3. We determined a lattice parameter of 6.06304(1) Å for pure $TiFe_2Sn$ which is in agreement with the literature.[59, 74] Panel (a) of Figure 3.3 presents variations in the lattice parameter of $TiFe_2Sn$ with x, illustrating that while excess Fe ($x < 0$) either expands or barely contracts the lattice parameter, excess Ti ($x > 0$) results in a clearly contracted lattice. This result is consistent with site occupancy results illustrated in panel (b) and anti-site occupancy results shown in panel (c) of Figure 3.3. To allow the accurate determination of Ti_{Fe} and Fe_{Ti} anti-site defects, refinements were completed by constraining each atomic site to be filled (i.e. no vacancies) while allowing the site to contain both Ti or Fe atoms. The Sn occupancy was fixed to full site occupancy to reduce correlation effects. While other defect arrangements were evaluated, this methodology resulted in the best fit and the least amount of correlation between the refined parameters. The refinement of atomic displacement parameters resulted in U_{iso} values of 0.002-0.006 Å, clarifying that structural disorder (*i. e.* atoms disordered about their ideal site) does not play a large role in these compounds. These occupancy results suggest that anti-site defects are present in all samples. However, the quantity of these defects is considerably reduced for the Ti–rich, $x = 0.10$, compound. This is consistent with the contraction in lattice parameter for this compound.

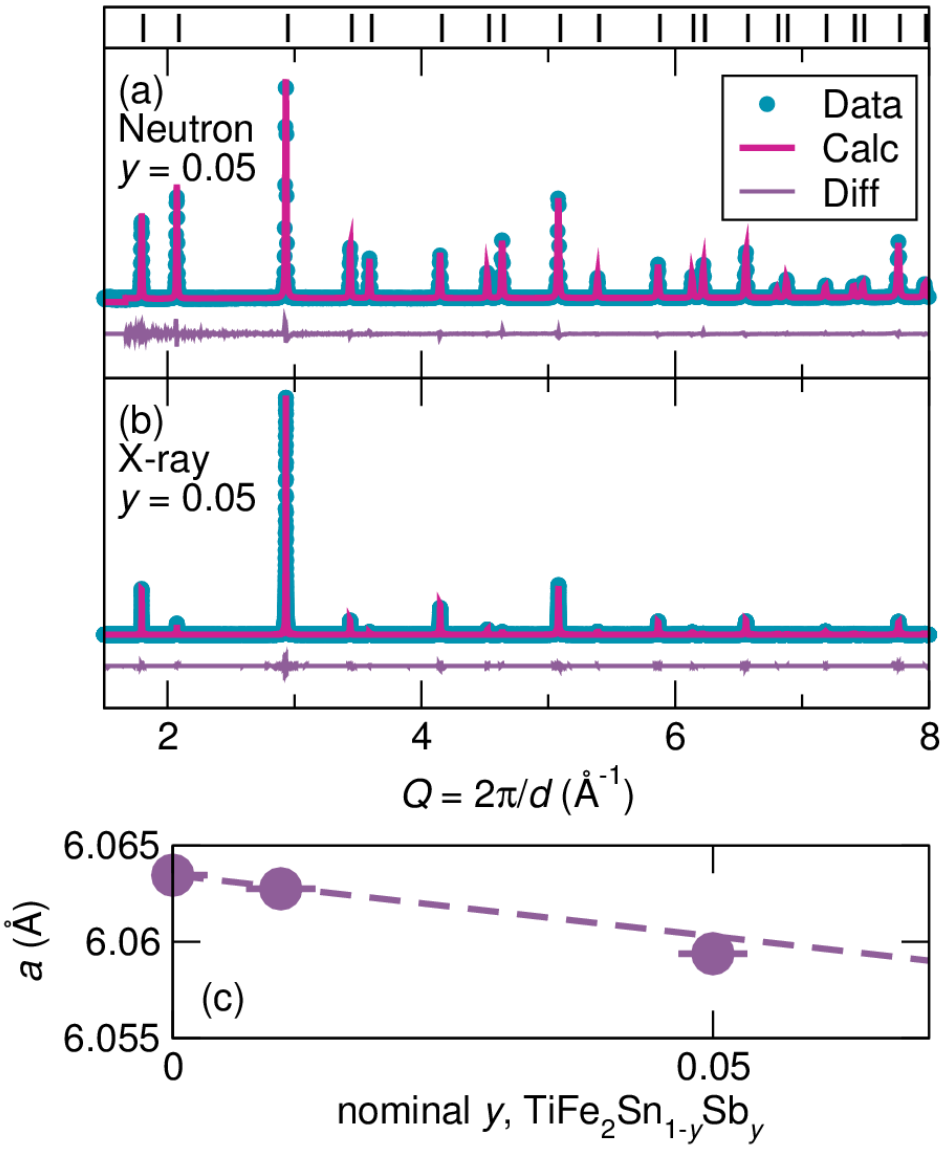

Figure 3.4: Joint refinement fits of (a) Neutron and (b) X-ray diffraction data for $TiFe_2Sn_{0.95}Sb_{0.05}$. Panel (c) indicates that the lattice parameter of $TiFe_2Sn_{1-y}Sb_y$ generally decreases with y, relating to a Vegard's law estimation of lattice parameter, indicated by the dashed line.

In addition to evaluating the effect of varying the Ti–Fe ratio in $TiFe_2Sn$, n-type doping of $TiFe_2Sn$ was attempted by the substitution of Sb onto the Sn site by preparing samples with composition $TiFe_2Sn_{1-y}Sb_y$ ($y = 0.01,\ 0.05$). Neutron and X-ray diffraction of $TiFe_2Sn_{0.95}Sb_{0.05}$ is presented in panels (a) and (b), respectively, of Figure 3.4. No impurity phases were identified in these compounds. To reduce correlation effects, Rietveld refinements were performed with Ti and Fe anti-site defects fixed to the values in Figure 3.3. Noting that these elements have similar X-ray and neutron scattering lengths, (Coh_b of 6.225 fm for Sn and 5.57 fm for Sb) occupancy refinements did not yield physically meaningful results, suggesting that refinement of site occupancies is not an effective technique for this case. However, lattice parameters, displayed in Figure 3.4(c) with respect to y, indicates that the lattice parameter of these compounds becomes smaller with y. To evaluate this decrease, a linear expression of Vegard's law[79] was calculated, utilizing a theoretical lattice parameter of Heusler $TiFe_2Sb$.[77] This line approximates the lattice constants shown in Panel (c) of Figure 3.4, indicating that the lattice contracts as expected with Sb introduction, supporting the substitution of Sb atoms onto the Sn site.

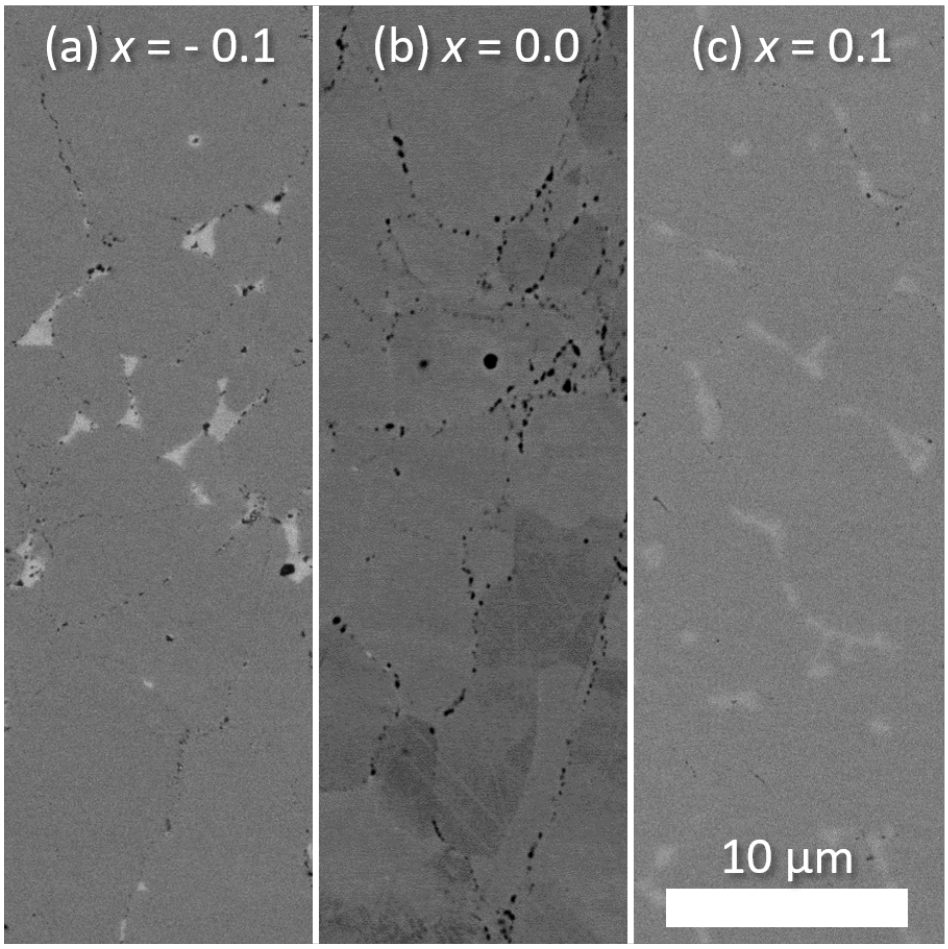

Figure 3.5: SEM BSE micrographs of $Ti_{1+x}Fe_{2-x}Sn$ for $x = -0.10$, 0.00, 0.10, in frames (a), (b) and (c), respectively, showing Z contrast between matrix and impurity phases. EDX was used to identify the matrix phase as a $TiFe_2Sn$ variation that was (a) Fe–rich or (c) Ti–rich. These variations correspond to the expected Ti–Fe ratio.

Microscopy

Microstructural analysis was performed for these materials utilizing SEM with a BSE detector to highlight Z contrast. EDX was used to examine elemental ratios, characterize matrix phase compositional changes, and resolve impurity phases. Representative micrographs were taken for a subset of samples ($x = -0.10$, 0.00, 0.10) as displayed in Figure 2.5.

EDX measurements indicate that the matrix phase of $x = -0.10$ is Fe-rich, while the atomic ratio of the matrix phase of $x = 0.10$ is Ti-rich. These EDX approximations suggest that the $TiFe_2Sn$ matrix phase corresponds to the Ti and Fe–rich extremes of the experimental design.

EDX was also employed to enable the identification of impurity phases. Utilizing X-ray diffraction to complement these results, impurity phases make up less than 1wt % of these samples. For all samples, impurity phases form near grain boundaries. In Fe-rich ($x = -0.1$) $FeSn_2$ was determined as the impurity phase, identifiable by its bright appearance in Figure 2.5 (a). This result differs from analysis of X-ray diffraction, which indicated Sn as the primary impurity phase. There were small unidentified impurity peaks in this refinement, suggesting that a $FeSn_2$–like phase with excess Ti forms such that impurity diffraction peaks became unidentifiable. For $x = 0$ (Figure 2.5 (b)) subtle Ti impurities can

be seen as dark diamond shaped regions residing between grains and is present only in trace amounts, in agreement with XRD refinements which indicates no impurities. The Ti–rich compound ($x = 0.1$) in panel (c) indicates that Sn_5Ti_6 with excess Fe–solubility is the impurity phase which, upon allowing lattice expansion for Fe–inclusion, agrees with our X-ray analysis. As the Fe–rich sample has a Fe–Sn impurity and the Ti–rich sample has a Ti–Sn impurity, these impurity phases are consistant with the experimental Ti:Fe ratio.

Physical properties

To characterize the thermoelectric performance of these materials, high temperature physical property measurements, including Seebeck coefficient (S) and electrical resistivity (ρ), were conducted. Results for $Ti_{1+x}Fe_{2-x}Sn$ ($x = -0.10$, -0.05 0.00, 0.05, 0.10) are presented in Figure 3.6, while results for $TiFe_2Sn_{1-y}Sb_y$ ($y = 0.01$, 0.05) are illustrated in Figure 3.7.

Panel (a) of Figure 3.6 exhibits trends in electrical resistivity with x as a function of temperature showing that resistivity has limited dependence on x. Room temperature resistivity values are similar to those published elsewhere,[74] and an increase in resistivity for $x = 0.10$, shown by our results, has also been observed elsewhere.[70] A transition from metallic to semiconducting behavior is

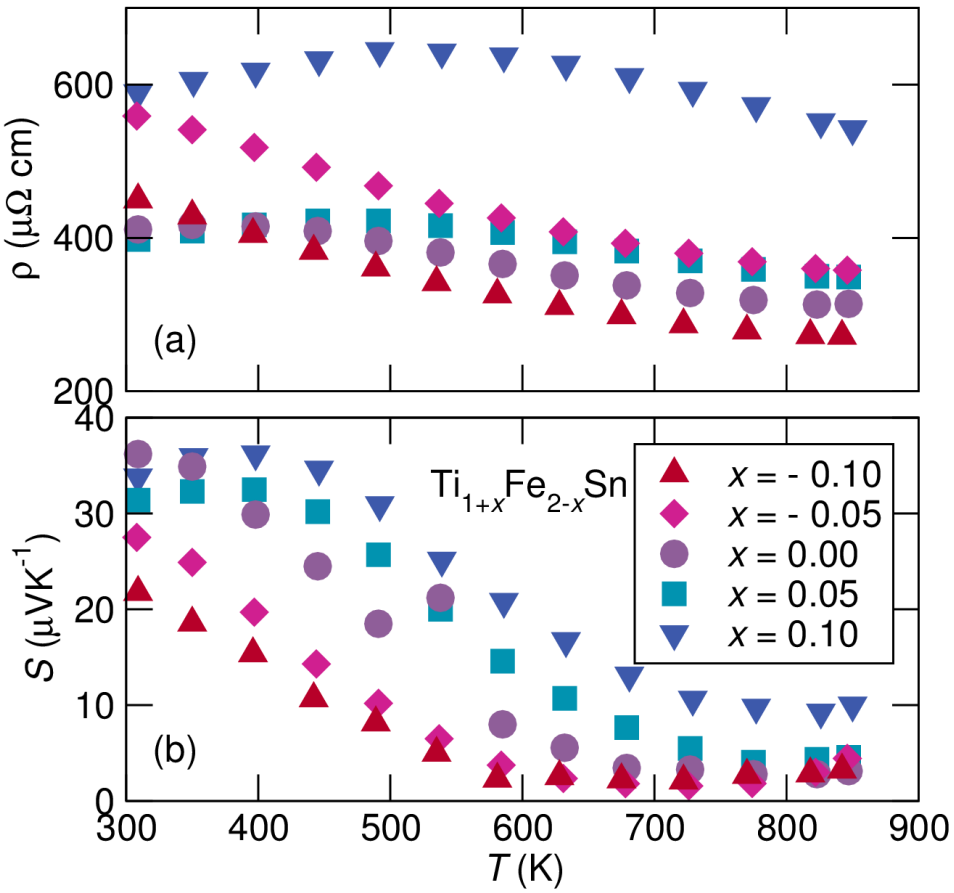

Figure 3.6: (a) Electrical resistivity (ρ) of the $Ti_{1+x}Fe_{2-x}Sn$ series indicates small increases in resistivity with x and generally semiconducting behavior while the (b) Seebeck coefficient is decreased for Fe–rich samples.

present in $x = 0.00$, 0.05, and 0.10. This phenomenon has been observed in low temperature measurements. [70, 71] Density of state calculations of disordered $TiFe_2Sn$ shows that the introduction of anti-site defects introduces a small number of the density of states at the Fermi level. [74] Deviations in temperature dependent resistivity behavior is similar to Heusler compound VFe_2Al,[60–62] other Heusler-dervived materials[80] and disordered metals.[81, 82]

Panel (b) of Figure 3.6 illustrates the dependence of the Seebeck coefficient with respect to temperature for the $Ti_{1+x}Fe_{2-x}Sn$ study. These results indicate that the Seebeck coefficient is reduced in Fe–rich samples and remains constant for Ti–rich samples, although the temperature of the Seebeck coefficient peak does transition to higher temperature with increasing x into Ti-rich compositions. These results are consistent with low temperature studies.[70, 71] The Seebeck coefficient is consistently positive, revealing that holes are the dominant carrier for all $TiFe_2Sn$ samples. These results separate $TiFe_2Sn$ from Heusler compound VFe_2Al, which has a Seebeck coefficient that is highly sensitive to atomic ratio: pure VFe_2Al has a maximum Seebeck coefficient near $30\,\mu VK^{-1}$, and variations in stoichiometry, such as varying the V:Al[66] or V:Fe[65] ratio, or doping the Al site with Ge[63] can enhance it to $80\,\mu VK^{-1}$ or $-120\,\mu VK^{-1}$.

Figure 3.7 illustrates the effects on thermoelectric properties resulting from the substitution of Sn for Sb in the form $TiFe_2Sn_{1-y}Sb_y$ ($y = 0.01$, 0.05). Sb is

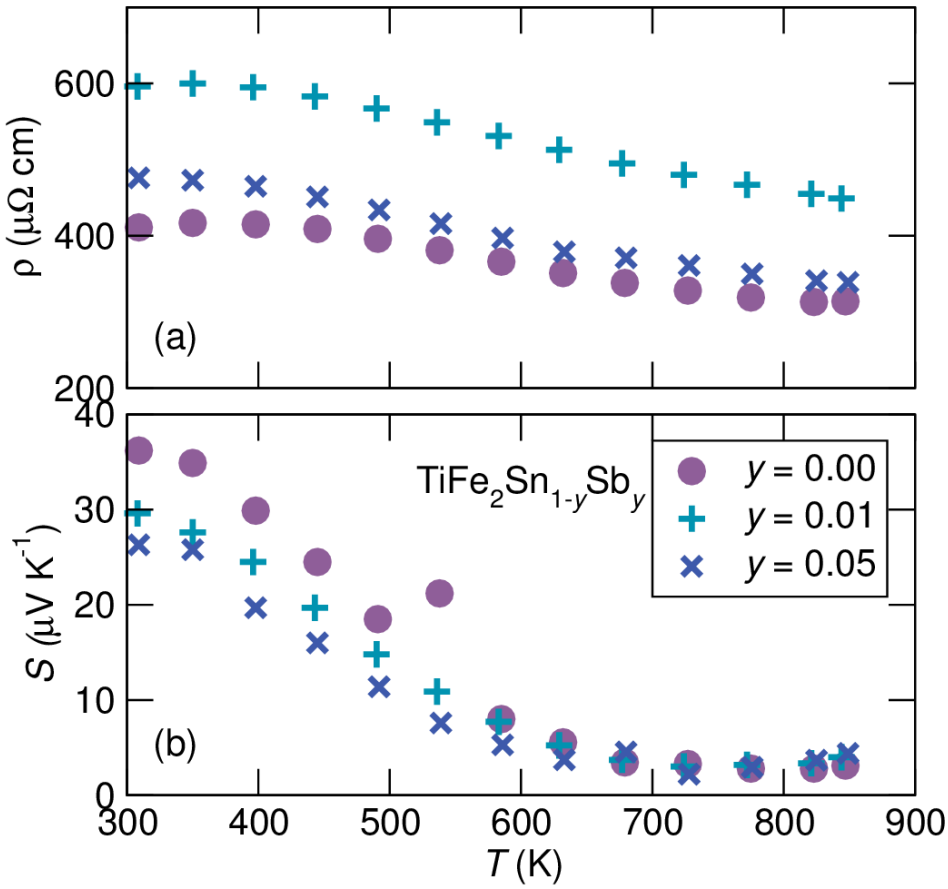

Figure 3.7: (a) Electrical resistivity of the $TiFe_2Sn_{1-y}Sb_y$ series indicates that resistivity is increased upon the introduction of Sb, while(b) the Seebeck coefficient decreases upon Sb introduction.

expected to act as an electron donor and, through the introduction of its electrons, a large Seebeck coefficient has been predicted for $TiFe_2Sn$.[59] Electrical resistivity results, displayed in panel (a), show that the $y = 0.01$ is more resistive than the stoichiometric compound, while at $y = 0.05$ resistivity returns to near that of the stoichiometric compound. However, all values remain within the same order of magnitude, suggesting no considerable impact to electrical resistivity occurs with Sb-doping. In contrast to variations in the slope of resistivity with x, the slope of resistivity remains unchanged with y. Panel (b) of Figure 3.7 illustrates that the Seebeck coefficient is reduced through the introduction of Sb, but never becomes negative, as anticipated by a Sb-type doping. Once again, these results are in contrast to VFe_2Al, which displays a reduction in electrical resistivity and Seebeck coefficient enhancement to $-120\,\mu VK^{-1}$ upon the introduction of either Si[63] or Ge.[64]

Noting that electrical resistivity is not decreased with y, as would be expected through the introduction of electron carriers in Sb-doping, the assumption that the substitution of Sb onto the Sn site introduces extra electron carriers requires modification. As highlighted in the structural section of this chapter, $TiFe_2Sn$ contains Ti–Fe anti-site defects that have been shown elsewhere[74] to shift the band structure from that of calculations that assume a fully ordered, defect free material. In the defective electronic structure, excess Sb electrons are not able

to contribute to electronic transport. Thus, Sb doping is an ineffective technique to enhancing the thermoelectric properties of disordered $TiFe_2Sn$.

3.4 Conclusions

Varients of the Heusler compound $TiFe_2Sn$ were studied through a variety of techniques including synchrotron X-ray and neutron diffraction, electron microscopy, and thermoelectric physical property measurements (Seebeck coefficient and electrical resistivity). Evaluation of a series of compounds with varied Ti–Fe ratio ($Ti_{1+x}Fe_{2-x}Sn$, $x = -0.10$, -0.05 0.00, 0.05, 0.10) concluded that the stoichiometric compound exhibits approximately 5% Ti–Fe anti-site defects and that the degree of defects is decreased by preparing the compound from a a Ti–rich composition. Studies considering Sb doping ($TiFe_2Sn_{1-y}Sb_y$, $y = 0.01$, 0.05) showed that Sb doping does not enhance the Seebeck coefficient. This result differs from calculations that predict a high Seebeck material with doping, this discrepancy is due to the observed anti-site defects.

Chapter 4

Investigation of thermoelectric performance in pseudo–binary half-Heusler alloy between TiNiSn and NbCoSn

Half-Heusler materials with 18 valence electrons are the foundation of leading Heusler-based thermoelectric materials. Previous studies considering solid solution or pseudo-binary half-Heusler alloys for thermoelectric applications maintain this 18 valence electron count by substituting elements located in

the same groups as those of the parent compounds. Herein we explore novel 18 valence electron half-Heusler alloys TiNiSn and NbCoSn in the solid solution $(TiNiSn)_{1-x}(NbCoSn)_x$. This work utilizes powder synchrotron X-ray and neutron diffraction data to reveal that these compounds form a solid solution, and investigates the high temperature thermoelectric performance of these alloys through electrical and thermal transport measurements. We find $(TiNiSn)_{0.5}(NbCoSn)_{0.5}$ to be the most promising of these alloys: While exhibiting an elevated resistivity respective to the parent compounds, it has a high Seebeck coefficient combined with reduced thermal conductivity to reach a maximum zT of 0.04 at 750 K.

4.1 Introduction

In this chapter, we present a novel approach towards half-Heusler thermoelectrics by exploring a pseudo-binary half-Heusler alloy that maintains 18 VEC for all compositions while expanding the X and Y sites to elements beyond a specific column of the periodic table. As determined in this study, TiNiSn forms a solid solution with NbCoSn that maintains an 18 VEC for all intermediate compounds. TiNiSn is an established half-Heusler thermoelectric in which the tetrahedral $(\frac{3}{4}, \frac{3}{4}, \frac{3}{4})$ vacancies can be filled by Ni interstitial atoms.[83, 84]

NbCoSn is a less known half-Heusler compound with a Seebeck coefficient similar to that of TiNiSn.[85] Previous studies indicate TiNiSn can be doped with Nb ($Ti_{1-x}Nb_xNiSn$ up to $x = 0.05$) resulting in overall zT improvement for $x = 0.02$,[86] while replacing Co for Ni ($TiNi_{1-x}Co_xSn$ up to $x = 0.10$) results in an increased resistivity.[87] Here we present the first report of a solid solution between these half-Heusler compounds. Through this work, we show that alloying increases the electrical resistivity in all samples, limiting the zT to below that of TiNiSn. However, the intermediate compound $(TiNiSn)_{0.5}(NbCoSn)_{0.5}$ has a promising Seebeck coefficient that is comparable to TiNiSn and NbCoSn, while also benefiting from a significant reduction in thermal conductivity, achieving a maximum zT of approximately 0.04 at 750 K.

4.2 Experimental details

A series of five compounds were prepared with nominal stoichiometry of $(TiNiSn)_{1-x}(NbCoSn)_x$ ($x = 0.00$, 0.25, 0.50, 0.75, 1). Compositions were selected to enable an investigation of the solubility between the half-Heusler compounds TiNiSn and NbCoSn. Samples were prepared under an Ar atmosphere utilizing a Crystalox MCGS5 levitation melting system with a water cooled copper crucible. Approximately 12 g charges were formed from a stoichiometric ra-

tio of pure elements: Nb foil (99.8%, Sigma Aldrich), Co pieces (99.5%, Sigma Aldrich), Ni foil (99.9%, Sigma Aldrich), Ti wire (99.7%, Sigma Aldrich), and Sn shot (99.8%, Sigma Aldrich). The resulting charge was cut into slices approximately 3 mm thick by a diamond saw. These slices were then wrapped in Ta foil, sealed in a silica ampoule under a partial pressure of Ar, annealed for one week at 1123 K from which the slices were cooled to room temperature over 5 hours. Bars for electrical transport properties with approximate dimensions $8 \times 3 \times 3$ mm were sectioned by diamond saw. Circular discs with a 6 mm diameter were sectioned by electrical discharge machining and thinned to 1 – 2 mm for thermal diffusivity measurements. Remaining sections were selected for electron microscopy measurements or ground by mortal and pestle for diffraction measurements.

Synchrotron X-ray diffraction (XRD) was acquired for all samples at the 11-BM beamline at the Advanced Photon Source at Argonne National Lab. Measurements were conducted at 295 K with a wavelength of 0.4593 Å to avoid Sn absorption. Neutron diffraction data was acquired for all samples at the POWGEN diffractometer at the Spallation Neutron Source located at Oak Ridge National Laboratory. 2 – 3 g of sample was loaded in vanadium cans and approximately 90 minute measurements were conducted at 300 K. TOPAS[75] was utilized for joint Rietveld refinements of diffraction data. VESTA[48] was used

to visualize the half-Heusler crystal structure.

Electron microscopy was completed by removing pieces from the bulk, mounting in epoxy, grinding with SiC paper, and then polishing with diamond suspensions down to 0.25 μm. Scanning electron microscopy (SEM) studies were completed on a FEI XL30 Siron FEG equipped with a backscattered-electron (BSE) detector operating at 15.0 kV. Energy dispersive X-ray (EDX) analysis supported phase identification, including impurity phase identification, as discussed in the structural characterization section of this chapter.

Electrical transport properties (Seebeck coefficient, S, and electrical resistivity, ρ) were measured on an ULVAC ZEM-3 instrument. Measurements were completed under 0.1 atm of He and were conducted twice. Samples were heated from 300 to 850 K and cooled to 300 K with measurements completed every 50 K such that heating and cooling measurement temperatures differed by 25 K. Data presented is collected on second cooling.

To determine thermal conductivity, κ, thermal diffusivity, h, heat capacity, c_p, and density, D, measurements were completed, where $\kappa = hc_pD$. Laser flash thermal diffusivity measurements were performed on pellets with a diameter of 6 mm and a thickness ranging from 0.95 – 2.74 mm using a Netzsch LFA 457. Pellets were coated with graphite spray three times for even distribution. The

measurements were collected from 323 K to 1123 K and back to 323 K in 50 K increments under a purging argon flow of 110 milliliters per minute using a Cowan+ pulse correction. Heat capacity measurements were performed using a Netzsch DSC 3500 and scanned from 293 K to 873 K under nitrogen with a flow rate of 40 ml per minute and a heating rate of 10 K per minute. The amount of energy required to heat the sample was then compared to a known sapphire standard to determine heat capacity using an inbuilt ratio method. Density was measured using the Archimedes method where each sample was weighed dry, then weighed after being submerged in boiling DI water for half an hour, and then weighed suspended in DI water. Density was calculated following the method described by Rahaman.[88]

4.3 Structural characterization

Diffraction analysis via joint refinement of X-ray and neutron data was completed for a series of compounds $(TiNiSn)_{1-x}(NbCoSn)_x$ ($x = 0.00$, 0.25, 0.50, 0.75, 1). Synchrotron X-ray diffraction features high Q-space resolution and signal-to-noise ratio that enables the determination of accurate lattice parameters and identification of minor impurity phases, while neutron diffraction provides elemental contrast that allows for the accurate determination of site occu-

pancies as the neutron scattering length, Coh_b, is -3.438 fm for Ti, 7.054 fm for Nb, 10.3 fm for Ni, and 2.49 fm for Co.[89] To reduce correlation between terms, all atomic displacement parameters were fixed to a B_{eq} value of 0.3 Å($U_{iso} \approx 0.0038$ Å^2) which is consistent with previous refinements.[85] It was assumed that all sites were completely occupied. A secondary TiNiSn phase was present in samples $x = 0.00, 0.25, 0.50$ and was modeled with a fixed 10% Ni interstitial on the $(\frac{3}{4}, \frac{3}{4}, \frac{3}{4})$ site. The resulting goodness-of-fit R_{wp} parameters for all refinements were in the range of 8–12%.

Figure 4.1 shows powder synchrotron X-ray diffraction data, Rietveld refinement fits, and difference curves between the experimental data and the fit. The main phase of all samples was fit with the $Fm\bar{3}m$ half-Heusler crystal structure. For $x = 0$, 0.25, and 0.50, a Ni-rich TiNiSn phase[36, 83] was added to the refinement and is highlighted in the (220) reflection shown in the right side panels of Figure 4.1 where the emergence of a shoulder on the left side of the peak can be seen. The relative phase fraction of this secondary phase to the main phase decreased with x from approximately 20 wt% in $x = 0$ to 9 wt% in $x = 0.50$. Impurity phases less than 5 wt% were identified in the analysis of the diffraction data, including, in order of increasing x: $TiNi_2Sn$, Sn_5Ti_6, Sn, Nb_3Sn, and CoNb. An additional impurity phase that could not be indexed is present in the $x = 0.25$ sample. These impurity phases were additionally confirmed through

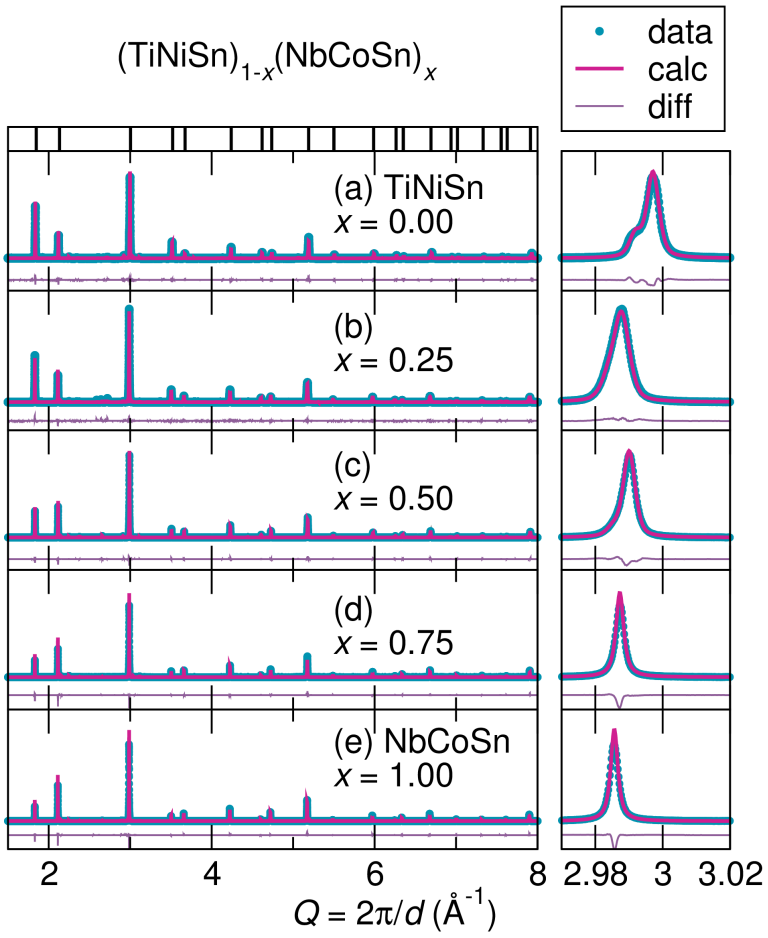

Figure 4.1: Powder synchrotron X-ray results, Rietveld refinement fits, and resulting difference curves for the complete $(TiNiSn)_{1-x}(NbCoSn)_x$ series, indicating the formation of a solid solution. Indexed peaks for a half-Heusler phase is shown in the top panel. The main (220) peak is highlighted in the right hand panel, where an increase in lattice constant with x can be visualized by a peak shift. This peak also shows the left-hand shoulder of $x = 0.00$, 0.25, and 0.50 that arises from a Ni-rich TiNiSn phase.

energy dispersive X-ray spectroscopy.

Figure 4.2 shows neutron diffraction data, Rietveld refinement fits, and difference curves between the data and fits for all samples. Due to the elemental sensitivity of neutron diffraction, fitting of this data aids in accurate site occupancy determination. By considering these fits and those shown in Figure 4.1, we confirm the existence of a solid solution between half-Heusler compounds TiNiSn and NbCoSn.

Structural parameters resulting from joint refinements are reported in Figure 4.3. Panel (a) displays site occupancy as a function of x, illustrating that the refined occupancy values follow nominal composition, indicated by the gray line. The occupancy results indicate that the Ti–Nb ratio lies near the expected composition for all x while the Ni–Co ratio favors Ni incorporation at lower x, which is consistent with the presence of an excess-Ni phase at low x compositions. It should be noted that these peaks could not be isolated in the neutron diffraction data due to lower Q-space resolution. Figure 4.3 (b) shows that the lattice constant generally follows Vegard's law behavior[79] between the two end member compositions. The unexpected lattice constant for $x = 0.25$, in combination with the larger than typical wt% of impurity phases in this sample, may suggest that the solid solution, while not completely inaccessible, may be less energetically favorable. While there are slight deviations from

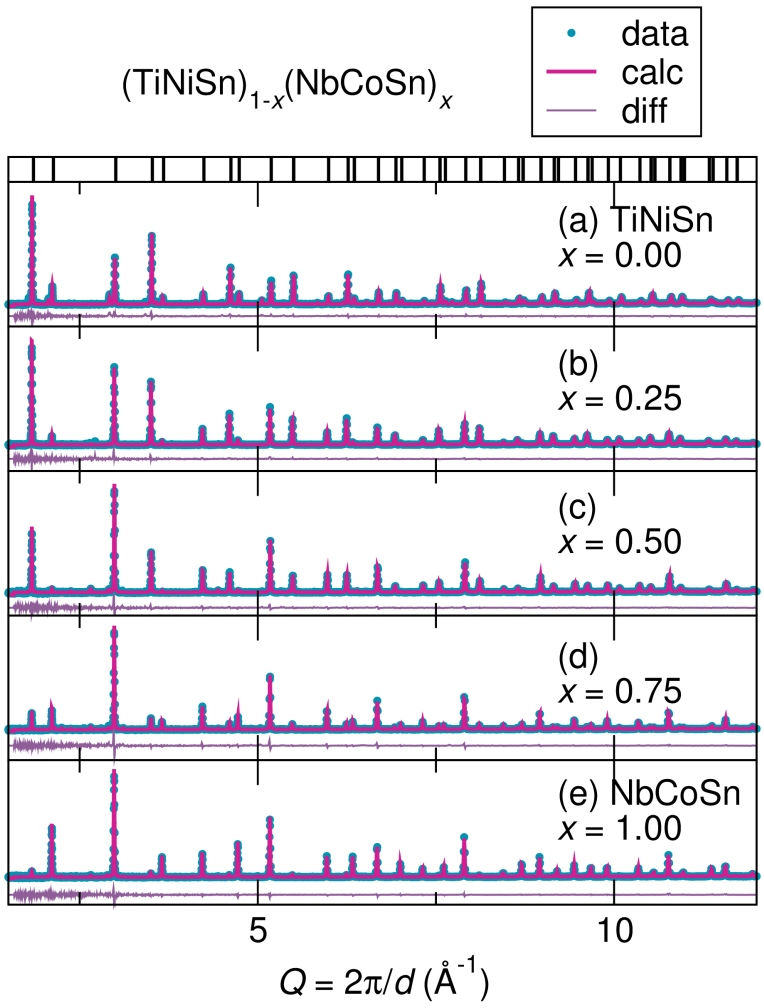

Figure 4.2: Powder neutron diffraction data, Rietveld refinement, and difference curves for the $(TiNiSn)_{1-x}(NbCoSn)_x$ series. As neutron diffraction has strong elemental sensitivity, as apparent by comparing the relative peak intensities, fits to this data aids in the accurate site occupancies.

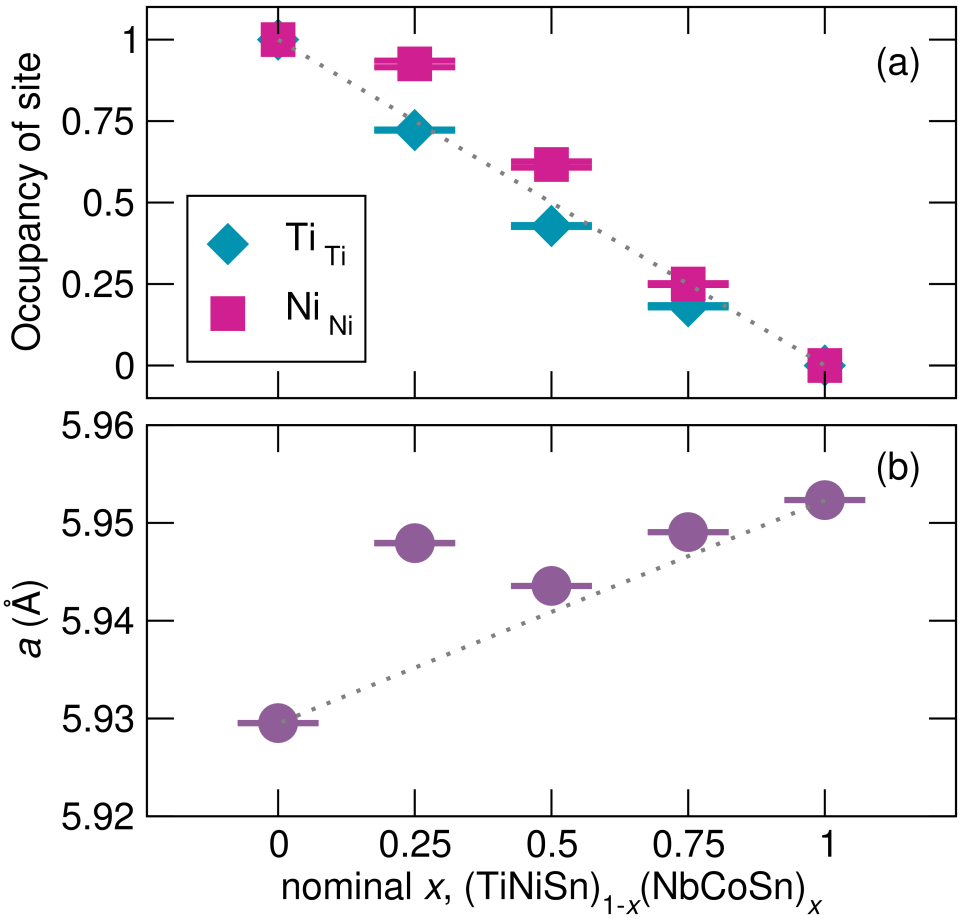

Figure 4.3: Structural parameters of the $(TiNiSn)_{1-x}(NbCoSn)_x$ series. Panel (a) illustrates the relationship between site occupancy and x. A grey trend line highlights the nominal composition, showing that site occupancies generally follow the predicted ratio. Panel (b) shows that the lattice constant of this solid solution generally follows linear Vegard's law behavior, as shown by a gray trend line.

expected trends due to the favorable formation of impurity phases, refinement of the diffraction data evidences that a solid solution exists between TiNiSn and NbCoSn.

4.4 Physical properties

To evaluate the thermoelectric performance of these alloys, high temperature physical property measurements were collected as a function of temperature. Electrical properties are shown in Figure 4.4 as a function of temperature. Values of TiNiSn[84] and NbCoSn[85] are comparable to those published elsewhere. Electrical resistivity measurements (ρ) shown in Figure 4.4 (a) indicate that all intermediate alloys are more resistive than pure compounds. This is accredited to alloy scattering introduced on the Y site, as both Ni and Co contribute to the conductive zinc-blende sublattice and the mixing of these elements results in alloy scattering. These results are similar to those observed by Romaka *et. al.*, who observed an increase in resistivity with Co-doped TiNiSn.[87] TiNiSn-rich compositions ($x = 0.00$, 0.25, 0.50) exhibit a negative slope of ρ with temperature, indicating semiconducting behavior, while NbCoSn-rich samples have a positive slope, indicating metallic behavior. The semiconducting behavior of the Ti-rich compositions can be explained by the secondary TiNiSn phase with ex-

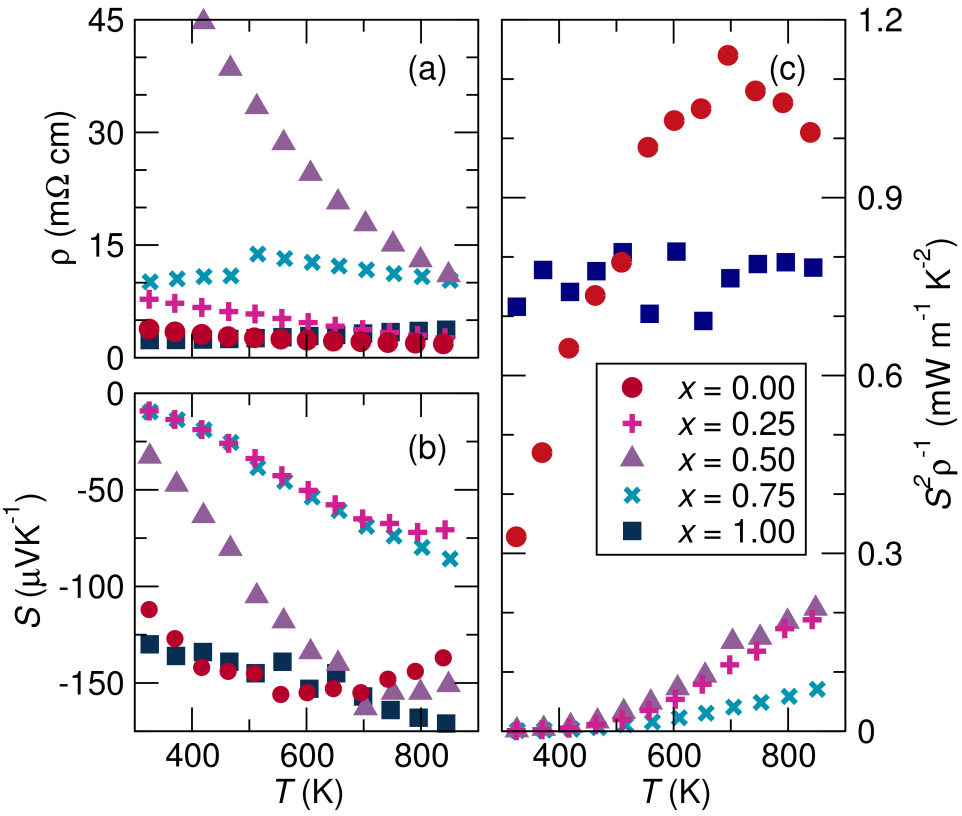

Figure 4.4: Electronic properties of $(TiNiSn)_{1-x}(NbCoSn)_x$ with respect to temperature. (a) Electrical resistivity of intermediate compounds is larger than that of end member compounds. (b) The magnitude of the Seebeck coefficient is largest for end member compositions while $x = 0.50$ attains a similar magnitude at higher temperatures. (c) Thermoelectric powerfactor ($S^2\rho^{-1}$), relating electronic properties to thermoelectric performance, indicates that potential of intermediate compounds is limited by high resistivity or low magnitude of Seebeck coefficient.

cess Ni, which is known to impact electrical conduction by modifying the density of states.[37]

The Seebeck coefficient (S), shown in Figure 4.4 (b), indicates that, with the exception of high temperature $x = 0.50$, the magnitude of the Seebeck coefficient is greatly reduced compared to pure compounds. The extreme temperature dependence of $x = 0.50$ is unique: At low temperatures it has both an increased resistivity and a reduced Seebeck coefficient, while at higher temperatures attains values that rival those of end member compounds. This suggests that at higher temperatures electron transport differs from that of lower temperatures, possibly by a scattering mechanism that is overcome at higher temperatures, enabling superior thermoelectric performance.

Figure 4.4 (c) illustrates the thermoelectric powerfactor ($S\rho^{-1}$) as a function of temperature. As both electrical resistivity and Seebeck coefficient are dependent on carrier concentration, it is expected that the electrical resistivity would be proportional to the magnitude of the Seebeck coefficient.[2] However, this trend is not observed for these alloys, suggesting that the electronic transport of intermediate compositions does not reflect that of end member compounds. This is best explained by considering the alloying of the Y site between Ni and Co. Doping this site impacts the electronic structure of half-Heusler compounds, since these rely on the zinc-blende sublattice for electronic transport. Results

for the the $x = 0.50$ sample suggest that when the Ni to Co ratio becomes 1:1, this alloy scattering can be overcome at high temperatures.

Figure 4.5 (a) presents the thermal conductivity (κ) of these alloys with respect to temperature. End member compounds have thermal conductivity values near 5 $Wm^{-1}K^{-1}$, which is reduced to 3 $Wm^{-1}K^{-1}$ for the intermediate compound $x = 0.50$. This 40% reduction in thermal conductivity is larger than the reduction observed for the introduction of a secondary phase[84, 85] (approx. 10%) and is similar to those observed in MNiSn alloys.[19] This enhanced reduction results from phonon scattering on point defects located on both the X and Y sites of the lattice.

The zT, shown in Figure 4.5 as calculated by $zT = [S^2/(\kappa\rho)]T$, indicates that end member compounds TiNiSn and NbCoSn have superior thermoelectric performance to any alloy that can be formed between them. Intermediate compound $x = 0.50$ is the most promising sample due to the large magnitude of its Seebeck coefficient and low thermal conductivity, but it is hampered by an increased electrical resistivity compared to the parent compounds. Thus, we can see that despite the successful reduction of thermal conductivity and maintenance of high temperature Seebeck coefficients, the consequences of alloying on electrical resistivity outweighs these benefits, and must be taken into consideration for the design of thermoelectric materials through compositional

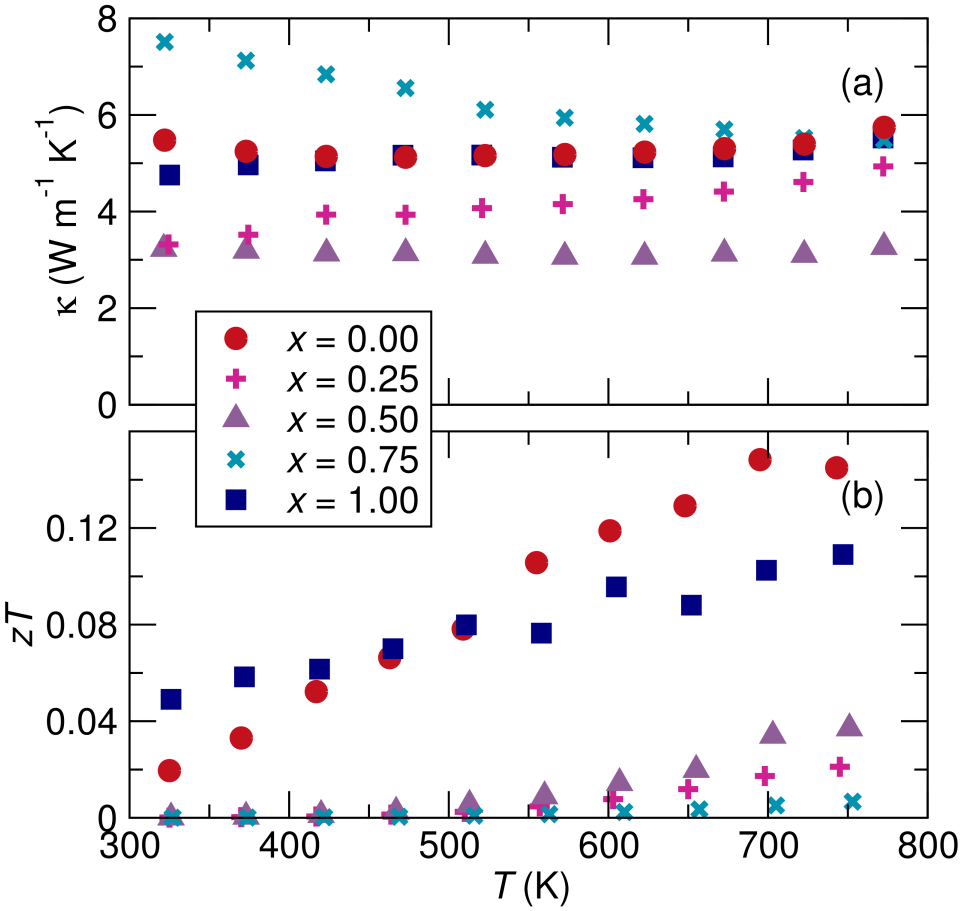

Figure 4.5: Thermal conductivity and zT calculations for $(\mathrm{TiNiSn})_{1-x}(\mathrm{NbCoSn})_x$ alloys as a function of temperature. (a) Thermal conductivity is reduced for for the $x = 0.25$ and 0.50 intermediate compositions as compared to pure compounds. (b) The thermoelectric figure of merit remains the largest for pure compounds. The intermediate $x = 0.50$ composition has the next largest zT due to its high Seebeck coefficient and reduced thermal conductivity, however the high resistivity of this composition prevents zT enhancement.

alloying.

4.5 Conclusions

Through this work we show that a solid solution exists between half-Heusler compounds NbCoSn and TiNiSn that maintains a constant VEC of 18. This psuedo-binary alloy was confirmed by powder X-ray synchrotron and neutron diffraction analysis. We show that while $(TiNiSn)_{0.5}(NbCoSn)_{0.5}$ has a relatively high resistivity, it also has a promising Seebeck coefficient and a large reduction in thermal conductivity that yields the largest zT of the intermediate compounds. We show that the introduction of point defects into a half-Heusler compound reduces thermal conductivity, but that this Y site doping ultimately introduces alloy scattering that negatively impacts the electrical resistivity.

Chapter 5

Phase separation and thermoelectric properties with heat treatment in half-Heusler TiNiSn

5.1 Introduction

TiNiSn is a well studied half-Heusler compound for thermoelectric applications.[25] Ni-interstitials can reside in the tetrahedral voids of the half-Heusler crystal structure,[36] and impact the electronic band structure and density of states of TiNiSn.[37, 90] Furthermore, by acting as point defect scatter-

ing centers, these interstitials reduce thermal conductivity, improving zT. An experimentally determined phase diagram between TiNiSn–$TiNi_2Sn$ identified that these phases have some solubility at high temperature enabled by excess Ni occupying Ni-interstitials. At a composition of $TiNi_{1.1}Sn$, regions of phase separation and phase solubility can both be accessed.[91]

This chapter examines the role that Ni-interstitials have on the thermoelectric physical properties of TiNiSn. A series of heat treatments were conducted for $TiNi_{1.1}Sn$ according to the phase diagram by Verma *et al.*[91] Levitation melted material was first homogenized for 6 days to phase separate TiNiSn from $TiNi_2Sn$, followed by a high temperature quench in the regime of the solid solution, which was followed by a low temperature anneal, again enabling phase separation. Samples were removed at key points in the heat treatment for characterization: relative phase fractions of TiNiSn–$TiNi_2Sn$, presence of Ni-interstitials, microstructure, and room temperature physical property measurements.

This chapter shows that, as consistent with the phase diagram, high temperature quenching results in a material with less $TiNi_2Sn$ and more Ni-interstitials. These interstitials are associated with an enhanced Seebeck coefficient, a reduced thermal conductivity, and an improved zT. Additional low temperature annealing following the high temperature quench allows the $TiNi_2Sn$ phase

to reemerge and thermoelectric properties to approach those of the original homogenized compound. By contributing our understanding on the relationship between Ni-interstitials and thermoelectric performance of TiNiSn, this work enables both the understanding of fundamental concepts behind defect-engineering and the development of high performance thermoelectric materials.

5.2 Experimental details

Four $TiNi_{1.1}Sn$ samples were melted utilizing a Crystalox MCGS5 levitation melting system with a water cooled copper crucible under an Ar atmosphere. Charges were formed from a stoichiometric ratio of $TiNi_{1.1}Sn$ from elemental sources: Ti wire (99.7%, Sigma Aldrich), Ni foil (99.9%, Sigma Aldrich), and Sn shot (99.8%, Sigma Aldrich). As visualized in Figure 5.1, heat treatments were applied to each sample. The *Homogenized* (*H*) sample was held at 1173 K for 6 days, after which the sample was air-quenched. The *Homogenized-Quenched* (*HQ*) sample was homogenized with *H* and was subsequently brought to 1423 K for 6 hours from which it was air-quenched. The *Homogenized-Quenched-Annealed-8hour* (*HQA8*) sample was heat treated with *H* and *HQ* and then annealed for 8 hours at 623 K. Similarly, *Homogenized-Quenched-Annealed-32hour* (*HQA32*) was heat-treated with the other samples, but was then an-

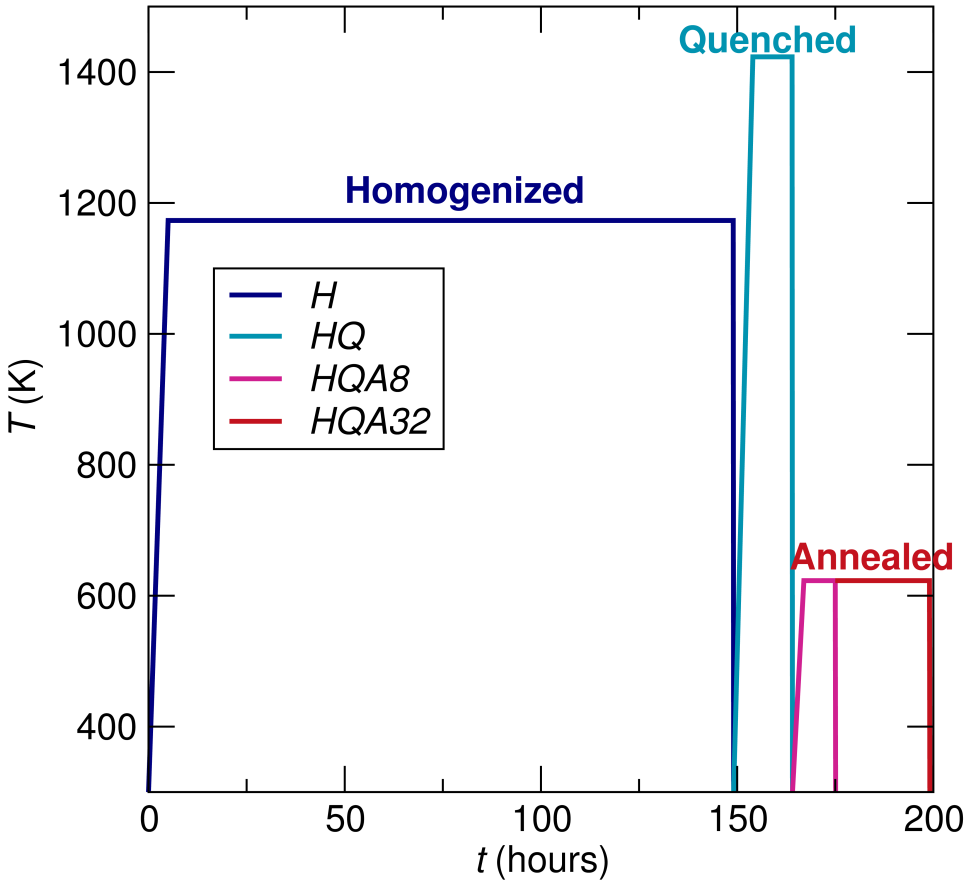

Figure 5.1: Plot of temperature (T) against time (t) to visualize the heat treatments applied in this study. Four samples were prepared: *H*, *HQ*, *HQA8*, and *HQA32*. With the exception of the final anneals for *HQA8* and *HQA32*, heat treatments were applied to samples simultaneously.

nealed for 32 hours at 623 K. All heat treatments were conducted by wrapping the samples in Ta foil and sealing in a silica ampoule under vacuum. Samples were sectioned by diamond saw for experiments, including a piece to grind into powder for synchrotron X-ray diffraction, a piece for scanning electron microscopy, and a bar for physical property measurements, approximately $8 \times 3 \times 3$ mm.

Synchrotron X-ray diffraction (XRD) was conducted at the 11-BM beamline at the Advanced Photon Source at Argonne National Lab. Measurements were conducted at 295 K and ran at a modified wavelength (≈ 0.45 Å) to reduce Sn absorbance. A Rietveld refinement analysis was completed on diffraction data utilizing Topas.[75]

The microstructure of *H*, *HQ*, and *HQA32* was examined by mounting a piece from the bulk samples into epoxy. The resulting pucks were polished with diamond suspension down to 0.25 μm. Studies were conducted on a FEI XL30 Siron FEG scanning electron microscope (SEM) equipped with a backscattered-electron (BSE) detector and energy dispersive X-ray (EDX) spectrometer, enabling phase observation and determination.

Electrical transport properties (Seebeck coefficient and electrical resistivity) were evaluated on an ULVAC ZEM-3 instrument under a partial Ar atomso-

phere. Measurements were conducted at 310 K. Thermal conductivity measurements were conducted on a Quantum Design Physical Property Measurement System (PPMS) utilizing the Thermal Transport Option (TTO). Measurements were taken between 300 K–310 K.

5.3 Results and discussion

Structural characterization

The evaluation of synchrotron X-ray diffraction data by Rietveld refinement, through its high signal-to-noise ratio, enables a precise analysis of the half-Heusler to Heusler phase fraction ratio. Furthermore, the Q-space resolution of this technique aids the evaluation of accurate lattice parameters and observations of the asymmetric TiNiSn peak shape resulting from Ni-interstitials. A representative fit of the XRD pattern for *H* is shown in Figure 5.2 (a), wherein both the TiNiSn and $TiNi_2Sn$ phases can be identified. By fitting both these phases for all samples, the evolution of the $TiNi_2Sn$ phase fraction with heat treatment is shown in Figure 5.2 (b). This figure illustrates that quenching $TiNi_{1.1}Sn$ from high temperature greatly reduces the phase fraction of $TiNi_2Sn$, as shown in the reduction of phase fraction from sample *H* to sample *HQ*. This results from

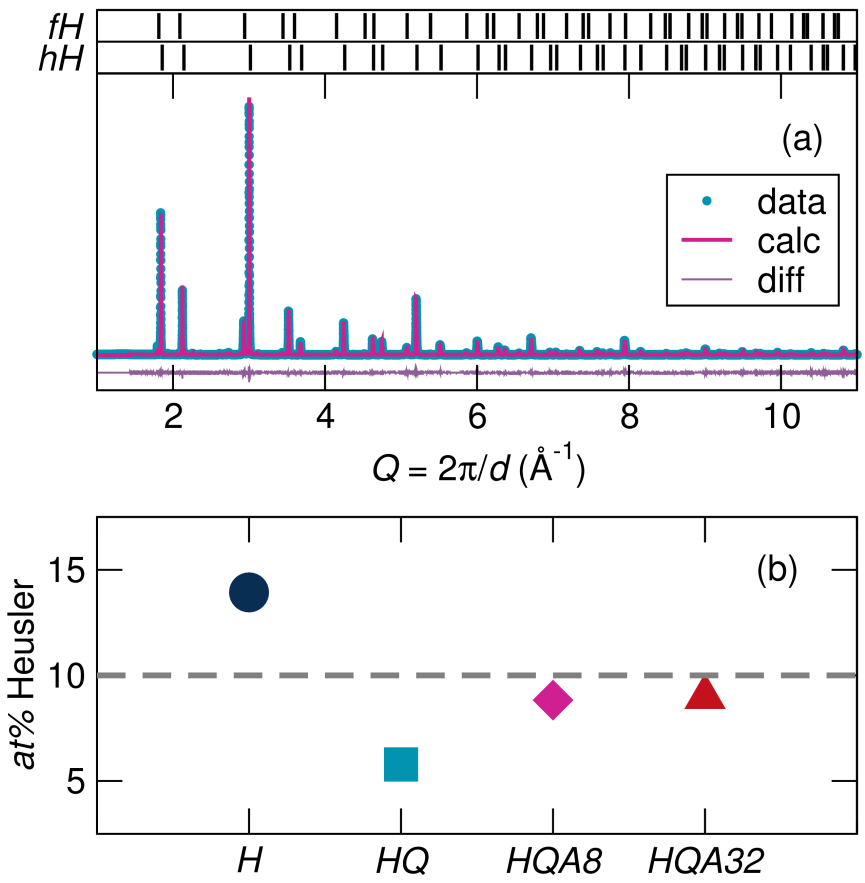

Figure 5.2: (a) Fit and X-ray diffraction data for sample *H*, representing diffraction studies. All samples contain both half-Heusler TiNiSn (*hH*) and full-Heusler $TiNi_2Sn$ (*fH*). The peaks of these phases are indexed in the top panels. (b) Plot indicating variations in at% $TiNi_2Sn$ (as compared to TiNiSn) with heat treatment, the dashed line indicates 10 at%, the expected amount of $TiNi_2Sn$ in fully phase separated $TiNi_{1.1}Sn$. HQ has reduced $TiNi_2Sn$ content due to its high temperature quench from the solid solution regime. The $TiNi_2Sn$ phase reforms with low temperature annealing, as shown by *HQA8* and *HQA32*.

solubility between the two phases at this temperature that enables the formation of Ni-interstitials in the TiNiSn phase, depleting Ni from the $TiNi_2Sn$ phase. As these samples are annealed (*HQA8* and *HQA32*) the $TiNi_2Sn$ phase reforms, approaching that of the nominal 10%.

Further assessment of Ni-rich TiNiSn can be conducted by evaluating Figure 5.3, which considers the evolution of the main (220) peak with heat treatment. From this analysis, a broadening in the main peak resulting from Ni-interstitials becomes evident with further heat treatment. In panel (a) of Figure 5.3 the (220) peak of sample *H* was fit by two TiNiSn phases, one with excess Ni-interstitials. However, successful fitting of sample *HQA8*, shown in frame (b), required the addition of a third phase to the Rietveld refinement in order to accurately represent the long shoulder on the right side of the peak. Lattice constant evaluation indicates expansion in sample *HQA8* compared to *H*, further evidence of Ni-interstitials as these expand the TiNiSn lattice constant.

Microscopy

To evaluate the evolution of microstructure with heat treatment, a series of micrographs were collected by SEM using a back-scattered electron detector in order to show Z-contrast, as shown in Figure 5.4. EDS was used to estab-

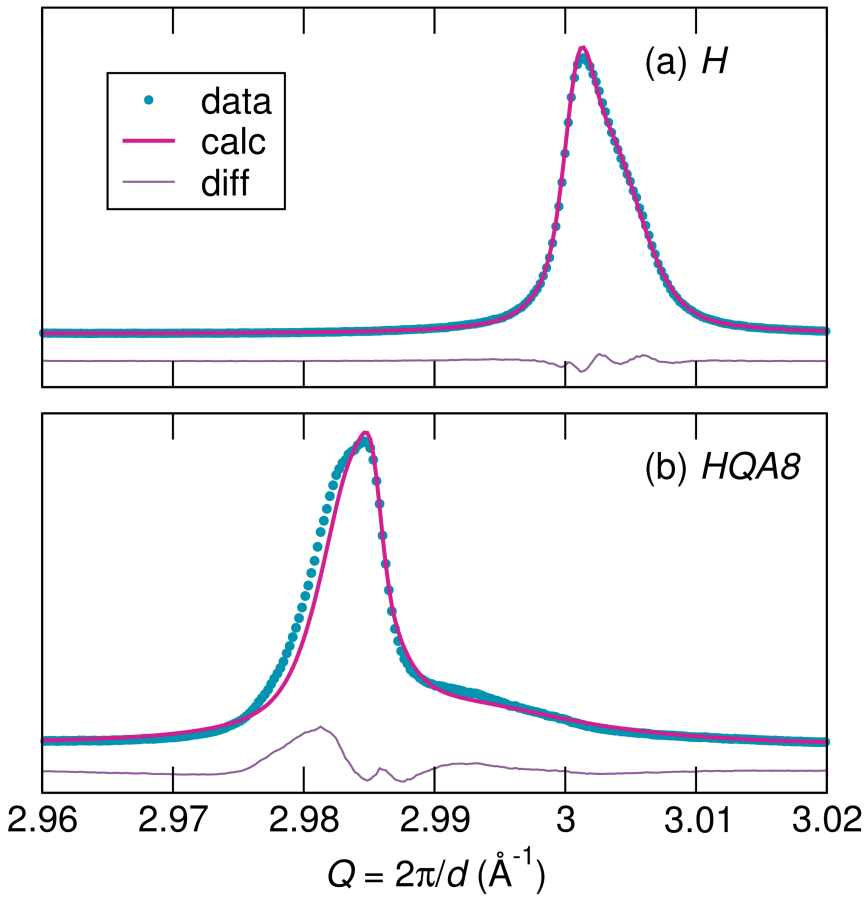

Figure 5.3: The main (220) peak of half-Heusler TiNiSn is highlighted for (a) sample *H* and (b) sample *HQA8* with diffraction data, Rietveld refinements, and difference curves shown. These plots illustrate the complex shape of the half-Heusler peaks that results from multiple TiNiSn variants with lattice constants that depend on the presence of Ni-interstitials. *HQA8* exhibits a larger lattice constant and a more complex shape. These observations result from the presence of more Ni-interstitials in the TiNiSn phase.

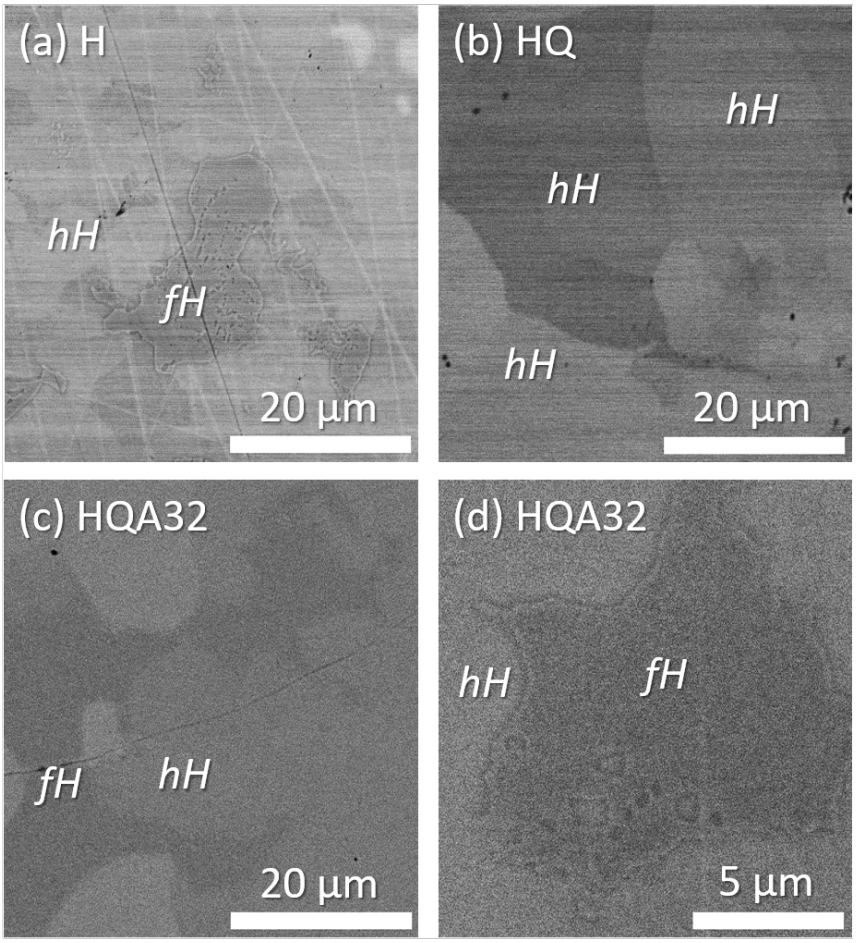

Figure 5.4: Scanning electron microscopy utilizing a back-scattered electron detector to image the microstructure of samples (a) *H*, (b) *HQ*, and (c),(d) *HQA32*, enabling analysis of microstructure evolution. Panel (a) illustrates that the homogenized sample contains separate TiNiSn (*hH*) and $TiNi_2Sn$ (*fH*) regions. (b) A high temperature quench removes the Heusler phase, resulting in homogeneous half-Heusler that, according to EDS, contains excess Ni. In (c), low temperature annealing reintroduces the Heusler phase, as detailed in (d).

lish chemical compositions and to distringuish between regions of Heusler, half-Heusler, and half-Heusler with excess-Ni. Frame (a) is from sample *H* and shows phase separation between the half-Heusler and Heusler phases. The quenched sample, *HQ*, is shown in Frame (b). While XRD indicated the presence of some Heusler phase in sample *HQ*, microscopy only identified the half-Heusler phase with Ni excess. Upon low temperature annealing, sample *HQA32* in frame (c), the Heusler phase reforms and, as highlighted in frame (d), the microstructure is complex and features regions of half-Heusler within Heusler precipitates.

Physical properties

Figure 5.5 presents the room temperature physical property results for all samples studied. The Seebeck coefficient, shown in Figure 5.5 (a), is enhanced for the high temperature quenched sample, *HQ*. This enhancement fades with low temperature annealing, as indicated by the trend line towards *HQA8* and *HQA32*. By 32 hours of low temperature annealing, the Seebeck coefficient has almost returned to the value of sample *H*. This observation can be explained by considering Ni-interstitials in relation to Seebeck coefficient enhancement. Calculations indicate that these interstitials modify the density of states, impacting the Seebeck coefficient.[37, 90] This interpretation follows the results presented

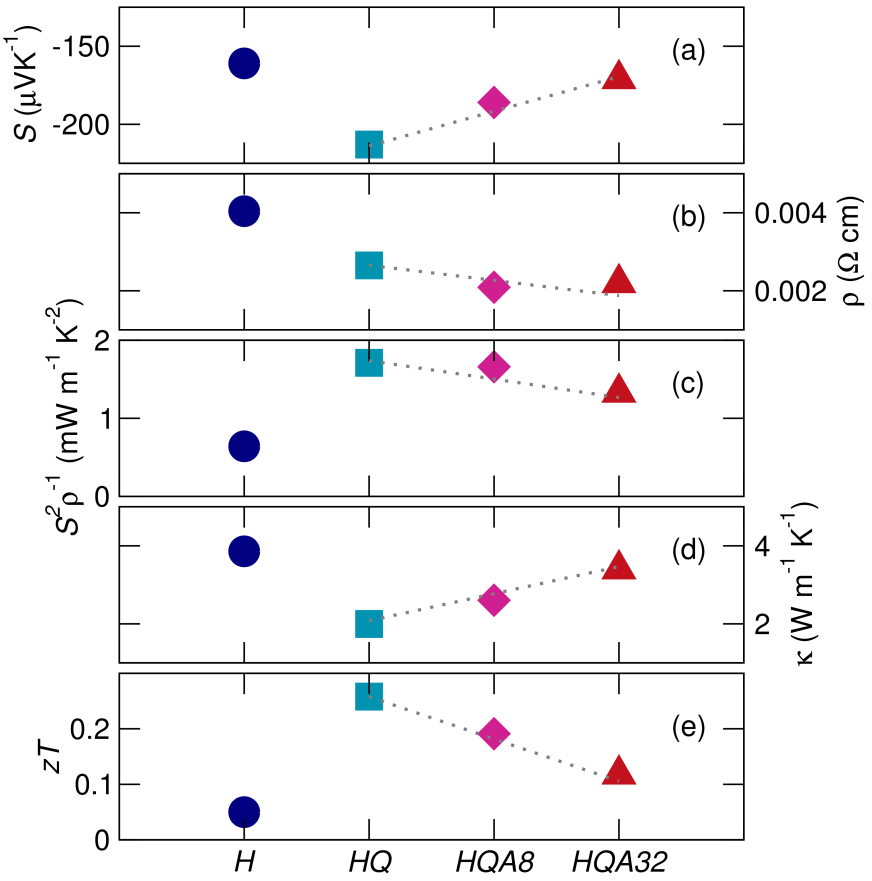

Figure 5.5: Thermoelectric property results for heat-treated samples with treatment identified on the x-axis. (a) The Seebeck coefficient is greatly enhanced for sample *HQ* and reduces with subsequent low temperature annealing. (b) Resistivity subtly decreases for *HQ* and limited change with annealing observed. As the (c) powerfactor is enhanced while (d) thermal conductivity is reduced, *HQ* has an improved figure of merit, (e) zT that is reduced with low temperature annealing, as shown in samples *HQA8* and *HQA32*.

in the structural and microstructure sections of this chapter, as they describe an increase in Ni-interstitials for the quenched sample and the formation of $TiNi_2Sn$ with low temperature annealing.

Electrical resistivity is shown in panel (b) of Figure 5.5, showing that resistivity is reduced for all samples after the high temperature quench. This is possibly the result of the Ni-vacancies in sample *H* that form in response to the greater than nominal at% of $TiNi_2Sn$ in this sample. These vacancies limit the electrical conductivity by reducing the connectivity of the $Y - Z$ zinc-blende sublattice. As the high temperature quench removes the $TiNi_2Sn$ phase, these vacancies are filled. Subsequent low temperature annealing, while allowing $TiNi_2Sn$ to reform, does not encourage vacancies to reform, enabling the reduced electrical resistivity for subsequent samples.

The electrical properties of these samples are summarized by the thermoelectric powerfactor in panel (c) of Figure 5.5. Due to its enhanced Seebeck coefficient, the high temperature quenched sample (*HQ*) has the largest powerfactor. Subsequent annealing decreases the powerfactor.

Panel (d) of Figure 5.5 shows thermal conductivity, displaying a trend that, similar to that of the Seebeck coefficient, is guided by the role of the Ni-interstitials. As the Ni-interstitials are introduced, they act as point defect

phonon scattering centers that impact the lattice contribution to thermal conductivity, reducing the overall thermal conductivity. Subsequent low temperature annealing, and the formation of $TiNi_2Sn$, returns the thermal conductivity to a value near that of the homogenized sample.

The zT of these materials has been calculated, as shown in panel (e) of Figure 5.5. Due to the impact of Ni-interstitials on both the Seebeck coefficient and the thermal conductivity, the quenched sample (*HQ*) has the largest zT. Further annealing of these samples enables the $TiNi_2Sn$ phase to reform and zT approaches that of the homogenized sample.

5.4 Conclusions

In this chapter, we discussed an annealing study that utilized four $TiNi_{1.1}Sn$ specimens with specific heat treatments. The first sample was homogenized in the biphasic regime, the next was subsequently quenched from high temperature in the solid solution regime between TiNiSn and $TiNi_2Sn$, and final samples were exposed to low temperature anneals in the biphasic regime for different time scales. We showed that, when quenched from the solid solution regime, excess Ni was present in the TiNiSn tetrahedral vacancies. These observations were related to thermoelectric physical properties, showing that the

Ni-interstitials enhance the Seebeck coefficient, while simultaneously reducing thermal conductivity, resulting in zT improvement. Subsequent annealing reduces the Ni-interstitials and reforms $TiNi_2Sn$, returning thermoelectric physical properties to that of the homogenized sample.

Chapter 6

Summary and future directions

6.1 Summary

The thermoelectric properties of three Heusler variants (NbCoSn, $TiFe_2Sn$, and TiNiSn) were examined in four distinct studies. Each of these studies found relationships between disorder and thermoelectric performance.

- **NbCoSn:** Half-Heusler NbCoSn completely phase separates from Heusler $NbCo_2Sn$. By preparing samples with and without an annealing step, we first conclude that annealing reduces the degree of Nb–Co antisite defects in NbCoSn and then realize these defects reduce thermal conductivity. A peak zT is attained for unannealed $NbCo_{1.15}Sn$.

- **$TiFe_2Sn$:** $TiFe_2Sn$ forms with Ti–Fe antisite defects. By preparing samples from a Ti-rich stoichiometry, antisite defects can be reduced. $TiNi_2Sn$ is natively a $p-$type material. When incorporating Sb, the substitutional atoms reside on the Sn site. The addition of Sb contributes electrons to the system, decreasing the Seebeck coefficient. Doping did not result in an $n-$type material, a result accredited to the Ti–Fe antisite defects.

- **$(TiNiSn)_{1-x}(NbCoSn)_x$:** A solid solution forms between 18 VEC half-Heusler compounds TiNiSn and NbCoSn. The resulting substitutional defects reduce the thermal conductivity of these alloys. Ni-interstitial atoms are present for a range of compositions, from $x = 0.00$ to 0.50 and are additional phonon scattering centers. Intermediate alloy $(TiNiSn)_{0.5}(NbCoSn)_{0.5}$ has a Seebeck coefficient similar to that of end member compounds.

- **TiNiSn:** Quenching Ni-rich TiNiSn from high temperatures preserves excess Ni as tetrahedral interstitials that form in result of high temperature solubility between TiNiSn and $TiNi_2Sn$. These Ni-interstitials enhance the Seebeck coefficient and decrease thermal conductivity. Upon low temperature annealing, interstitials diffuse to form $TiNi_2Sn$ and physical properties return to values similar to those from before the high temperature quench.

In Table 6.1, we summarize these results by calculating the fractional change in thermoelectric properties with the addition of each type of defect. By comparing these results, we see that most defects have a negative impact on electrical properties and a positive impact on thermal transport. This suggests that while defects can improve the thermoelectric performance, simultaneous enhancement of all properties can be elusive. However, the interstitial defects of TiNiSn are unique. These defects simultaneously improve the electrical and thermal properties of TiNiSn. This result can guide the development of future half-Heusler thermoelectric materials.

6.2 Future directions

Based on the work completed in this document and summarized above, we propose further studies into Heusler variants for thermoelectric applications:

- **VFe$_{1+x}$Sb:** VFeSb was revealed as an understudied but promising 18 VEC thermoelectric material in the data mining results shown in Figure 1.4. This compound has a large Seebeck coefficient ($> |200|\,\mu$VK^{-1}) but also a large thermal conductivity ($> 7\,$Wm^{-1}K^{-1}).[92] While there is no literature regarding the existence of a Heusler compound, it is compelling to consider where excess Fe would be incorporated by VFeSb. Excess Fe

Table 6.1: Summary of impact that defects have on thermoelectric properties of studied compounds, calculated as a fractional change as compared to the defect free material. From this, we conclude that the interstitial defects present in TiNiSn enable the best improvements of zT.

Legend: AM (arc melted); SPS (spark plasma sintered); LM (levitation melted); RT (room temperate)

compound	defect	preparation	temperature	$\frac{\Delta\rho}{\rho_{defectfree}}$	$\frac{\Delta S}{S_{defectfree}}$	$\frac{\Delta\kappa}{\kappa_{defectfree}}$	$\frac{\Delta zT}{zT_{defectfree}}$
NbCoSn	phase separation	AM and SPS	RT	-0.538	-0.194	0.029	0.469
			850 K	-0.461	-0.239	-0.166	0.268
NbCoSn	antisite	AM, anneal, SPS	RT	-0.586	-0.482	-0.174	0.23
			850 K	-0.566	-0.301	-0.048	0.195
solid solution	substitutional	LM and anneal	RT	14.2	-0.433	-0.410	-0.996
			750 K	6.43	0.047	-0.431	-0.66
TiNiSn	interstitial	LM and anneal	RT	-0.344	0.323	-0.483	4.17

may result either in a secondary phase or tetrahedral interstitials. Either outcome would reduce thermal conductivity.

- **(TiNiSn$_{1-y}$Sb$_y$)$_{0.5}$(NbCoSn$_{1-y}$Sb$_y$)$_{0.5}$:** The 1:1 ratio of NbCoSn to TiNiSn of Chapter 4 has a large Seebeck coefficient and a reduced thermal conductivity. The high electrical resistivity at this composition could be overcome through the addition of electron charge carriers in the form of Sb doping.

- **TiNi$_{1.1}$Sn:** The addition of a detailed microstructural study to the work in Chapter 5 would enhance understanding of the reformation of TiNi$_2$Sn with low temperature annealing.

- **MPd$_{1+x}$Sn and MPt$_{1+x}$Sn (M = Hf, Zr):** Table 6.1 shows that interstitial defects have the largest impact on the thermoelectric performance of half-Heusler compounds. MPdSn and MPtSn form from the same columns of the periodic table as TiNiSn. Only theoretical work has been conducted for MPdSn and, while MPtSn has been characterized,[93] the impact of excess Pt has not been explored.

6.3 Conclusions

In this thesis, four vignettes compose a story relating varied forms of disorder (such as phase boundaries, substitutional atoms, antisite defects, and interstitial atoms) to the thermoelectric performance of Heusler and half-Heusler materials. In some systems (TiNiSn and NbCoSn) we show that these defects can be a powerful engineering tool to enhance performance, but in others ($TiFe_2Sn$) these defects restrict the electrical performance required in thermoelectric applications. As there are more than a thousand Heusler variant compounds and numerous types of defects with diverse influence on thermoelectric performance, each Heusler system is unique. By studying the defects present in any Heusler variant material, it becomes possible to discover the engineering potential and constraints that enable the development of the thermoelectric materials of the future.

Appendix A

Comparing sample preparations of NbCoSn

While completing this research, half-Heusler NbCoSn was prepared by different techniques. In this appendix, we look to compare the thermoelectric performance of these different approaches. As detailed in Chapter 3, NbCoSn was prepared by arc melting, annealing, grinding, and then spark plasma sintering (SPS). In Chapter 5 NbCoSn was prepared as induction melting and annealing. By contrasting the thermoelectric properties of these different techniques, we show that thermoelectric performance is higher for the induction melted preparation due to a reduction in thermal conductivity.

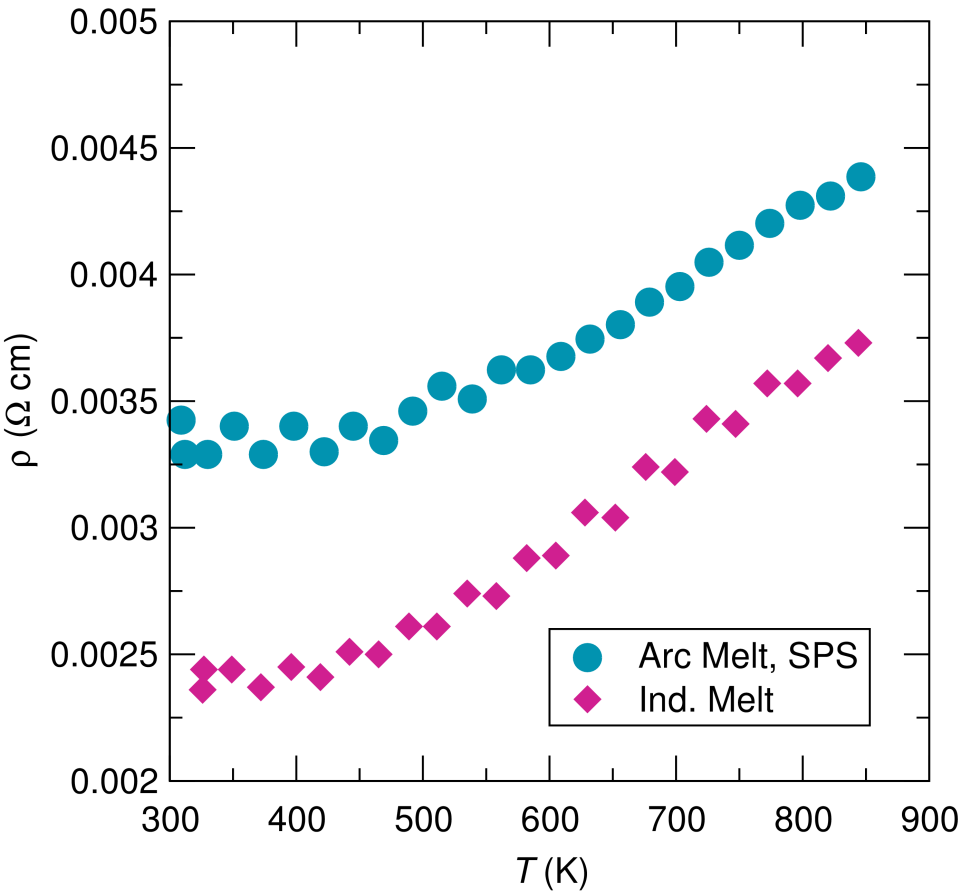

Figure A.1: Resistivity does not have a large dependence on sample preparation, indicated by values in the same order of magnitude and identical temperature dependencies. Temperature dependency suggests metallic behavior, despite band structure calculations shown in Figure 2.1 indicating a band gap.

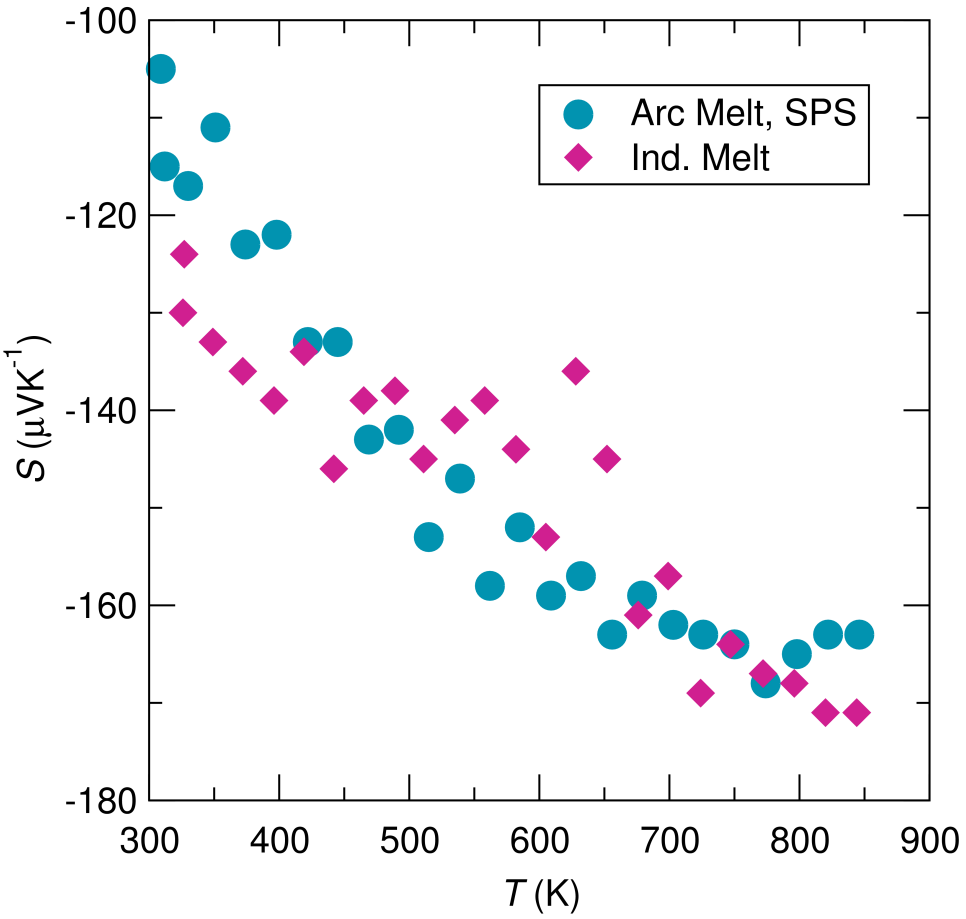

Figure A.2: The Seebeck coefficient is not significantly impacted by preparation.

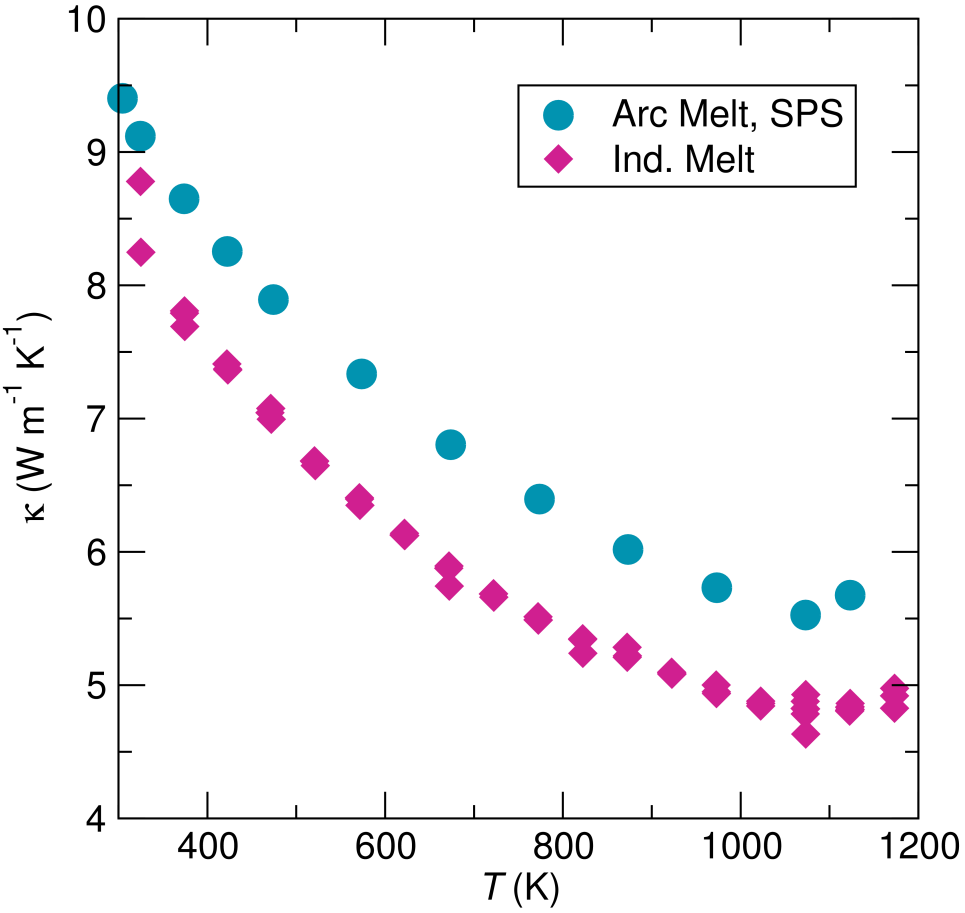

Figure A.3: Thermal conductivity is consistently lower for the induction melted sample. This result is counter intuitive as literature would suggest that sintering a powder introduces more grain boundaries to act as phonon scattering centers.

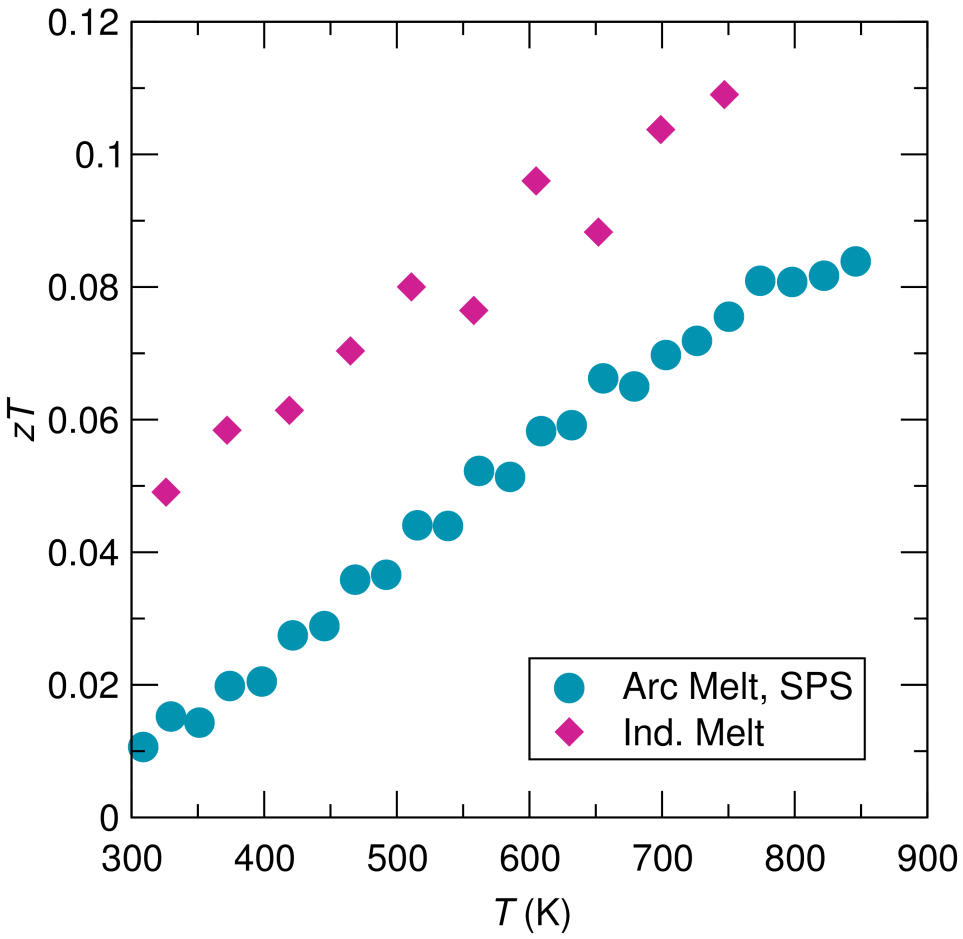

Figure A.4: The induction melted sample has a larger zT than the arc melt and SPS'ed analogue. This arises from a decrease thermal conductivity.

Appendix B

Price curves

Price curves are developed from fundamental principals to relate carrier concentration to Seebeck coefficient and electrical conductivity.[94] These plots compare electrical conductivity (on a log scale) to the Seebeck coefficient with a theoretical slope of $\frac{k_b}{q}$ for n-type materials. In the following figures, we show Price curves for $NbCo_{1+x}Sn$ (Chapter 2) and $(TiNiSn)_{1-x}(NbCoSn)_x$ (Chapter 4). All samples in these plots are represented at three different temperatures (400, 600, and 800 K). Price curve behavior qualitatively indicates semiconductor temperature-dependence of charge carrier concentration.

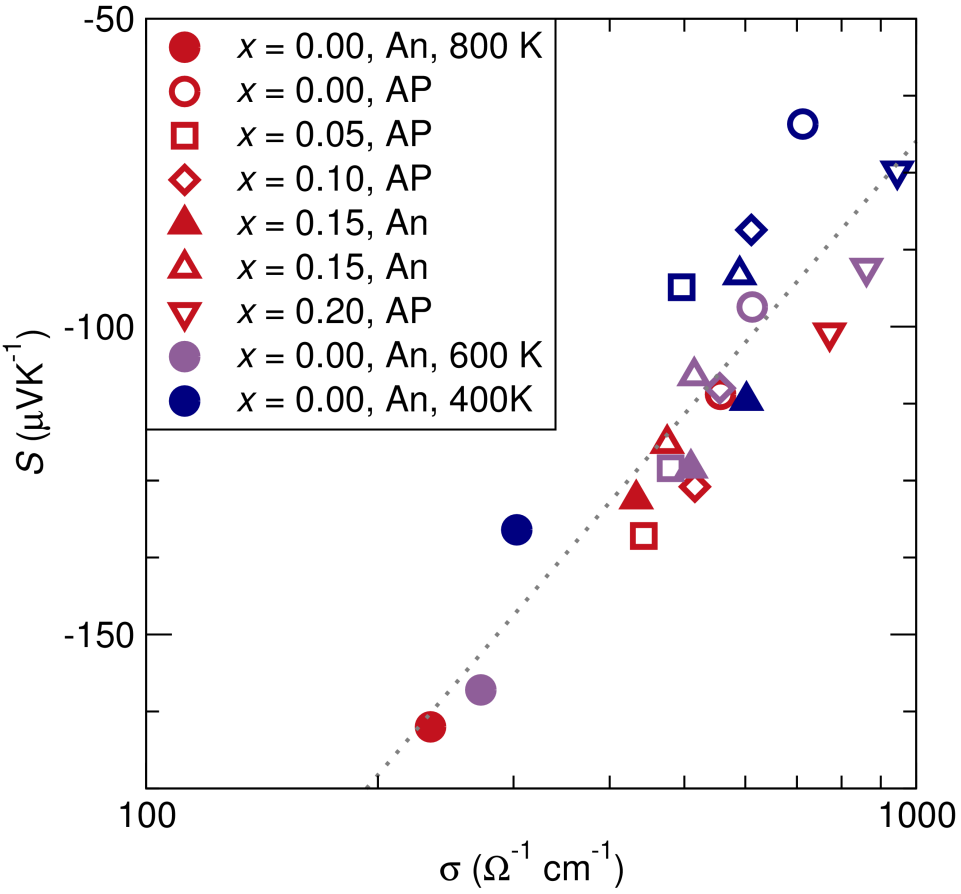

Figure B.1: NbCoSn and biphaic NbCoSn/$NbCo_2Sn$ physical property measurements plotted as a Price curve. A grey trend line indicates measurements follow Price curve behavior with a positive slope. These results indicate that charge carrier concentration is modified with temperature and that electrical conduction occurs at a consistent energy of the electronic band structure regardless of x or sample preparation.

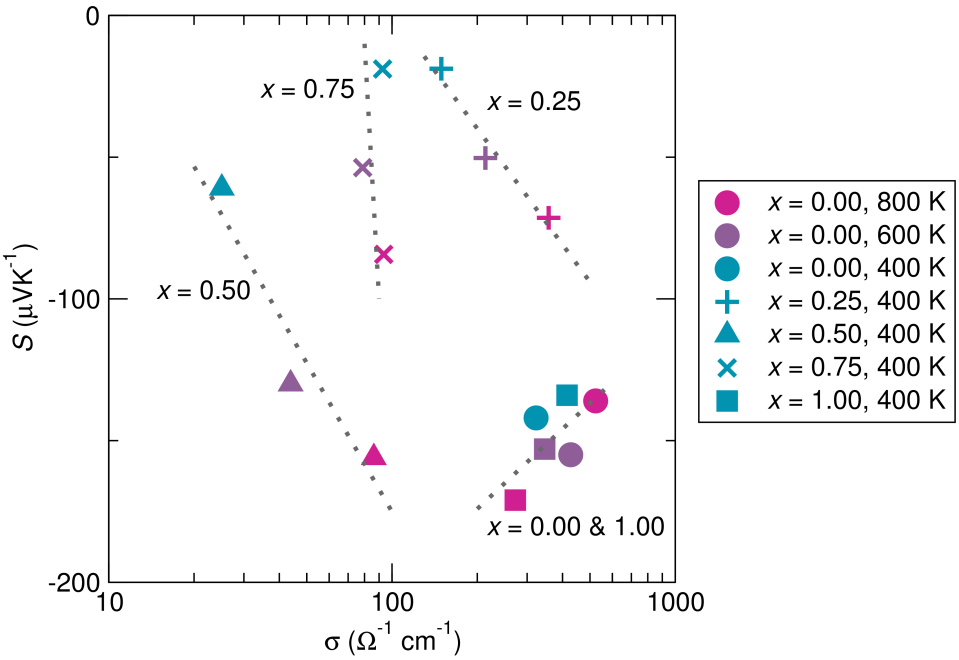

Figure B.2: $(TiNiSn)_{1-x}(NbCoSn)_x$ physical property measurements plotted as electrical resistivity and Seebeck coefficient with grey trend lines drawn for respective alloys. Pure half-Heusler compounds TiNiSn and NbCoSn ($x = 0.00$ and 1.00) follow general Price curve behavior with a positive slope. Intermediate alloys ($x = 0.25$, 0.50 and 0.75) do not obey Price curve behavior. These results indicate that intermediate alloys behave differently than the end member compounds, as could result from non-semiconductor temperature dependence of charge carrier concentrations, or from an electronic band structure that significantly differs from NbCoSn and TiNiSn.

Bibliography

[1] BCS Incorporated. Waste heat recovery: Technology and opportunities in U.S. industry. Technical report, U.S. Department of Energy - Industrial Technologies Program, 2008.

[2] G. J. Snyder and E. S. Toberer. Complex thermoelectric materials. *Nat. Mater.*, 7:105, 2008.

[3] Terry M. Tritt. Thermoelectric phenomena, materials, and applications. *Annu. Rev. Mater. Res*, 41:433, 2011.

[4] Ali Shakouri. Recent developments in semiconductor thermoelectric physics and materials. *Annu. Rev. Mater. Res*, 41:399, 2011.

[5] V. Leonov. Thermoelectric energy harvesting of human body heat for wearable sensors. *IEEE Sense. J.*, 13(6):2284, 2013.

[6] Jihui Yang and Thierry Caillat. Thermoelectric materials for space and automotive power generation. *IEEE Sense. J.*, 31(3):224, 2006.

[7] K. Smith and M. Thorton. Feasibility of thermoelectrics for waste heat recovery in conventional vehicles. Technical report, U.S. Department of Energy, 2009.

[8] Lon E. Bell. Cooling, heating, generating power, and recovering waste heat with thermoelectric systems. *Science*, 321(5895):1457, 2008.

[9] T. J. Seebeck. Ueber die magnetische polarisation der metalle und erze durch temperatur-differenz. *Ann. Phys.*, 82(2):133, 1826.

[10] J. Heremans, M. Dresselhaus, L. Bell, and D. Morelli. When thermoelectrics reached the nanoscale. *Nature Nanotech.*, 8(7):487, 2013.

[11] A. J. Minnich, M. S. Dresselhaus, Z. F. Ren, and G. Chen. Bulk nanostructured thermoelectric materials: current research and future prospects. *Energy Environ. Sci.*, 2(5):466, 2009.

[12] Eric S. Toberer, Lauryn L. Baranowski, and Chris Dames. Advances in thermal conductivity. *Annu. Rev. Mater. Res.*, 42:179, 2012.

[13] Michael W. Gaultois, Taylor D. Sparks, Christopher K. H. Borg, Ram Seshadri, William D. Bonificio, and David R. Clarke. Data-driven review of thermoelectric materials: Performance and resource considerations. *Chem. Mater.*, 25(15):2911, 2013.

[14] X. Yan, B. Poudel, Y. Ma, W. Liu, G. Joshi, H. Wang, Y. Lan, D. Wang, G. Chen, and Z. Ren. Experimental studies on anisotropic thermoelectric properties and structures of $n-$type $Bi_2Te_{2.7}Se_{0.3}$. *Nano. Lett.*, 10(9):3373, 2010.

[15] H. Kleinke. New bulk materials for thermoelectric power generation: Clathrates and complex antimonides. *Chem. Mater.*, 22(3):604, 2010.

[16] X. Shi, J. Yang, J. Salvador, M. Chi, J. Cho, H. Wang, S. Bai, J. Yang, W. Zhang, and L. Chen. Multiple-filled skutterudites: High thermoelectric figure of merit through separately optimizing electrical and thermal transports. *J. Am. Chem. Soc.*, 133(10):7837, 2011.

[17] Sung-Wng Kim, Yoshisato Kimura, and Yoshinao Mishima. High temperature thermoelectric properties of TiNiSn-based half-Heusler compounds. *Intermetallics*, 15(3):394, 2007.

[18] H. Hohl, A. P. Ramirez, W. Kaefer, K. Fess, Ch. Thurner, Ch. Kloc, and E. Bucher. A new class of materials with promising thermoelectric properties: MNiSn (M = Ti, Zr, Hf). *Mater. Res. Soc. Symp. Proc.*, 478:109, 1997.

[19] Cui Yu, Tie-Jun Zhu, Rui-Zhi Shi, Yun Zhang, Xin-Bing Zhao, and Jian He. High-performance half-Heusler thermoelectric materials Hf_{1-x}

$Zr_xNiSn_{1-y}Sb_y$ prepared by levitation melting and spark plasma sintering. *Acta Mater.*, 57(9):2757, 2009.

[20] F. Heusler. Manganese bronze and synthesis of magnetizable alloys from nonmagnetic metals. *Angew. Chem*, 17(9):260, 1904.

[21] S. Tsunegi, Y. Sakuraba, M. Oogane, K. Takanashi, and Y. Ando. Large tunnel magnetoresistance in magnetic tunnel junctions using a Co_2MnSi Co_2MnSi Heusler alloy electrode and a MgO barrier. *Appl. Phys. Lett.*, 93:112506, 2008.

[22] S. Chadov, X. Qi, J. Kubler, G. Fecher, C. Felser, and S. Zhang. Tunable multifunctional topological insulators in ternary Heusler compounds. *Nature Mater.*, 9:541, 2010.

[23] F. Tafti, T. Fujii, A. Juneau-Fecteau, S. Cotret, N. Doiron-Leyraud, A. Asamitsu, and L. Taillefer. Superconductivity in the noncentrosymmetric half-Heusler compound LuPtBi: a candidate for topological superconductivity. *Phys. Rev. B*, 87:184504, 2013.

[24] A. Planes, L. Manosa, and M. Acet. Magnetocaloric effect and its relation to shape-memory properties in ferromagnetic Heusler alloys. *J. Phys.: Condens. Matter*, 21(23):233201, 2009.

[25] S. Chen and Z. Ren. Recent progress of half-Heusler for moderate temperature thermoelectric applications. *Mater. Today*, 16(10):287, 2013.

[26] S. Ogut and K. M. Rabe. Band gap and stability in the ternary intermetallic compounds NiSnM (M = Ti, Zr, Hf): A first-principles study. *Phys. Rev. B*, 51:10443, 1995.

[27] T. Graf, C. Felser, and S. Parkin. Simple rules for the understanding of Heusler compounds. *Prog. Solid State Chem.*, 39(1):1, 2011.

[28] H. Kandpal, C. Felser, and R. Seshadri. Covalent bonding and the nature of band gaps in some half-Heusler compounds. *J. Phys. D: Appl. Phys*, 39(5):776, 2006.

[29] I. Galanakis, P. H. Dederichs, and N. Papanikolaou. Slater-Pauling behavior and origin of the half-metallicity of the full-Heusler alloys. *Phys. Rev. B*, 66:174429, 2002.

[30] G. E. Bacon and J. S. Plant. Chemical ordering in Heusler alloys with the general formula A_2BC or ABC. *Contemp. Phys.*, 1:524, 1971.

[31] Peter J. Webster. Heusler alloys. *Contemp. Phys.*, 10:559, 1969.

[32] S. Sakurada and N. Shutoh. Effect of Ti substitution on the thermoelectric properties of (Zr,Hf)NiSn half-Heusler compounds. *Appl. PHys. Lett.*, 86:082105, 2005.

[33] S. Bhattacharya, A. Pope, R. Littleton, T. Tritt, V. Ponnambalam, Y. Xia, and S. Poon. Effect of Sb doping on the thermoelectric properties of Ti-based half-Heusler compounds, $TiNiSn_{1-x}Sb_x$. *Appl. Phys. Lett.*, 77:2476, 2000.

[34] S. Picozzi, A. Continenza, and A. J. Freeman. Role of structural defects on the half-metallic character of Co_2MnGe and Co_2MnSi Heusler alloys. *Phys. Rev. B*, 69:094423, 2004.

[35] Ruth A. Downie, Ronald I. Smith, Donald A. MacLaren, and Jan-Willem G. Bos. Metal distributions, efficient n-type doping, and evidence for in-gap states in $TiNi{M}_ySn$ (M = Co, Ni, Cu) half-Heusler nanocomposites. *Chem. Mater.*, 27:2449, 2015.

[36] J. E. Douglas, P. A. Chater, C. M. Brown, T. M. Pollock, and R. Seshadri. Nanoscale structural heterogeneity in Ni-rich half-Heusler TiNiSn. *J. Appl. Phys.*, 116:163514, 2014.

[37] Hirofumi Hazama, Masato Matsubara, Ryoji Asahi, and Tsunehiro Takeuchi. Improvement of thermoelectric properties for half-Heusler TiNiSn by interstitial Ni defects. *J. Appl. Phys.*, 110:063710, 2011.

[38] J. E. Douglas, C. S. Birkel, N. Verma, V. M. Miller, M.-S. Miao, G. D. Stucky, T. M. Pollock, and R. Seshadri. Phase stability and property evolution of biphasic TiNiSn alloys for use in thermoelectric applications. *J. Appl. Phys.*, 115:043720, 2014.

[39] J. E. Douglas, M. P. Echlin, W. C. Lenthe, R. Seshadri, and T. M. Pollock. Three-dimensional multimodal imaging and analysis of biphasic microstructure in a TiNiSn thermoelectric material. *APL Mater.*, 3:096107, 2015.

[40] J. Makongo, D. Misra, J. Salvador, N. Takas, G. Wang, M. Shabetai, A. Pant, P. Paudel, C. Uher, K. Stokes, and P. Poudeu. Thermal and electronic charge transport in bulk nanostructured $Zr_{0.25}Hf_{0.75}NiSn$ composites with full-Heusler inclusions. *J. Solid State Chem.*, 184(11):2948, 2011.

[41] Y. Kimura and Y. Chai. Ordered structures and thermoelectric properties of MNiSn (M = Ti, Zr, Hf)-based half-Heusler compounds affected by close relationship with Heusler compounds. *JOM*, 67(1):233, 2014.

[42] K. Biswas, J. He, I. Blum, C. Wu, T. Hogan, D. Seidman, V. Dravid, and M. Kanatzidis. High-performance bulk thermoelectrics with all-scale hierarchical architectures. *Nature*, 489:414, 2012.

[43] Y. Ono, S. Inayama, H. Adachi, and T. Kajitani. Thermoelectric properties of doped half-Heuslers $NbCoSn_{1-x}Sb_x$ and $Nb_{0.99}Ti_{0.01}CoSn_{1-x}Sb_x$. *Jpn. J. Appl. Phys.*, 45(11):8760, 2006.

[44] Y. Kimura and Y. Tamura. Thermoelectric properties of directionally solidified half-Heusler compound NbCoSn alloys. *Appl. Phys. Lett.*, 92:012105, 2008.

[45] Y. Kimura, Y. Tamura, and T. Kita. Thermoelectric properties of nearly single-phase half-Heusler NbCoSn alloys and importance of microstructures for improving performance. *Mater. Res. Soc. Symp. Proc.*, 1044:U07–06, 2007.

[46] A. C. Larson and R. B. Von Dreele. General structure analysis system (GSAS). *Los Alamos National Laboratory Report*, page 86, 2000.

[47] B. H. Toby. EXPGUI, a graphical user interface for GSAS. *J. Appl. Cryst*, 34:210, 2001.

[48] K. Momma and F. Izumi. VESTA 3 for three-dimensional visualization of crystal, volumetric and morphology data. *J. Appl. Cryst*, 44:1272, 2011.

[49] G. Kresse and J. Furthmuller. Efficiency of ab-initio total energy calculations for metals and semiconductors using a plane-wave basis set. *Comput. Mater. Sci.*, 6(1):15, 1996.

[50] G. Kresse, M. Marsman, J. Fürthmuller, and J. Vienna. Ab-initio simulation package: VASP the guide. 2012.

[51] P. E. Blochl. Projector augmented-wave method. *Phys. Rev. B*, 50:17953, 1994.

[52] G. Kresse and D. Joubert. From ultrasoft pseudopotentials to the projector augmented-wave method. *Phys. Rev. B*, 59:1758, 1999.

[53] J. Perdew, K. Burke, and M. Ernzerhof. Generalized gradient approximation made simple. *Phys. Rev. Lett.*, 77:3865, 1996.

[54] S. Curtarolo, W. Setyawan, G. Hart, M. Jahnatek, R. Chepulskii, R. Taylor, S. Wang, J. Xue, K. Yang, O. Levy, M. Mehl, H. Stokes, D. Demchenko, and D. Morgan. AFLOW: an automatic framework for high-throughput materials discovery. *Comput. Mater. Sci.*, 58:218, 2012.

[55] J. Heyd and M. Ernzerhof. Hybrid functionals based on a screened Coulomb potential. *J. Chem. Phys.*, 118:8207, 2003.

[56] R. Hill. The elastic behaviour of a crystalline aggregate. *Proc. Phys. Soc. A*, 65(5):349, 1952.

[57] X. Huang, X. Wang, and B. Cook. Coherent nanointerfaces in thermoelectric materials. *J. Phys. Chem. C*, 114(49):21003, 2010.

[58] A. May, E. Toberer, A. Saramet, and G. Snyder. Characterization and analysis of thermoelectric transport in $n-$type $Ba_8Ga_{16-x}Ge_{30+x}$. *Phys. Rev. B*, 80:125205, 2009.

[59] S. Yabuuchi, M. Okamoto, A. Nishide, Y. Kurosaki, and J. Hayakawa. Large Seebeck coefficients of Fe_2TiSn and Fe_2TiSi: First-principles study. *Appl. Phys. Express*, 6(2):025504, 2013.

[60] Y. Nishino, M. Kato, S. Asano, K. Soda, M. Hayasaki, and U. Mizutani. Semiconductorlike behavior of electrical resistivity in Heusler-type Fe_2VAl compound. *Phys. Rev. Lett.*, 79:1909, 1997.

[61] R. Weht and W. E. Pickett. Excitonic correlations in the intermetallic Fe_2VAl. *Phys. Rev. B*, 58:6855, 1998.

[62] D. J. Singh and I. I. Mazin. Electronic structure, local moments, and transport in Fe_2VAl. *Phys. Rev. B*, 57:14352, 1998.

[63] Y. Nishino, S. Deguchi, and U. Mizutani. Thermal and transport properties of the Heusler-type $Fe_2VAl_{1-x}Ge_x (0 < x < 0.20)$ alloys: Effect of doping on lattice thermal conductivity, electrical resistivity, and Seebeck coefficient. *Phys. Rev. B*, 74:115115, 2006.

[64] C. S. Lue, C. F. Chen, J. Y. Lin, Y. T. Yu, and Y. K. Kuo. Thermoelectric properties of quaternary Heusler alloys $Fe_2VAl_{1-x}Si_x$. *Phys. Rev. B*, 75:064204, 2007.

[65] T. Kanomata, T. Sasaki, T. Hoshi, T. Narita, T. Harada, H. Nishihara, T. Yoshida, R. Note, K. Koyama, H. Nojiri, T. Kaneko, and M. Motokawa. Magnetic and electrical properties of $Fe_{2+x}V_{1-x}Al$. *J. Alloys Compd.*, 317-318:390, 2001.

[66] H. Miyazaki, S. Tanaka, N. Ide, K. Soda, and Y. Nishino. Thermoelectric properties of Heusler-type off-stoichiometric $Fe_2V_{1+x}Al_{1-x}$ alloys. *Materials Research Express*, 1(1):015901, 2014.

[67] Mikami, Inukai, Miyazaki, and Nishino. Effect of off-stoichiometry on the thermoelectric properties of Heusler-type Fe_2VAl sintered alloys. *J. Elecron Mater.*, 45(3):1284, 2016.

[68] C. S. Lue and Y.-K. Kuo. Thermoelectric properties of the semimetallic Heusler compounds $Fe_{2-x}V_{1+x}M$ (M = Al, Ga). *Phys. Rev. B.*, 66:085121, 2002.

[69] Nakama, Takaesu, Yagasaki, Naka, Matsushita, Fukuda, and Yamada. Transport properties of Heusler compounds $Fe_{3-x}V_xAl$. *J. Phys. Soc. Jpn.*, 74:1378, 2005.

[70] C. S. Lue and Y.-K Kuo. Thermal and transport properties of the Heusler-type compounds $Fe_{2-x}Ti_{1+x}Sn$. *J. Appl. PHys.*, 96:2681, 2004.

[71] M. Nakabayashi, K. Fukuda, H. Kitagawa, Y. Yamada, S. Kubo, and A. Matsushita. Magnetic and transport properties in Heusler-type Fe_2TiSn compound. *Physica B*, 329-333(2):1134, 2003.

[72] A. Slebarski, M. B. Maple, C. Sirvent E. J. Freeman, D. Tworuszka, M. Orzechowska, A. Wrona, A. Jezierski, S. Chiuzbaian, and M. Neumann. Weak ferromagnetism induced by atomic disorder in Fe_2TiSn. *Phys. Rev. B*, 62:3296, 2000.

[73] J.E. Frackowiak and J. Deniszczyk. Mossbauer effect study of atomic disorder in Fe_2TiSn alloy. *Mol. Phys. Rep.*, 38:79, 2003.

[74] A. Slebarski. Electron-correlation effects in a disordered Fe_2TiSn Heusler alloy. *J. Phys. D: Appl. Phys.*, 39(10):856, 2006.

[75] A. Coelho. Topas academic V5 software. http://www.topas-academic.net/, 2012.

[76] J. Jong, J. Zhu, M.-G. Jon, Y. Zhou, J. Kim, and J. Yan. Theoretical investigation of stabilities and physical properties of low cost Fe-based full-Heusler materials. *J. Alloys Compd.*, 693:462, 2017.

[77] H. Luo, G. Liu, F Meng, J. Li, E. Liu, and G Wu. Half-metallicity in Fe-based Heusler alloys Fe_2TiZ (Z = Ga, Ge, As, In, Sn and Sb). *J. Magn. Magn. Mater.*, 324(20):3295, 2012.

[78] B. Xu and L. Yi. Optical properties of the intermetallic compound Fe_2TiSn. *J. Phys. D: Appl. Phys.*, 41:095404, 2008.

[79] A. Denton and N. Ashcroft. Vegard's law. *Phys. Rev. A*, 43(6):3161, 1991.

[80] L. Jodin, J. Tobola, P. Pecheur, H. Scherrer, and S. Kaprzyk. Effect of substitutions and defects in half-Heusler FeVSb studied by electron transport measurements and KKR-CPA electronic structure calculations. *Phys. Rev. B*, 70:184207, 2004.

[81] P.J. Cote. Electrical resistivity of amorphous nickel phosphorus alloys. *Solid State Commun.*, 18(9-10):1311, 1976.

[82] M. Kass, C. Brooks, D. Falcon, and D. Basak. Electrical resistivity of amorphous nickel phosphorus alloys. *Intermetallics*, 10(10):951, 2002.

[83] R. A. Downie, S. A. Barczar, R. I. Smith, and J. W. G. Bos. Compositions and thermoelectric properties of XNiSn (X = Ti, Zr, Hf) half-Heusler alloys. *J. Mater. Chem. C*, 3:10534, 2015.

[84] J. E. Douglas, C. S. Birkel, N. Verma, V. M. Miller, M.-S. Miao, G. D. Stucky, T. M. Pollock, and R. Seshadri. Phase stability and property evolution of biphasic TiNiSn alloys for use in thermoelectric applications. *J. Appl. Phys.*, 115:043720, 2014.

[85] M. L. C. Buffon, G. Laurita, N. Verma, L. Lamontagne, L. Ghadbeigi, D. L. Lloyd, T. D. Sparks, T. M. Pollock, and R. Seshadri. Enhancement of thermoelectric properties in the NbCoSn half-Heusler/Heusler system through spontaneous inclusion of a coherent second phase. *J. Appl. Phys*, 120:075104, 2016.

[86] Hiroaki Muta, Takanori Kanemitsu, Ken Kurosaki, and Shinsuke Yamanaka. High-temperature thermoelectric properties of Nb-doped MNiSn (M = Ti, Zr) half-Heusler compound. *J. Alloys Compd.*, 469:50, 2009.

[87] V. A. Romaka, Yu. V. Stadnyk, D. Fruchart, T. I. Dominuk, L. P. Romaka, P. Rogl, and A. M. Goryn. The mechanism of generation of the donor- and acceptor-type defects in the n-TiNiSn semiconductor heavily doped with Co impurity. *Semiconductors*, 43:1124, 2009.

[88] Mohamad N. Rahaman. *Ceramic Processing*. CRC Press, 2006.

[89] A. Munter. Neutron scattering lengths and cross sections. https://www.ncnr.nist.gov/resources/n-lengths/, 2011.

[90] Catherine Colinet, Philippe Jund, and Jean-Claude Tedenac. NiTiSn a material of technological interest: Ab initio calculations of phase stability and defects. *Intermetallics*, 46:103, 2014.

[91] Nisha Verma, Jason E. Douglas, Stephan Kramer, Tresa M. Pollock, Ram Seshadri, and Carlos G. Levi. Microstructure evolution of biphasic $TiNi_{1+x}Sn$ thermoelectric materials. *Mat. Trans. A*, 47:4116, 2016.

[92] Chenguang Fu, Hanhui Xie, Yintu Liu, T.J. Zhu, Jian Xie, and X.B. Zhao. Thermoelectric properties of FeVSb half-Heusler compounds by levitation melting and spark plasma sintering. *Intermetallics*, 32:39, 2013.

[93] Yoshisato Kimura, Akihisa Zama, and yoshinao Mishima. Thermoelectric properties of p-type half-Heusler compounds HfPtSn and ZrPtSn. *2006 25th Inter. Confer. on Thermoelect.*, 25:115, 2006.

[94] P. J. Price. Theory of transport effects in semiconductors: Thermoelectricity. *Phys. Rev.*, 104:1223, 1956.